# Aerodynamic performance improvement of vertical axis wind turbines through novel techniques


**Yan Yan**

School of Engineering and Material Science
Queen Mary University of London

This dissertation is submitted for the degree of
*Doctor of Philosophy*

April 2020

# Declaration

The work described in this thesis was carried out in the School of Engineering and Material Science, Queen Mary University of London, between October 2015 - September 2019. I declare that except where specific reference is made to the work of others, the contents of this dissertation are original and have not been submitted in whole or in part for consideration for any other degree or qualification in this, or any other university. This dissertation is my own work and contains nothing which is the outcome of work done in collaboration with others, except as specified in the text and Acknowledgements. I accept that the College has the right to use plagiarism detection software to check the electronic version of the thesis.

The work in this thesis has so far produced the following three journal and one conference publications:

Yan, Y., Avital, E., Williams, J., and Cui, J. (2019). CFD analysis for the performance of micro-vortex generator on aerofoil and vertical axis turbine. AIP Journal of Renewable and Sustainable Energy, 11(4):043302. (Editor's pick)

Yan Yan, Eldad Avital, John Williams and Theodosios Korakianitis. CFD Analysis for the Performance of Gurney Flap on Aerofoil and Vertical Axis Turbine. International Journal of Mechanical Engineering and Robotics Research, Vol.8, No.3, pp.385-392,2019.

Yan Yan, Eldad Avital, John Williams, and Jiahuan Cui. Performance Improvement of Vertical Axis Wind Turbine Through Gurney Flap. ASME. J. Fluids Engineering. Accepted.

Yan Yan, and Eldad Avital. Aerodynamic and Aeroacoustic Redesign of Low Speed Blade Profile. 2016 International Congress on Sound and Vibration.23-27 July, London.

Yan Yan
April 2020

# Acknowledgements

First and foremost, I wish to express my gratitude to my doctoral research advisor, Dr. Eldad Avital, for his support, encouragement, and guidance during my research. His enthusiasm and commitment to high quality research has inspired me greatly.

Special thanks are due to the development team of Code_Saturne, particularly Mr. Yvan Fournier for his help solving the problems about the understanding and usage of Code_Saturne.

Also, I thank my colleagues Dr. Andrew Hefferon and Dr. Kaiming Ai for their continuing guidance, valuable discussion and advices. I also thank my colleague Mr. Mingyang Wang for his kind help on my research. I thank to Mr. Jonathan Hills and other staff at QMUL for their help throughout my studies.

Finally, I want to thank the endless support and encouragement for my parents during my doctoral studies.

This work is funded by China Scholarship Council (CSC)/ Queen Mary Joint PhD scholarship.

# Abstract

In order to improve the aerodynamic performance of the vertical axis wind turbines (VAWTs), the presented research seeks to use the novel idea of three different flow control techniques, Gurney flaps (GF), passive micro vortex generators (MVGs) and leading-edge protuberances to extend the operating range and to suppress aerodynamic instabilities for a small-scale H-type VAWT.

Two dimensional simulations are used to assess the impact of various GFs on the isolated aerofoil. It is found that the GFs can enhance the aerodynamic performance of the aerofoil by generating more lift and delaying the onset of stall. The benefit of having GF of 1%c and 2%c height is also shown for H-VAWT achieving significant power improvement at low tip speed ratios (TSRs).

The main function of the MVGs is to transfer momentum from outside into the inner boundary layer, leading to the suppression of flow separation. In this study, a set of properly designed MVGs is found to increase the lift and reduce the drag of the isolated aerofoil beyond the stall angle. The VAWT with MVGs control shows significant enhancement in power generation at high TSR ranging from 2 to 3.5. The optimum configuration of the MVGs is found to be located at 20% chord length of the blade, having a rectangular shape and a mounting angle of 16°.

Sinusoidal wave protuberances of the leading edge are numerically investigated to obtain the detailed flow fields for analysis and visualization. The results show that leading-edge protuberances with proper design can improve the lift of the blade near the stall angle and the power generation of the VAWT at TSR ranging from 1 to 2.5.

The three passive flow controls have been numerically investigated to show their ability to improve the aerodynamic performance of VAWTs and their strong potential for this sector.

# Table of contents

# List of figures

# List of tables

# Nomenclature

**Acronyms**

AFW Active flexible wall

AoA Angle of attack

BC Before Christ

CFD computational fluid dynamics

DNS Direct numerical simulation

EDF Eletricite de France

GF Gurney flap

GW Gigawatt

GWEC Global wind energy council

HAWT Horizontal axis wind turbine

ILES Implicit large eddy simulation

kW Kilowatt

LES Large eddy simulation

LSB Laminar separation bubble

MVG Micro vortex generator

NASA National Aeronautics and Space Administration

PIV Particle image velocimetry

RANS Reynolds-averaged Navier–Stokes equations

SGS Subgrid-Scale model

SVG Smart vortex generators

TSR Tip speed ratio

UK United Kingdom

URANS Unsteady Reynolds-averaged Navier–Stokes equations

US United States

VAWT Vertival axis wind turbine

VG Vortex generator

ZVWT Zephyr veritcal axis wind turbine

**Greek Symbols**

$\alpha$ Angle of attack

$\beta$ Mounting angle of micro vortex generator

$\delta$ Thickness of boundary layer

$\Delta$t Time step

$\delta^\star$ Displacement thickness

$\Delta_g$ Filter width

$\delta_{ij}$ Kronecker delta

$\varepsilon$ Internal energy

$\Gamma$ Wall shear stress

$\gamma$ Mounting angle of Gurney flap

$\lambda$ Tip speed ratio

$\mu$ Dynamic viscosity

$\mu_t$ Eddy viscosity

$\omega$ Rotor rotation speed (Chapter 4)

$\omega$ The specific dissipation rate (Chapter 3)

$\phi'$ Unresolved field

$\rho$ Density

$\sigma$ Solidity of turbine

$\tau_{ij}$ Reynolds stress tensor

$\theta$ Azimuth angle

$\theta^\star$ Momentum thickness

$\tilde{\Delta}$ Length scale

$\tilde{\phi}$ Filtered field

$\varphi$ Amplitude of leading-edge protuberance

**Roman Symbols**

$a, b$ Spacing between vortex generators (Chapter 5)

$a$ Induction factor (Chapter 4)

$c$ aerofoil chord length

$C_D$ Drag coefficient

$C_f$ Skin friction coefficient

$C_L$ Lift coefficient

$C_m$ Torque coefficient

$C_P$ Power coefficient

$C_p$ Pressure coefficient

$C_s$ Constant

| | |
|---|---|
| $D$ | Drag |
| $d$ | Diameter of turbine rotor |
| $e$ | Length of micro vortex generatort |
| $F$ | Function |
| $F_x$ | Force on X direction |
| $F_y$ | Force on Y direction |
| $G$ | Filter convolution kernel |
| $g$ | Gravity acceleration |
| $H$ | Height of turbine blade |
| $h$ | Height of micro vortex generator |
| $H_s$ | Shape factor |
| $k$ | Turbulent kinetic energy |
| $L$ | Lift |
| $Ma$ | Mach number |
| $N$ | Number of rotor blades |
| $o$ | Wavelength of leading-edge protuberance |
| $p$ | Pressure |
| $P_\infty$ | Static pressure |
| $P_m$ | Mechanical energy produced by turbine |
| $R$ | Radius of turbine (Chapter 5) |
| $r$ | Radius of rotor (Chapter 2) |
| $Re$ | Reynolds number |
| $Re_c$ | Reynolds number based on chord length |

| | |
|---|---|
| $Re_{ij}$ | Reynolds stress |
| $S$ | Cross section area of turbine |
| $s$ | distance to the trailing edge of vortex generator |
| $S_{ij}$ | Strain tensor |
| $T$ | Temprature |
| $t$ | Time |
| $\overline{u_i}$ | Mean components of flow velocity |
| $U_0$ | Flow velocity at a point in flow field (Chapter 6) |
| $u_i$ | Flow velocity |
| $u_i'$ | Fluctuating components of flow velocity |
| $u_r$ | Relative velocity |
| $V$ | Wind velocity |
| $V_\infty$ | Freestream velocity |
| $y^+$ | Non-dimensional wall distance |
| (x,y,z) | Cartesian coordinates |

# Chapter 1

# Introduction

## 1.1 Vertical Axis Wind Turbine

### 1.1.1 A Brief Introduction to Wind Power Technology

With the rapid development of industry and economy, the demand of alternative clean energy sources, such as solar, biomass and wind is considerably growing in recent years. Until now fossil fuels, such as coal and oil, supported the world's energy demands. On the other hand, the excessive consumption of fossil fuels makes humanity face up the pressure of energy shortage because of the increasing exploitation of finite fossil fuel resources for next decades as well as the problem of environment pollution. It has been reported that the emission of green house gases will increase by over 100 % in mid-21st century from 2005 [53]. The energy crisis has become a great challenge. As a result, demands have increased for an energy technology revolution of alternative environmental-friendly energy sources and greater energy efficiency.

Wind power is one of the most popular clean and renewable resource, which possesses significant potential, because of its wide distribution on the earth. Wind energy has some advantages that the conventional energy does not have: 1) It is renewable non-polluting resource that has nearly no impact on the environment. 2)It is free and very abundant in many parts of the earth. 3) Part of wind power technology is mature and the evolution of wind power industry is encouraged by government in many countries.

Figure 1.1 portrays the $CO_2$ emission reduction in various power sectors, which indicates that wind energy is one of the most environmentally promising renewable energy options. Furthermore, huge quantities of renewable energy can be extracted from oceans, in which there are a lot of marine and tidal energy. These energies can be extracted by marine current

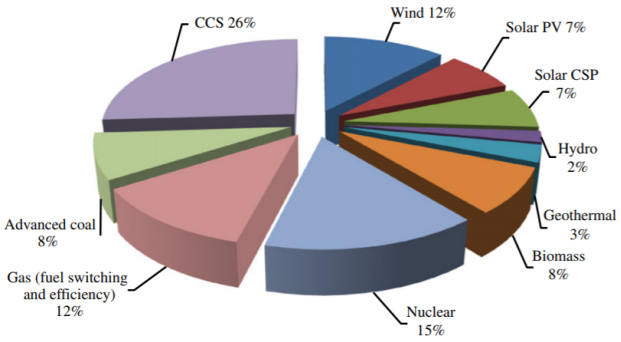


Fig. 1.1 $CO_2$ emissions reduction in various power sectors [53].

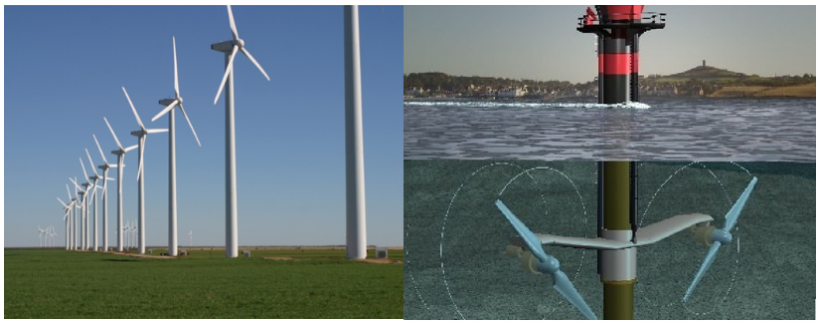

Fig. 1.2 Horizontal axis wind turbine (right) and marine turbine (left) [7]

turbine (as Figure 1.2 (left) of different scales, which can transform the kinetic energy stored in the ocean into electrical power. One should note that the fundamentals of the hydro marine turbine is similar to the wind turbine, although there are differences in the fluid density, steadiness in the flow as well as structural and materials demands.

The usage of wind power for humans has a long history, which could be traced back to 3000 years ago. The oldest wind power devices was found in ancient Persia as early as 300 BC [115]. In old times the fluctuating wind energy resource was used for mechanical applications, which was applied for irrigation.

Due to the development of modern technology, wind power was directed for electrical energy generation instead of first mechanical energy in 1970s. Because of the oil crisis and oil price shock during that period, wind energy technology went through rapid development and attracted more attention from government and research field than before [1]. As a result, much of the supporting mechanism and techniques have developed since 1970s. The capacity of the wind turbine grew step by step. In early 1980s, the typical size of wind turbines was less than 100 kW and more than 90 % of world installed capacity are in the United States. By 1990s, the normal size of wind turbines increased to over 450 kW. By the end of 1990s, it continued to increase to nearly 750 kW. In recent years, the capacity of large wind turbines

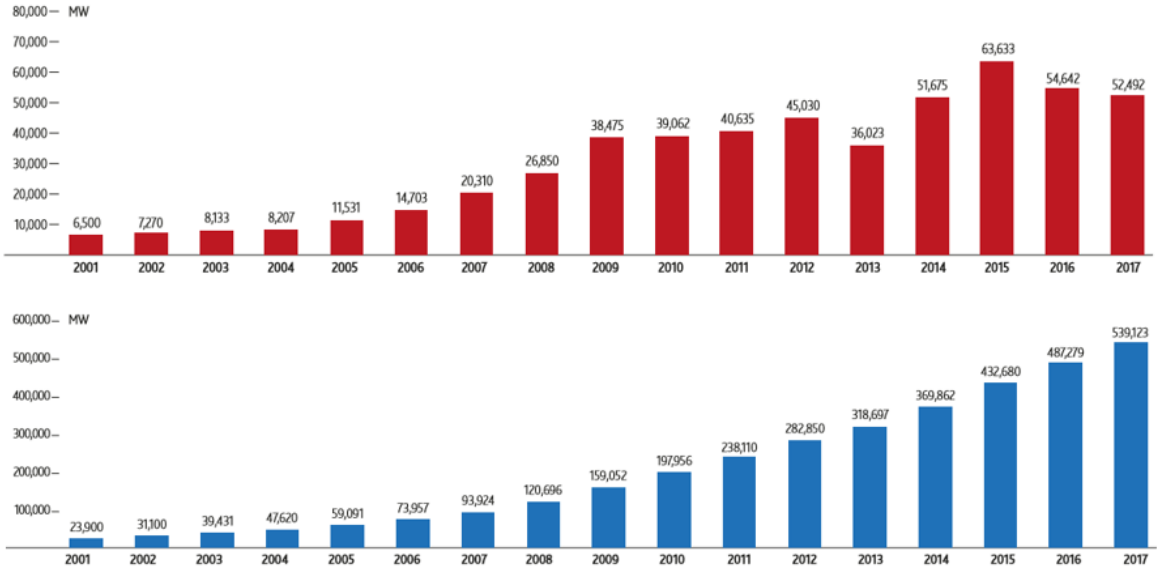


Fig. 1.3 Global annual and cumulative installed wind capacity from 2001 to 2017, reproduced from GWEC's global wind report [39].

rapidly grew to 3500 kW [115]. Many countries have adopted the energy policy including reducing usage of fossil fuels and encouraging renewable environmental-friendly resources. Wind energies become one of the fastest developing sustainable energy all around the world. It is reported that the global wind industry is present in more than 80 countries and among them there are 28 countries that have more than 1 GW capacity installed in total [1].

The latest global wind report from Global Wind Energy Council (GWEC) released in 2017 states that by the end of 2015 the global wind power capacity has reached about 433 GW and achieved improvement of 17% as compared to the previous year [39]. GWEC predicts that wind energy will share more than 12% of electricity demand around the global by 2020. Figure 1.3 shows global annual installed wind capacity and cumulative installed wind capacity from 2001 to 2017. The cumulative installed wind capacity increased by more than 25 times in this period.

The United States was one of the first countries to promote wind power in order to achieve energy independence until late 20th century. Then China experienced a rapid growth in wind power generation and became the largest wind power market around the world representing about one-third of global market followed by Europe and north America since 2007 [99]. United kingdom occupied the largest installed offshore wind capacity worldwide at 2012.

### 1.1.2 Wind Turbine Configurations

#### Wind Turbines of Various Scales

Wind turbines could be classified according to three parameters. In terms of size and power ratings, wind turbines fall into some basic groups: micro, small, medium or large. The boundaries between turbines of different capacity is vague and there is no absolute definition to distinguish the "small" and "large" wind turbines. The definition is related to the diameter of turbine rotor, Reynolds number and power output.

Usually the rotor diameter of small-scale turbines are mainly used for charging for small equipment, which have a diameter smaller than 15m and rated power less than 50 kW. Medium-scale ones are used to offer electricity supply for small area and their capacity ranges from 50 kW to 1.5 MW. The most of wind turbines fall into medium-scale size worldwide. Wind turbines, whose capacity are larger than 1.5MW are classified as large-scale turbines.

#### Horizontal Axis Wind turbine

Most commonly modern wind turbines are divided into two typical categories according to rotor axis relative to the wind stream direction: horizontal axis wind turbine (HAWT) and vertical axis wind turbine (VAWT). As the name suggests, for HAWTs, the rotor axis is parallel to direction of wind stream. The rotation axis of VAWTs is perpendicular to the ground and wind direction.

Currently HAWTs dominate the global wind energy market and more than 80% of wind turbines in operation worldwide are HAWTs due to their relatively high efficiency as compared to other wind turbine designs. The maximum power coefficient($C_p$) of a mid-scale HAWT could reach 0.5, but the VAWTs can hardly have a $C_P$ larger than 0.4 [64]. HAWTs can be further categorized in terms of the location of rotor: upwind or downwind of the tower. Although an active yaw control system is required for upwind configurations, currently the trend for the design of HAWTs is toward it. Upwind HAWTs have relatively high $C_P$ as compared to downwind ones. Because in downwind configurations wind needs to go pass the tower before reaching the rotor, which degrades the performance of the wind turbine and produces more noise [41].

HAWTs have different number of blades. For medium and large scale HAWTs, in order to have a lower starting torque, a low solidity configuration with three or two blades is preferred choice. Compared to the two-blade configuration, the rotor with three blades has better aerodynamic balance and produces low vibration, leading to a lower noise level and easy maintainess. In addition, for the two-blade rotor the turbine hub is connected to the main

shaft using teeter hinges instead of rigid connections that usually installed in three-blade turbines. For large-scale HAWTs, the installation of complex teeter hinge device is expensive. As a result, currently only 10% of wind turbines installed have two blades.

### Vertical Axis Wind turbine

Although HAWTs are much more popular as compared to VAWTs, the latter ones offer some advantages in some respects that HAWTs don't have.

1) VAWTs can eliminate the power production's dependence on the incoming direction of the air or water so they can accept the wind from all directions.

2) VAWTs do not require active yaw devices due to their vertical configurations.

3) The overall structure of VAWTs is simple, so they are easy for operation and maintenance.

4) VAWTs produce less noise.

5) The location of the generator is on the ground, which makes it easy for maintenance.

There are two normal types of VAWTs, Darrieus turbine (Figure 1.4) and Savonius turbine (Figure 1.5) or S-rotor. The Darrieus type wind turbines are named after their inventor Georges Darrieus from France. He got the patent of Darrieus wind turbine in 1931 that attracted much attention from researchers after the oil crisis. The Darrieus rotor is also called egg beater because of its shape, which is used to reduce the bending moments of blades. Since Darrieus turbines are based on lift force, the rotation speed of rotor blades can be as large as wind speed. The Darrieus wind turbines can capture the kinetic energy of wind from all directions and the largest wind speed in which the Darrieus wind turbine work can reach 220km/h.

If the egg beater type blade is replaced by straight blade, a new configuration of Darrieus wind turbine called Giromill turbine is created. As for the configuration of Giromill turbine (Figure 1.6), it is also called straight-bladed type Darrieus turbine or H-rotor, which is the simplest design of VAWTs. The Giromill turbine was created by Georges Darrieus in 1927, which is widely used in urban area as a small capacity machine because of their simple configuration and design. This kind of turbines consists of a wind wheel, spindle, tower, controller and magnet generator. The blades are fixed on the vertical tower in centre by a horizontal bridge that make the turbine has an H-style structure. So the Giromill turbines are also called H-type turbines. The blades of Giromill turbines are much heavier than other types of turbines, although they have relatively simpler design. In order to have a lighter structure and reduce the producing cost, the towers of these turbines are usually made

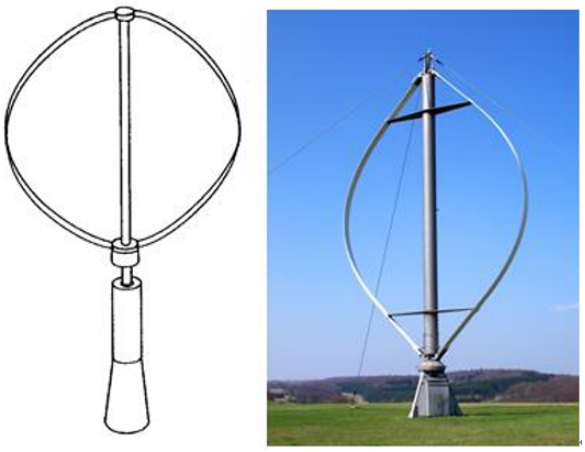

Fig. 1.4 Two-blade Darrieus wind turbine [43].

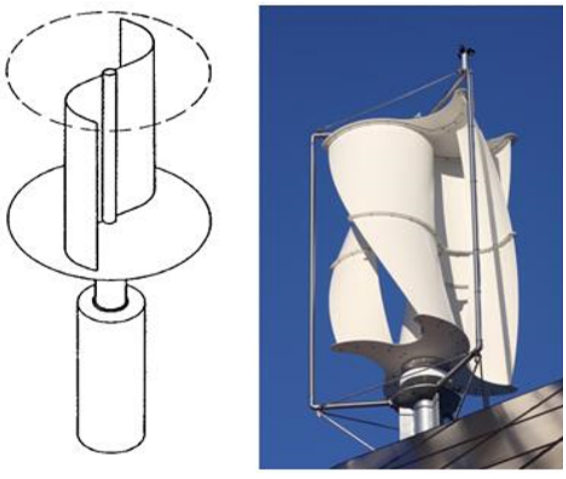

Fig. 1.5 Savonius wind turbine [86].

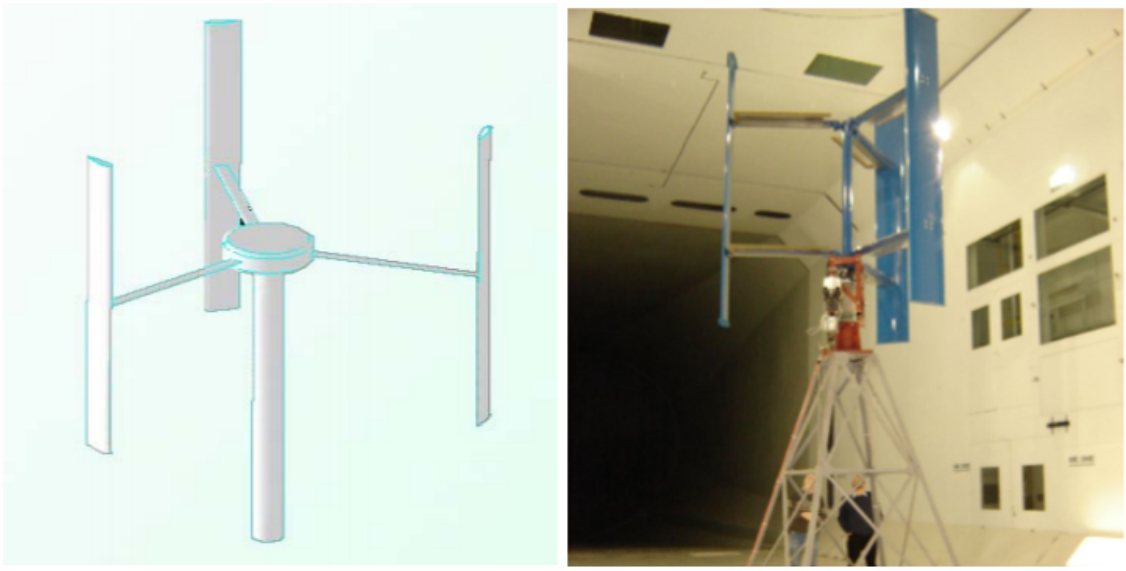

Fig. 1.6 Giromill turbine. [12] [40]

of wood. They are widely used in some complicated environment because of their good performance in turbulence wind and low noise generation.

As the counterpart of the straight-bladed H-type wind turbine, the twisted-bladed Darrieus turbine are more widely used worldwide. Gupta and Biswas [37] investigated the aerodynamic performance of a twisted three-blades Darrieus turbine via numerical simulation. They evaluated the influence of twisted angles on the efficiency of the wind turbines and determined the optimum value of it. The results showed that the twisted blades had positive lift at zero incidence angle, so that this type of turbines could be self-started at favorable wind conditions [37].

Unlike the Darrieus rotor based on lift force, Savonius rotor uses mainly drag force for power production. Therefore, its rotation speed can not reach the wind speed. As its low rotation speed and high torque, the Savonius rotor is ideal for driving pumps. A Savonius rotor consists of two half cylinders fixed on the rotating shaft. The drag on the two sides are different and the difference of drag offers a torque for propelling the turbine rotate.

Savonius turbine was created by Sigurd Savonius. This type of turbines has simple but large structure as compared to other types of turbines. They usually require high strength material for the blades. In addition, unlike the lift-type turbines, Savonius turbines have relatively low efficiency, so that their application on high power systems is limited [21]. Design is simplified because it is self-starting and the pointing mechanism is not required to

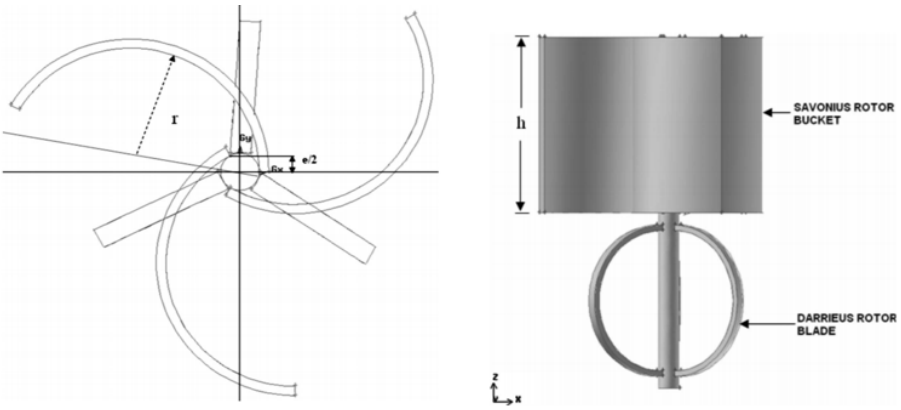


Fig. 1.7 Top view and front view of physical model of combined type wind turbine [21].

allow for shifting wind direction. The Savonius turbines are widely used in some areas, such as deep sea.

In order to overcome the demerits of normal Darrieus wind turbine, researchers combined it with Savonius configuration, which can produce a larger starting torque as shown Figure 1.7. The objective is to find a balance between the advantages and disadvantages of these two types of configuration. It was found that this new style of turbine has relatively high power coefficient and can be applied in the area of low wind velocity.

Debnath et al.[21] introduced a new style of wind turbine, which is the combination of two rotors: a three-bladed Darrieus turbine and a three-bucket Savonius turbine. The aerodynamic performance and the efficiency of both modified turbine were investigated by numerical methods. The results from the numerical simulation were verified by the wind tunnel test. It was found that the power coefficient ($C_P$) of the new wind turbine could reach as high as 0.35 and the torque generated was much higher than normal Darrieus wind turbines.

Gerald Muller [85] studied a kind of drag-based small scale wind turbine called Sistan wind mill as Figure 1.8, which is usually integrated with buildings and provides energy for them. In old times, this type of wind turbines had a very low efficiency because of technical limitation. The authors introduce some optimization methods that could improve $C_P$ to around 0.48.

Pope and Rodrigues [88] proposed a type of Savonius turbine for urban application called the Zephyr vertical axis wind turbine (ZVWT), which is firstly introduced by a Toronto based company [57]. In this turbine, a Savonius-type configuration is surrounded by some stationary stator tabs as shown in Figure 1.9. The steady tabs can reduce the turbulence in flow and allow the turbine to operate in high turbulent conditions.

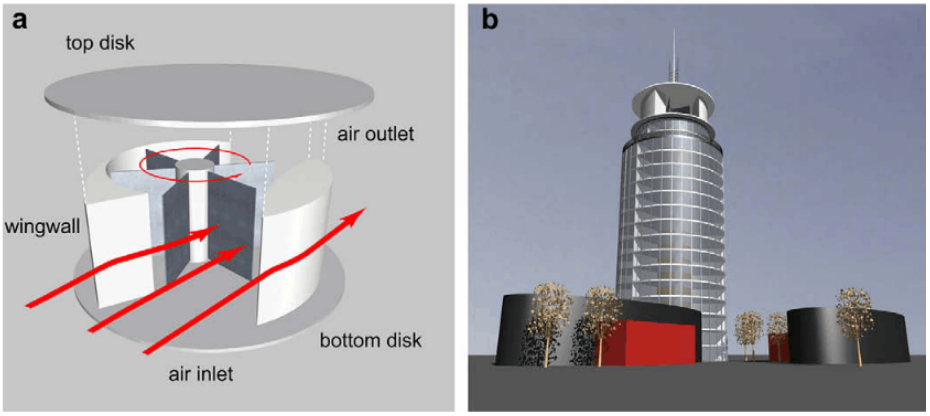


Fig. 1.8 Sistan wind mill[85]

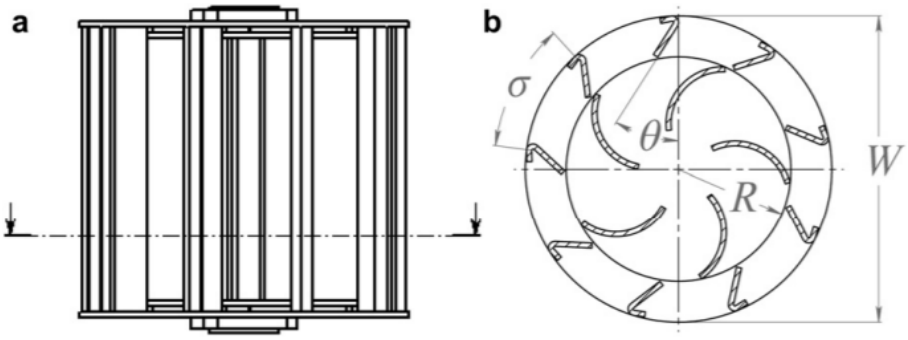


Fig. 1.9 Front view and top view of physical model of Zephyr turbine [88].

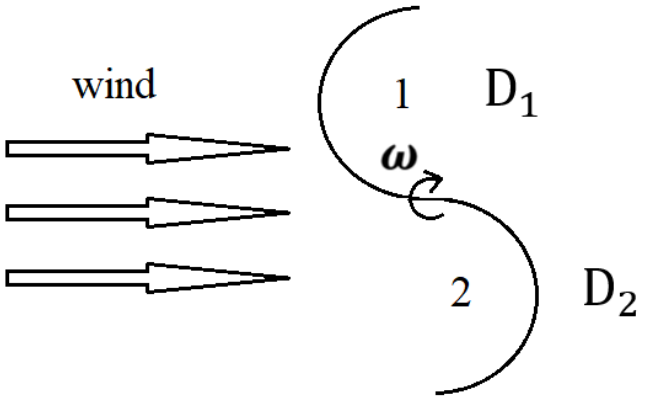


Fig. 1.10 Schematic view of drag-based Savonius wind turbine.

**Drag Type or Lift Type Wind Turbines**

The aerodynamic forces on the turbine blades could be distinguished as lift and drag. Wind turbines could be classified in terms of the way that wind energy extracted by wind turbines: lift-based wind turbines and drag-based wind turbines [57]. Modern wind industry is dominated by wind turbines based on lift [95]. All the HAWTs and a part of VAWTs belong to this category.

Savonius turbines are typical drag-type turbines [61]. Figure 1.10 portrays the simplified model of a Savonius turbine from the top view. As shown in the figure, the S-shape turbine consists of two scoops: 1 and 2. It's easy to know that scoop 1 moves against to the wind that experiences less drag as compared to scoop 2 that moves with the wind. The drag difference between the two scoops can propel the turbine to rotate. For the turbines driven by drag, the rotation speed is smaller than wind speed, which means that the Tip Speed Ratio (TSR) is smaller than 1. The TSR for a Savonius turbine is usually from 0.8 to 1. As a result, the energy captured by the drag-type wind turbines is much less than that from the lift-type wind turbines.

The lift-based wind turbines can extract power from wind by lift component of aerodynamic force on the turbine blades [64]. Darrieus turbines are the main typical lift-based turbines [62]. When the turbine blades rotate in the airflow, at some parts of one revolution, they experience positive incidence angles and the lift has a component force that has the same direction with their rotation velocity as shown in Figure 4.12 . This force can drive the blade to spin.

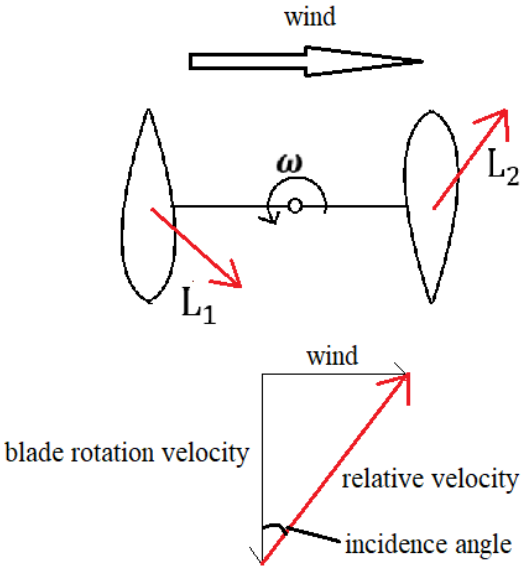


Fig. 1.11 Schematic view of lift-based two-blade H-type wind turbine.

### 1.1.3 Challenges of HAWT and Opportunity of Small VAWT Development

The large scale HAWT farms dominate the wind power industry worldwide, especially in the utility-scale segment [87]. Due to the complex designs and manufacturing costs, the development of VAWTs is limited, although the first VAWT has been invented about one hundred years ago [111]. Less financial support and less interest from researchers and commercial sectors restricted the development of VAWTs. In the United States, financial support for VAWTs was much less than that applied to the development of HAWTs, account for only 10% of the whole funding for wind energy systems in 1970s [59]. A similar condition could be found in UK. From 1970 to 1986, only 16% of the total financial expenditure on wind power research from UK department of energy was applied on the research and construction of VAWTs[90]. Despite of the relatively smooth development of HAWTs technologies as compared to VAWTs, there are some challenges that slow down their development in recent years [111].

First and foremost, it has been reported that the large-scale usage of wind power has influence on local and global climate by extracting the kinetic energy from atmosphere and changing the turbulence condition in the atmosphere boundary layer [60]. Fiedler and Bukovsky [27] investigated the effect of a giant wind farm on climate and precipitation. Their detected area adopted in the study was located both inside and outside the wind farm in the US, where 62 warm seasons were involved. They found that the precipitation increased by

1% in some parts within the detected region, because of the wind farm's obstruction for the advecting of drier air. Other researchers also got a similar result about climatic change due to the existence of large-scale wind farms. Except for the effect on the airflow, wind farms can affect the climate via altering earth's ground surface roughness. Daniel and Davidoff [63] investigated the effect of tropospheric wind fields on the surface roughness anomalies and it was found that the stability of surface climate was disturbed using model experiment.

In addition, large-scale deployment of wind energy provides significant challenges on wildlife conversation. In the last 20 years, some research programs focus on how wind farms affect the bird and bat populations have been carried out in the US and European countries [65]. These studies have proved that modern HAWTs that feature high tower, large blade, low tip speed and with lighting on the turbines increased the collision risks to birds. In addition, there is evidence that the loss of habitat for wildlife was associated with the construction of giant wind farms. Leddt and Higgins[29] found that the bird density of Conservation Reserve Program grassland without turbines is higher as compared to the regions with wind turbines constructed [67].

Except for the impact on environment, there are technological challenges for large scale HAWTs that worried experts in recent years. Firstly the augment of turbine blade increases the requirement for structured strength of the blades in order to withstand aerodynamic forces on the blades. Although carbon fiber is an ideal choice for blade material, which has enough strength and relatively less weight, the high cost makes it hard to be widely used [111]. In addition, although some VAWTs feature very simple structures, like H-type VAWTs, their aerodynamics is complex [54]. Because the VAWT blades experience a wide range of Reynolds incidence angles in one revolution.

## 1.2 Aerodynamics of VAWTs

### 1.2.1 Theories and Models

The mechanism of VAWTs is complicated, so one of the simplest type of VAWTs, H-type Darrieus turbine was chosen in this work for investigation. This is because it still has the fundamentals of unsteady aerodynamic characteristics common with other types of VAWTs.

The performance of a wind turbine depends on the power coefficient ($C_P$), which states the efficiency of energy transform from wind kinetic energy to mechanical kinetic energy by a wind turbine. The $C_P$ for conventional HAWTs is usually between 0.4 and 0.5 [25]. The

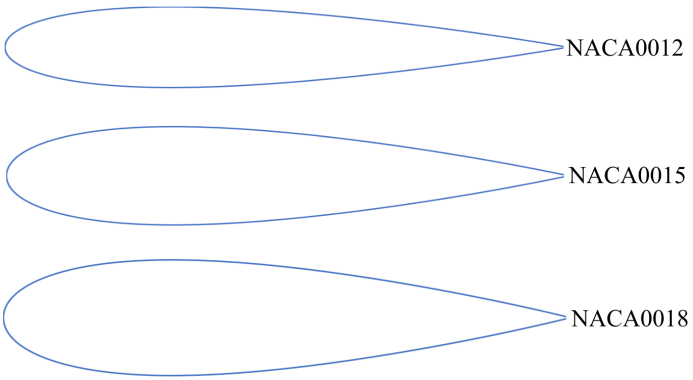


Fig. 1.12 Geometry of symmetric NACA aerofoils

$C_P$ for VAWTs depends on their configurations. But in most cases, the $C_P$ for a VAWT is smaller as compared to that of a HAWT of the similar scale.

### Aerofoil Selection

The selection and design of blade aerofoil section is one of the crucial factors in wind turbine design, especially for small- scale Darrieus turbines. It has been proved by several numerical and experimental studies that the aerodynamic efficiency of wind turbines is greatly affected by the blade aerofoil geometry. The data including lift, drag and pitching moment for the aerofoil in a wide range of incidence angles is needed for predicting the aerodynamic performance of a wind turbine [96].

The typical low speed aerofoils established by National Advisory Committee for Aeronautics (NACA), which are also called NACA aerofoils, were widely applied in the designs of VAWTs. Because NACA aerofoils had relatively high lift but low drag as compared with other aerofoils in the early times of VAWT development.

The NACA four-digit wing sections define the profile by four digits. The first one stands for the maximum camber in percentage of chord, the second one provides the distance from the leading edge to the maximum camber in tenths of chord and the last two numbers represents the maximum thickness of the aerofoil in percentage of chord. Among the NACA 4 digit aerofoils, the aerofoils whose first two digit is zero have symmetry contour. Most of Darrieus turbine blades are made of NACA symmetric aerofoil section, such as NACA 0012, NCA0015 and NACA 0018 as shown in Figure 1.12 [54] .

### Tip Speed Ratio

The tip speed ratio (TSR) is a parameter of great importance that indicates the characteristics of turbines. The definition of TSR is the ratio of blade tip linear velocity and wind speed. The expression of TSR is as follows:

$$\lambda = \frac{R\omega}{V} \tag{1.1}$$

where $\lambda$ = TSR, $\omega$ = Rotation velocity (rad/s), V = Wind speed. According to the magnitude of TSR, wind turbines can be classified as two categories: low ratio wind turbines and high ratio wind turbines. The maximum TSR for low ratio wind turbines is 2.5 and for high ratio ones the TSR can reach as large as 15. Almost all the modern wind turbines belong to the high ratio category.

### Moment Coefficient and Power Coefficient

The power coefficient $C_p$ is defined as the ratio of the mechanical energy extracted by a wind turbine and the total kinetic energy available in wind power. So the $C_P$ can be expressed as,

$$C_P = \frac{P_m}{\frac{1}{2}\rho S U^2} \tag{1.2}$$

where $P_m$ denotes the mechanical energy produced by the wind turbine, $\rho$ denotes the density of wind, S is the area of rotor, which is given as $\pi r^2$ (r is the radius of rotor for HAWT) and U denotes the free wind speed. For VAWT, the cross section area of the turbine is defines as S', which is 2RH for H-rotor, where H is height of the VAWT.

The moment coefficient $C_m$ is a parameter indicating the shaft torque produced by the turbine rotor that can be expressed as,

$$C_m = \frac{C_p}{\lambda} \tag{1.3}$$

where $\lambda$ is the TSR of the wind turbine.

### Betz Limit

Betz's theory was created by German Physicist Albert Betz in 1919. It is a basic law of wind turbine related to the efficiency of wind power utilization, which suggests that the maximum power that can be transformed to mechanical energy from wind energy by wind turbines.

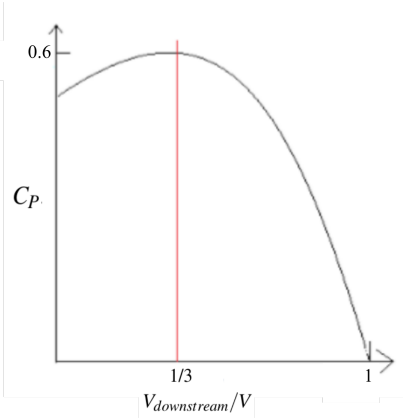


Fig. 1.13 Betz limit

According to Betz's theory, in an ideal condition, the largest ratio of energy extracted by the wind turbine from the kinetic energy in the wind is no more than 16/27 (around 60 %), which is called Betz limit for $C_P$ as shown in Figure 1.13. The theory is based on the actuator disk model and the law of conservation of energy.

An assumed ideal wind turbine is adopted for the generation of Betz theory. The flow is assumed to be continues, incompressible and free of viscosity. It is not hard to imagine that if all kinetic energy of wind is transformed to electrical power by the wind turbine, the wind velocity on the exit side of rotor is zero. However, this is a case of a maximum drag. For maximum power, the downstream speed for the turbine is 1/3 of the upstream (wind) speed as will shown later. It is a result of the power proportional to the air mass flow rate going pass the turbine.

### Blade Solidity

Solidity is one of the most crucial parameter that influences the aerodynamic performance of VAWTs [68]. The solidity $\sigma$, is simply defined as followed:

$$\sigma = \frac{Nc}{d} \tag{1.4}$$

where N is the number of blades, c is the blade chord length and d is the diameter of the rotor. So the solidity states the ratio of the blade area and the turbine swept area. The value of solidity lies in a very large range that depends on the size and the style of wind turbines. Usually the optimum power coefficient increases with solidity [64]. The choice of solidity is an important step in wind turbine design. The definition of solidity indicates that it can be

altered by changing either the blade length to turbine radius ratio or the number of blades [18].

## 1.3 Motivation Objectives and Achievements

The aerodynamic stall of rotor and the flow separation on the turbine blades degrade the performance and efficiency of wind turbines. In order to improve the power coefficient, extend the operating range of tip speed ratio and increase the stability of VAWTs, extensive redesign of turbine blades and implementation of flow control techniques need to be conducted as detailed above.

Although much investigation of flow control techniques have been carried out to control dynamic stall in VAWTs by researchers in recent years, a large number of studies focused on the active flow control devices, such as the plasma actuator and active flexible blade. However, extra power is required on these external energy resources for the active flow control devices that adopted in wind turbine systems that increase the cost on installation and maintenance. Therefore, the application of passive flow control methods are relatively more practical for wind turbine systems.

In addition, considering the relatively less research on vertical axis wind turbines as compared to horizontal wind turbines, the modification of turbine blade aerofoil section using flow control devices is a relatively new topic. The implementation of passive control devices can suppress the flow separation and delay the occurrence of rotating stall. Additional benefit may be achieved such as the reduction of noise level.

The aim of this research is to improve the aerodynamic performance of a small scale H-type Darrieus wind turbine via some flow control techniques. This project focus on the small VAWT where the Reynolds number is between 100k to 300k when based on the chord length of the aerofoil. At this range of Reynolds number, the blade profile is dominated by laminar boundary layers that prone for flow separation [103]. Hence, the noted flow control approaches of MVG or Gurney flap can be effective. Also, VAWTs are popular for the small to medium range of Reynolds number and hence such study has the potential to achieve high impact. Studying higher Reynolds number blades dominated by turbulent boundary layer is left for a future project.

The project aim can be achieved by the following objectives:

1) Simulate the flow around clean NACA 0018 aerofoil and H-type VAWT using the URANS and LES approach.

2) Conduct a two dimensional numerical study of the Gurney flap on a NACA 0018 aerofoil and a small scale H-type VAWT.

3) Investigate the effect of the MVGs on NACA 0018 aerodynamic efficiency for a wide range of angle of attack using high performance simulations. Furthermore, simulate and study the effect of the MVGs on the H-type VAWT.

4) Computationally study of the effect of leading-edge serration on the performance of a straight stationary blade of VAWT and a small scale VAWT.

All these objectives were successfully achieved, resulting in the dissemination activities details at the start of the thesis.

## 1.4 Thesis Outline

This thesis is organized into seven chapters. The first chapter gives an overview of the research problem related to the flow control techniques in vertical axis wind turbine. The second chapter provides a review of the investigation and application of the flow control methods in previous study. The difficulty points in research and some of the questions that have not been answered are also point out. The third chapter describes the numerical methods adopted in this work. The fourth chapter focuses on the study of Gurney flap. The Numerical simulation was performed on the two dimensional aerofoil NACA 0018 and H-type Darrieus wind turbine made of the same aerofoil. Mesh sensitivity study and code validation were conducted to determine the mesh resolution and validate the RANS method. The fifth chapter presents the numerical study of micro vortex generators. The MVGs of various designs implemented on the suction surface of an isolated blade and the whole VAWT was numerically investigated. The rotating stall and power generation of the modified turbine is compared with the unmodified case and the optimum configuration of MVGs is determined. The sixth chapter presents the study of aerodynamic performance of the leading-edge protuberances applied on the isolated blade and the VAWT. The development of the "bi-periodic" phenomenon was visualized by streamline patterns on the modified blade. The seventh chapter concludes the thesis and provides suggestions for the future work.

# Chapter 2

# Literature Review

Flows around the wind turbine are among the most complex flows encountered in fluid dynamics practices, which is inherently unsteady, due to the motion of the rotor. The boundary layer shows various states: laminar, transitional and turbulent. The transition might be caused by flow separation. As the result, the working mechanism of flow control techniques is complex for wind turbines. In order to successfully predict the performance of wind turbine, decide the blade load and power output, the investigation of their aerodynamics in all working states is necessary [38]. Understanding the flow mechanics in wind turbines thoroughly and easily, the analysis of flow around an isolated aerofoil is useful, which directly determines the overall performance and efficiency of the wind turbine system.

This chapter presents a literature review of aerodynamic analysis for aerofoils and VAWTs, especially focusing on the flow control methods for the improvement of their performance and efficiency. A review of numerical methods on solving these unsteady flows is also provided.

## 2.1 Aerodynamic performance of low Reynolds number aerofoils

### 2.1.1 Numerical Study of an Isolated Low-speed Aerofoil

The research on VAWTs is less advanced than that of HAWTs, which has limited the development and implementation of VAWTs [16]. Through the rotor cycle flow separation and stall occur when the blade profile is subjected to a high incidence angle. The flow

experiences a laminar separation bubble if the separated flow is reattached for low Reynolds number flow, while at stall massive flow separation occurs.

### Laminar separation bubble on low-speed aerofoil

The aerofoil experiences several flow features on its suction surface at low Reynolds numbers and high angle of attack as shown in Figure 2.1. Firstly, the laminar separation occurs near the leading edge of the aerofoil because of surface curvature and an adverse pressure gradient. After the leading edge small separation bubble, the flow reattaches and depending on the Reynolds number continues as a laminar boundary layer or goes through a transition process to turbulent boundary layer. For low Reynolds number conditions as focused in this study, the boundary layer continues as laminar until reaching boundary layer separation bubble due to adverse pressure gradient. This is called as the laminar separation bubble (LSB).

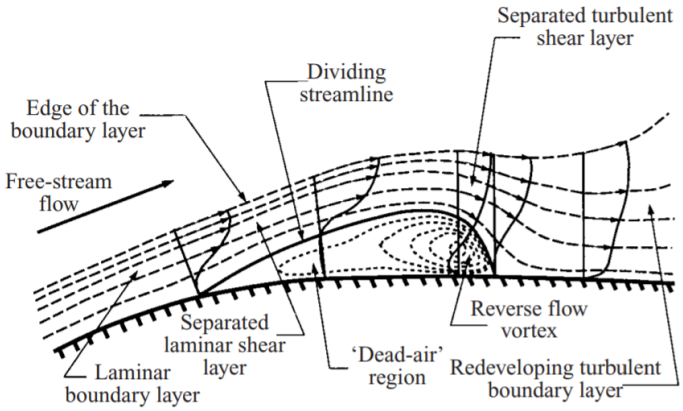


Fig. 2.1 The mean flow structure of laminar separation bubble [49]

The laminar separation bubble is the main obstacle for achieving good performance for aeorfoils at low Reynolds numbers and high incidence angles. McGranahan and Selig [78] conducted the measurement of upper-surface flow features of seven aerofoils to determine the separation and reattachment point at the Reynolds numbers ranging from $2 \times 10^5$ to $5 \times 10^5$.

The oil-flow visualization technique was executed and the good agreement obtained as compared to the experimental results from NASA. It was found that the performance of low-speed aerofoil is dominated by laminar separation bubble at Reynolds number below $2 \times 10^5$. The wind tunnel test was conducted on the E387 aerofoil by Mcghee et al. at the Reynolds number ranging from $6 \times 10^4$ to $4.6 \times 10^5$ [77]. The pressure model was tested to achieve the aerofoil surface pressure measurement in order to obtain the lift, drag and pitching moment data. The results indicate that Reynolds number and incidence angle are key factors that influence the condition of laminar separation bubble. It is also interesting to

note that at Re= $6 \times 10^4$ two different flow phenomena, laminar separation with and without turbulent reattachment, could be observed at the incidence angle ranging from 3° to 7° [77].

### Aerofoil static stall

Stall is a typical nonlinear phenomena in aerodynamic engineering. The static stall occurs around a static aerofoil when the incidence angle reaches a critical value, resulting in the dropping of lift and increasing of drag dramatically [75].

Liu et al. [75] analyzed the origin and development of the static stall of the NACA 0012 aerofoil in detail at Re=1000. The AoA starts from a low value. At $\alpha < 5°$, there is no flow separation and the streamline is stay attached on the surface of the aerofoil. When the AoA increases to 6°, there is a small separation vortex near the trailing edge of the aerofoil. Figure 2.2 (a) presents the streamline pattern around the aerofoil at $\alpha = 7°$, corresponding to the steady conditon of flow. If the AoA is larger than 8°, the lift and drag start to fluctuate periodically due to the trailing-edge vortex shedding. The amplitude and frequency of the oscillating become larger with the increase of AoA. When the AoA further increases to 26°, the flow shows unsteady behavior with unperiodical vortex shedding as shown in Figure 2.2 (b). At $\alpha = 29°$, the scale of separation almost cover the whole surface side of the aeorfoil and the vortex shed frequently, resulting in significant lift decline . This situation is considered as static stall phenomena.

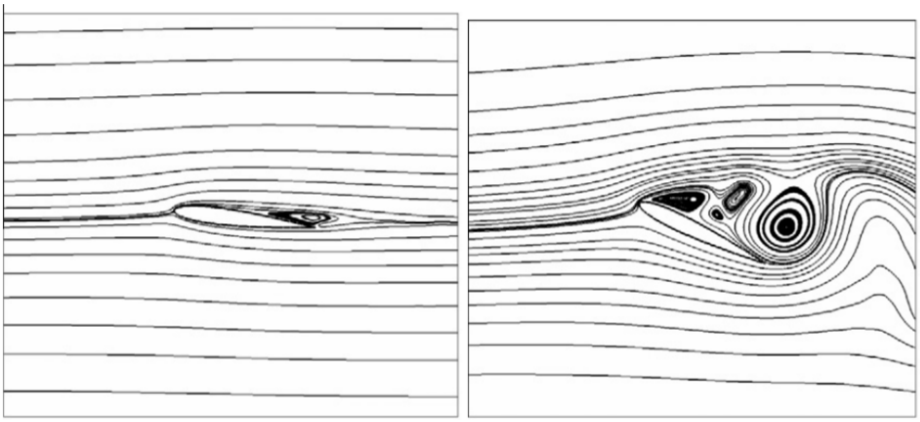

Fig. 2.2 Instantaneous streamline around a static airfoil at $\alpha = 7°$ (right) and $\alpha = 26°$ (left) [75].

Despite of the angle of attack, the stall condition depends on the section shape, thickness ratio and the operating Reynolds number [48]. Hoerner classified flow separation into three categories: leading edge separation-long bubble type, leading edge separation-short bubble type and trailing edge separation. Each of the three types has a distinct behavior as

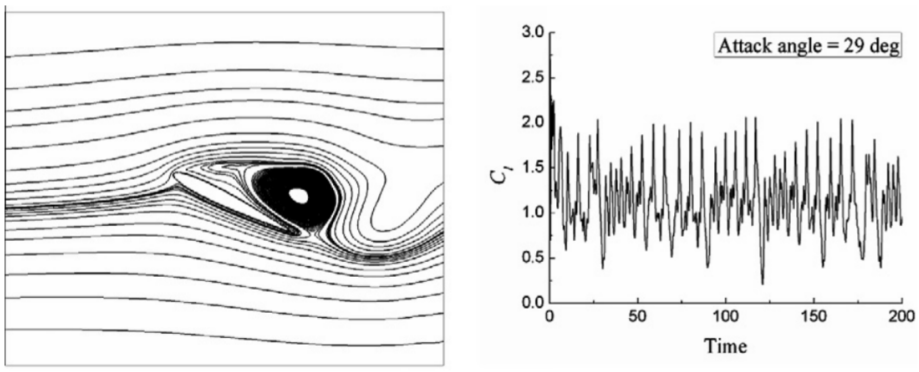


Fig. 2.3 (a)Instantaneous streamline around a static airfoil at $\alpha = 29^\circ$. (b) Time history of lift coefficient at $\alpha = 29^\circ$ [75].

characterized by the variation of lift as a function of AoA [48]. The leading edge separation-long bubble type separation is a gradual laminar separation and reattachment process occurs on thin sections. The leading edge separation-short bubble type separation is a sudden stall with bubble bursting of a section with round nose and low camber. The trailing edge separation is originated from trailing edge as discussed in the last paragraph.

**Aerofoil aerodynamic stall**

When the aerofoil experiences oscillatory conditions as in VAWT, the stall is of dynamic nature and is different from the static stall of a single aerofoil at high angle of attack. The prediction of dynamic stall is important for the performance of turbomachinery, aircrafts and wind turbine applications [23]. This unsteady conditions has been studied for many years. The complicit of flow mechanics in dynamic stall present significant barrier and challenges in the research of both experiment and Computational Fluid Dynamics (CFD). The prediction of dynamic stall mainly relied on empirical or semi-empirical methods in last century [23]. With the significant progress of CFD and supercomputers, the capacity of turbulent and flow transition modeling was improved. The definition of dynamic stall firstly introduced in helicopter industry due to the oscillations of the blades, which degrades the performance and stability of helicopters [2].

The early experimental study of dynamic stall could be traced back to 1970s. Mccroskey et al.[76] carried out a wind tunnel test on aerofoil NACA 0012 to investigate the dynamic stall and unsteady boundary-layer separation at moderately large Reynolds number of $2.5 \times 10^6$. Different styles of flow separation obtained by modifying the leading edge of NACA 0012 aerofoil in three ways(sharp leading edge, reduced leading edge radius and ONERA 0012 camber). The authors indicate that the dynamic stall is not originated from the bursting of the

laminar separation bubble but from the unsteady separation of turbulent boundary layer [76]. In addition, they determined the predominated difference between static and dynamic stall is vortex shedding. The process of vortex shedding in all three oscillating aerofoil models were examined at the same incidence angles and the different leading edge types lead to a significant difference in dynamic force and moment.

Recently, much research is focused on the numerical methods that were applied to study this phenomenon and mechanism of dynamic stall. Wu et al. [120] compared three turbulence models in predicting the flow dynamic characteristics of aerofoils using 2D and quasi-3D RANS solver. It was found that for attached flows the numerical results of all three turbulent models are in agreement with the experimental results, while in separated flows there is no good correlation with measured data. A 2D study was carried out in viscous laminar flow over oscillated NACA 0012 aerofoil using a vortex method by Akbari and Price [2]. It was found that oscillating the aerofoil can delay the flow separation to a higher incidence angle as compared to the steady aerofoil. The effect of parameters including Reynolds number, incidence angle, location of pitch axis and different frequency of oscillation of the airfoil were compared with each other. Among them, the reduced frequency of oscillation of the airfoil had relatively large effect on flow separation and dynamic forces of the aerofoil. The maximum normal force was also much affected reduced frequency. On the other hand, the Reynolds number had the least influence on the flow field.

### 2.1.2 Flow Control Methods on Aerofoils

Nowadays, there are several approaches to improve the aerodynamics of wind turbines and overcome the drawbacks of the design of wind rotors in order to maximize energy capture and increasing the reliability, such as the optimization of blade shape, adding intelligent control system and improving the configuration of the generator. Among them, flow control of wind turbine blades is one of the widely used technique to improve the power coefficient of rotors, which is also applied to many other research fields, like aeroplanes.

Much research has been devoted towards the development of flow control methods concerned with improving lift, reducing drag, delaying flow separation and lowering noise for aerofoils.

#### Flow control of aerofoils using Gurney flap

The Gurney flap is named after its creator, Dan Gurney in 1970. He installed a piece of metal on the rear wing of his racing car to increase the down force, which is the prototype

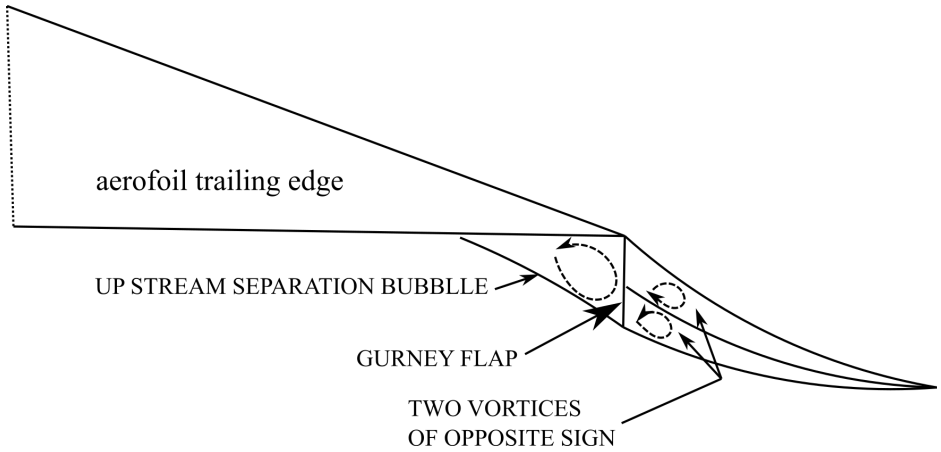


Fig. 2.4 Gurney flap on the pressure side of an aerofoil [72].

of modern Gurney flap. The Gurney flap was firstly applied to the area of aerodynamic engineering by Liebeck in 1976 on a Newman aerofoil, who named it as "Gurney flap", after it was used in the field of racing for many years. He found that the Newman aerofoil with a Gurney flap of 1.25 % aerofoil chord length (c) has a higher lift coefficient and lower drag coefficient as compared with the clean aerofoil.

The Gurney flap is usually perpendicular to the chord line of aerofoil as shown Figure 2.4. Its length is usually 1% to 5% of the chord length. Many wind tunnel tests and numerical simulations have been conducted on aerofoils with Gurney flap of different length. It was found that this simple device can improve the performance of an aerofoil significantly.

Two mechanisms lead to the increase of lift. One is related to the attached flow. As the Gurney flap delays flow separation, increasing the region of attached flow to the aerofoil. The other mechanism is concerned with the momentum. As compared to the clean aerofoil, the aerofoil with a Gurney flap has a larger exit flow angle, which means that the change of momentum of flow the aerofoil is larger. So according to the Newton third law, the lift component of the force on the aerofoil with Gurney flap is larger.

Furthermore, the Gurney flap has influence on the drag of the aerofoil. Flow moves along the aerofoil on its pressure surface near the trailing edge. When the flow hit the flap, which increases the drag of the aerofoil. On the other hand, the separation delay can reduce pressure drag. Normally in most cases the former effect is larger than the latter one. So the drag is increased. However, for very thick aerofoils, the separation delay effect is much more significant and the drag is decreased.

There had been a large amount of study on the Gurney flap of different aerofoils, especially 2D models. It was found that the Gurney flap can be used in a wide range of angles of attack

to improve the lift of the aerofoil and delay the occurrence of separation. Although it also increases the drag coefficient ($C_D$) to some extent. However, in most cases the lift-to-drag ratio is still increased [108].

Gurney flaps (GFs) have been widely used as flow control devices on low-speed aerofoils, supersonic aerofoils and modern aircraft designs. The study on GFs can be traced back to more than forty years ago. The GFs' function of lift enhancement for the subsonic aerofoil was verified by Liebeck [72] in 1978. He carried out a wind tunnel test of Gurney flap with the height of 1.25% chord length on the Newman aerofoil. It was found that the GFs provided increased lift and reduced drag of the aerofoil at a given angle of attack. Although the detailed flow mechanism was not completely understood at that time, how the GFs affects the flow near the trailing edge of the aerofoil was hypothesized as Figure 2.5 (a). The flow structure was verified by Date et al. [19] via numerical method as Figure 2.5 (b). The detailed mechanism of GFs has been discussed in the previous chapter. The GFs are mainly used as a lift enhancement technique on high-lift aerofoils. Many research have been verified that the GF is an effective device for high-lift design although there is a drag penalty associated with the lift increment.

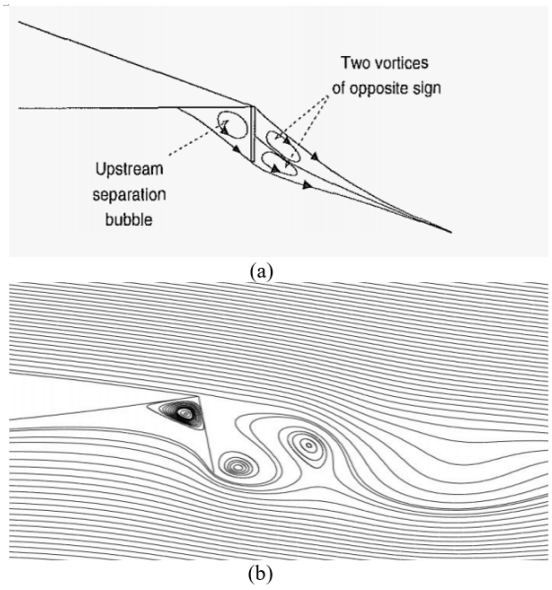


Fig. 2.5 (a) Hypothesized flow around Gurney flap [56].(b) Flow streamlines around Gurney flap by numerical simulation[19].

GFs applied on water applications were studied by researchers as well. The water tunnel test of several GF configurations attached to a wing with the section of NACA0012 aerofoil was carried out by Neuhart at low Reynolds number 8588. Four GF geometry with different lengths and configurations were tested. Except for the conventional GFs of smooth structure,

the GFs with serrated structure along the spanwise direction was investigated. The flow visualization data around trailing edge of the aerofoil was recorded during the tests. The visualized flow structure substantiated the hypothesized flow field proposed by Liebeck [72]. It was also found that the larger GF had better performance on flow separation control. It should be noted that unlike the wind tunnel tests conducted before, a Reynolds number that was lower several magnitude was chosen in this work. As a result, the characteristics of vortices and flow separation are different with the flow field of higher Reynolds numbers. However, the GFs have the similar effect on the suppression of flow separation and lift enhancement at both low to medium ranges of Reynolds numbers.

So far the studies on GFs mainly were limited to an mounting angle of 90° and to the location at the trailing edge of aerofoils. Li et al. [71] proposed an experimental study to determine the effect of the mounting angle and location of GFs. The low speed wind tunnel test was conducted on a NACA 0012 aerofoil and the Reynolds number based on chord length was $2.1 \times 10^6$. The configuration of GFs are as shown in Figure 2.6, where $\Phi$ denotes the mounting angle of GFs. The tested mounting angles were 45°, 60° and 90°. The results indicate that the GFs with all the three mounting angles have positive influence on lift enhancement . Among them 90° is the optimum mounting angle that provides the largest maximum lift for the aerofoil, while the lowest drag penalties achieved in the case of $\Phi = 45°$. In terms of the location of GFs, the aerofoil with a GF that farther from the trailing edge has a relatively lower lift and a higher drag as compared to the case in which the GF was attached to the trailing edge of the aerofoil at the incidence angle ranging from 2° to 10°.

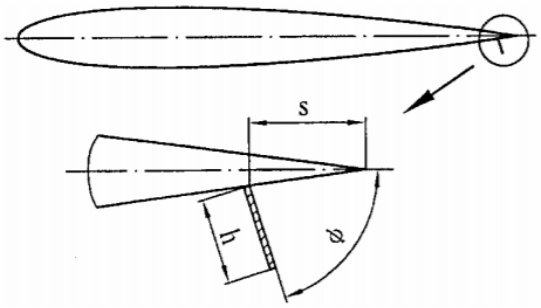


Fig. 2.6 Configuration of Gurney flap [71]

The study of GFs in high-speed flow condition is rare by now. The function of flow control on a NACA0012 airfoil was studied by Li et al. [69] via Wind tunnel experiments at Ma=0.7. Four GFs of various lengths ranging from 0.5% to 2.0% chord length were tested. Similar to the low-speed profiles, the addiction of GFs increased both the lift and drag of the aerofoil at incidence angles ranging from 2° to 8° as compared to the clean aerofoil. The

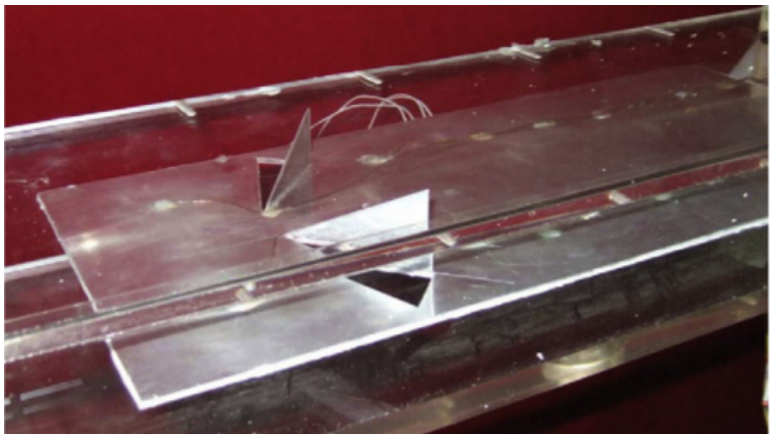

Fig. 2.7 Vortex generators mounted on the flat plate in the wind tunnel[119].

maximum lift and maximum lift-to-drag ratio increased with the GF length. Furthermore, the larger GF corresponded to a larger slop of the lift curve and the same result can not be found in the cases of the low-speed aerofoils. It should be note that the mechanism of GFs under high-speed circumstances has unique characteristics that are different from the low-speed aerofoils. The GF could move the shock position downstream on the suction side of the aerofoil.The enlargement of the supersonic region leads to the lift increment. Moreover, the installation of GFs increased the pressure on the pressure side of the aerofoil that also had a positive influence on the lift improvement.

**Flow control of aerofoils using micro-vortex generator**

Vortex generators (VGs) are popular aerodynamic devices used for flow control in a wide range of area, such as aircraft and wind turbines. The development of vortex generator has a long history of more than 50 years and it was firstly used on the wing of the aeroplane by Boeing to prevent boundary layer separation.

The vortex generator (VG) consists of a small vane attached to the aerofoil of wings and turbine blades as shown in Figure 2.7. The main mechanism of VG is that when the aerofoil moves in the fluid, the device can introduce the flow outside into the inner boundary layer and thus delay flow separation. The boundary layer can become turbulent much earlier and thus increase the skin friction. The generators can also increase drag by its own presence (parasite drag). Hence, vortex generators should be used with caution. Nevertheless, they can still improve the blade aerodynamic efficiency, i.e. lift-to-drag ratio. The shape of the VGs are normally rectangular and the height is the same as the height of boundary layer [109].

In recent years, a new style of VG called Micro Vortex Generator (MVG) has attracted more attention from researchers. This device is smaller than normal VGs, which is usually lower than 50% of the height of boundary layer. It is used for introducing the fresh flow from outer to the inner boundary layer in order to suppress flow separation. Because the MVG is much smaller than VGs, so that the parasite drag is much smaller. However, this requires further careful design of its size and location [46].

VGs and MVGs have been widely-used as flow control devices for various aerodynamic applications, especially in the wind turbine industry for many years. Taylor [110] proposed a simple device installed in a diffuser, which consisted of a row of small plates projecting normal to the surface at an incidence angle to the free stream airflow. They were also used for enhancing wing lift, reducing noise generated by airflow separation and reducing afterbody drag of aircraft fuselages [14].

Many modern aerofoils operate in the conditions of low Reynolds number based on chord length ($< 10^6$). At high incidence angles before stall the aerofoil experiences a laminar separation bubble due to adverse pressure gradients that degrades the performance of the aerofoil. The separation bubble forms downstream where the laminar flow separation occurs[73]. The turbulent boundary laryer induced by that cause large drag increase. The effect of passive vortex generator on reducing the laminar separation bubbles and the behavior of vortex have been investigated by previous studies.

Heffron et al. [44] presented a numerical investigation to suppress the separation bubble on a Eppler e387 low Reynolds number aerofoil using a rectangular MVG vane of three different design angles. The chord Reynolds number of the aerofoil was $2 \times 10^5$ at an incidence angle of $\alpha = 12^\circ$. The MVG vane was placed at 30% chord length from leading edge on the suction side of the aerofoil. The height of it was 10 % chord length that is totally contained within the turbulent boundary layer. Three different installation angles were tested, $14^\circ$, $18.5^\circ$ and $23^\circ$. Although a larger installation angle of the MVG introduced higher initial circulation strength of vortex, the decay rate of vortex was relatively high, which could offset the benefit brought by large initial circulation strength. The optimum mounting angle of MVG vane was identified as $18.5^\circ$, which provided a relatively high initial circulation strength of vortex but moderate decay rate.

In order to extend the application of MVGs on wind turbine systems, the optimization the geometry of MVGs is required. A pair of triangular MVGs with counter-rotating distribution applied on turbine aerofoil S809 at $\alpha = 15^\circ$ was numerically investigated by Yashodhar et al.[123]. Figure 2.8 (right) presents the configuration of MVGs that are placed just upstream of separation point. It was found that for a clean aerofoil the separation occurred near the

trailing edge of the aerofoil and after the separation point, the shear stress started decreasing. In comparison of unmodified case, the installation of MVGs could continuously increase the shear stress that denotes a large skin friction and the suppression of flow separation. The flow field visualization of both clean and optimized aerofoils at stall angle along the streamwise direction are shown in Figure 2.8 (b). It is clearly seen that the clean aerofoil experience large flow separation on its trailing edge. However, the vortex region on the modified aerofoil was suppressed due to the existence of MVGs.

Over the years, high-lift devices have attracted more attention form researchers. The MVGs could be also applied to high-lift aerofoils where the maximum lift value required to be maintained while controlling flow separation. Lin et al. [74] carried out experimental investigation on the performance of vane-type MVGs placed on a multielement aerofoil. MVGs of both co-rotating and counter-rotating configurations were tested in the wind tunnel. It was found that MVGs of both configurations had a positive effect on the flow separation. The optimum lift could be achieved when the MVGs were as small as 0.18 % of the chord length. The optimum location of MVGs was identified as well. The MVGs placed at 25 % chord length provided relatively higher lift with a smaller drag penalty.

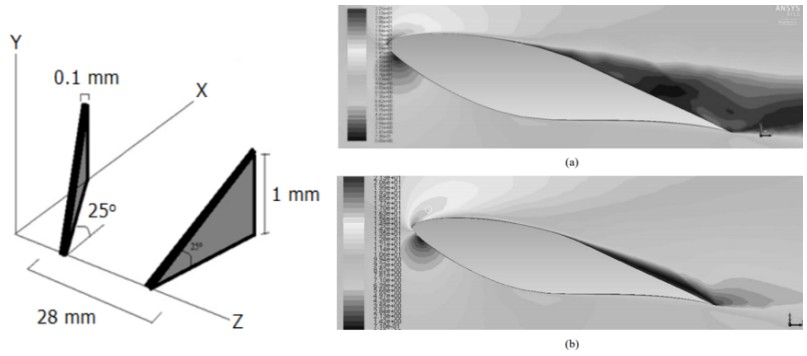


Fig. 2.8 Configuration of MVGs (right). Spanwise flow field (left), (a) clean aerofoil, (b) modified aerofoil. [123]

Reducing the large drag for improving the aerodynamic performance of the highly swept wings for aircrafts is a great challenge for researchers. Ashill [5] presents a flow control technique using the miniature wire segments as low-profile VGs applied on the highly-swept wing with drooped leading edges. The low-speed wind tunnel test was performed on the wings with fixed or variable camber. It was found that the installation of MVGs reduced the drag of fixed-camber wing by at most 50%.

Fig. 2.9 Leading edge serration of an aerofoil [42].

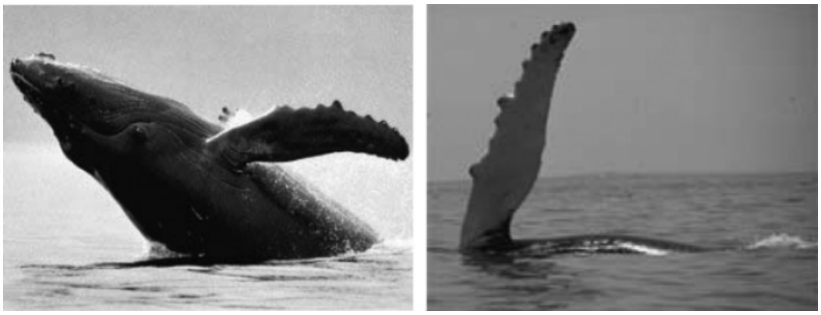

Fig. 2.10 Model of humpback whale flipper [58].

**Flow control of aerofoils using leading-edge serration on the aerofoil**

Leading edge serration is another passive flow control method for aerofoils to enhance their aerodynamic performance. Leading edge serration means that the wave serration is employed on the leading edge of a blade along its spanwise direction as shown in Figure 2.9.

The modification of leading edge was inspired by the previous research of marine biologists about the humpback whale flipper as shown in Figure 2.10 [29] [28]. It was found that the leading edge protuberance is effective in stall delay and lift enhancement around stall incidence angle. The device is also beneficial in noise reduction for aircraft and turbine blades. The working mechanism of leading edge serration lies in the generation of streamwise vortices that can improve the momentum exchange within boundary layer.

Several studies on this method have been undertaken recently. The sinusoidal wave serration is the main choice for leading edge modification. Johari et al.[58] presents a water tunnel test to indicate the effects of leading-edge sinusoidal wave protuberances on aerofoil performance by evaluating its lift, drag and pitching moment in a wide range of incidence angles from $-6^\circ$ to $30^\circ$. The protuberances of three amplitudes with two spanwise

wavelengths were discussed in this work and were compared with the original 63-021 aerofoil. The measured lift and drag as the function of incidence angle are shown in Figure 2.11. In the base line, the $C_L$ continues increase with the improvement of $\alpha$ before a sudden drop at the stall incidence angle of 21°. For the aerofoils with leading-edge protuberances, the $C_L$ follows the similar trend with the base line at low incidence angles from $-6°$ to nearly 12°. After that, different from the base line, the $C_L$ is nearly constant until $\alpha = 24°$. As shown in Figure 2.11, the modified aerofoils have higher lift at post stall region for the base line, although the maximum lift is reduce due to the leading-edge protuberances. In terms of drag coefficient, the $C_D$ keeps increasing at a similar rate without any significant turning, while in the base line the increasing rate of $C_D$ rises until near stall incidence angle. Similar result of pressure distribution was obtained by Skillen and Revell [106] by numerical method.

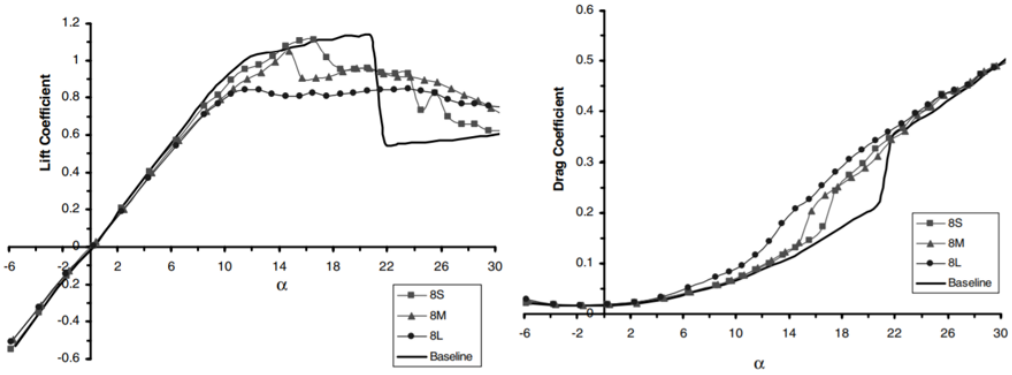


Fig. 2.11 The comparison between the aerofoil with leading edge serration and unmodified aerofoil in terms of lift (right) and drag (lift) coefficient [58].

The serration of jagged shape also has beneficial effect on the performance of aerofoils as shown in Figure 2.12. Collins [17] carried out subsonic wind tunnel test on low-speed wings with sections of NACA 2412 and NACA 0015 aerofoils at the Reynolds number ranging from $3 \times 10^5$ to $6 \times 10^5$. It was found that the serration affected the distribution of pressure coefficient ($C_p$) distribution significantly. The $C_p$ of suction surface decreased and that of pressured side increased at $\alpha = 10.63°$. As a result, the pressure difference between two sides of the aerofoil increased, pointing to lift enhancement. In addition, the stall angle of modified aerofoil was improved by around 1°.

Furthermore, the leading-edge serration is used for reducing the noise radiated from aerofoils [47]. Hersh et al. [47] conducted the acoustic investigation of NACA 0012 aerofoil with a variety of serrations on its leading edge in low Reynolds number flow by numerical simulation. It was found that the tones generated from vortex shedding near trailing edge was

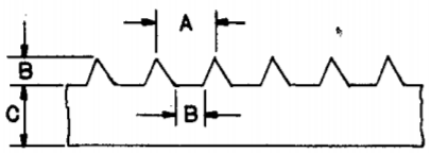


Fig. 2.12 The geometry of Jagged-shaped serration [17].

reduced or eliminated after the application of leading-edge serration at low incidence angles. Because the serration produced chordwise trailing vortices that affected the behavior of vortex. The broadband noise due to the dynamic stall decreased as well by this optimization of aerofoil. The noise from turbulence shock on the leading edge of aerofoil was studied by Roger rt al.[92]. He applied leading-edge serration and porous materials on the NACA 0012 aerofoil to control the turbulent noise by both wind tunnel test and modeling approaches. It was found that the leading-edge serration could degrade the noise level and a maximum reduction of 10 dB was achieved.

Howe [50] discussed the effect of serrated trailing edge on the sound level cause by the turbulent flow via numerical methods. The aerofoils of a variety of chord length in terms of the characteristic acoustic wavelength were investigated in this work. The result indicates that a properly designed serration could reduce the level of the noise with a certain frequency spectrum near the trailing edge of the aerofoil.

**Active flexible wall**

The active flexible wall is a device installed on the surface of wings or blades on its suction side [104] as shown in Figure 2.13. As more laminar flow is desirable for the aerofoil of high performance, the main goal of this device is maintaining the laminar flow on the surface of the aerofoil. This device consists of a thin membrane and there is an array of strips on it. As it is thin enough, it has no influence on the system when it's not actuated.

The mechanism of the active flexible wall is used for detecting the flow separation and then introduce small disturbances into the boundary layer, which can help resist the flow separation. When the device is in the sensor mode, it is inhibition and has no influence on the airflow. But it can monitor the beginning of flow separation. When it detects the trend of separation, the second mode starts up. The membrane starts to vibrate , causing small disturbance in the airflow. The transducers can detect and judge where the separation happens and decide which strip to vibrate and its frequency to prevent the flow separation[104].

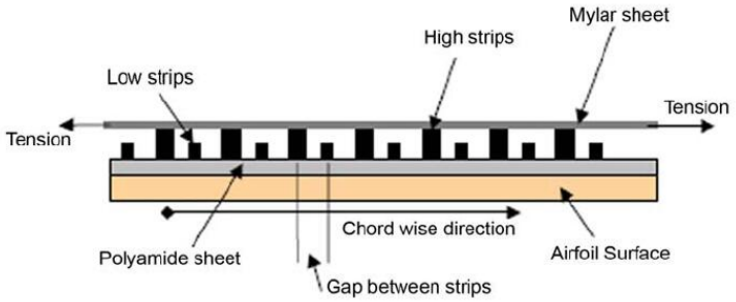


Fig. 2.13 Schematic of the AFW[112].

The study on active flexible wall has been conducted by many researchers, because of its superiority compared to other active flow control devices. The most attractive advantage is that its volume is small enough and has no influence on the system when it's not working. There is no complicated mechanical configuration and almost no extra weight to the wings or blades. Sinha [105] investigated the optimization of lift-to-drag ratio enhancement of wings of sail plane by flexible wall. It was found that the ratio $L/D$ increased nearly 100 % due to this device.

**Plasma actuator**

The plasma-based device is a very promising method of flow control for wings or aerofoils of aircraft and wind turbines. The earliest research conducted on this device was in 1950s, although there has been a few publications about that for a long time after that. There are two electrodes in the plasma actuators that are settled on the aerofoil surface. Between the two electrodes there is a high-voltage AC signal, which can make the air in the electric field weakly ionize as shown in Figure 2.14. The ionized air introduces a body force to drive the nearby air, which can help to modify the airflow in the boundary layer.

The main goal of the device is flow separation delay. Compared to other active flow control devices, Plasma actuator has some advantages. The most attractive one among them is its simple configuration that adds no extra weight to the wings and blades. This device only has small volume as well as low noise. Additionally, there are no mechanical parts that easy to break down. This device doesn't need any storage for high-momentum air as well. Furthermore, it has a fast response and easily to be controlled.

These advantages of plasma actuators discussed above attracted more attention from researchers in recent years. Post and Corke [89] applied the plasma actuator on the NACA 0015 aerofoil that periodically oscillated. They studied its effect on the leading-edge separation and stall control. It was found that all styles of plasma actuators can improve the lift

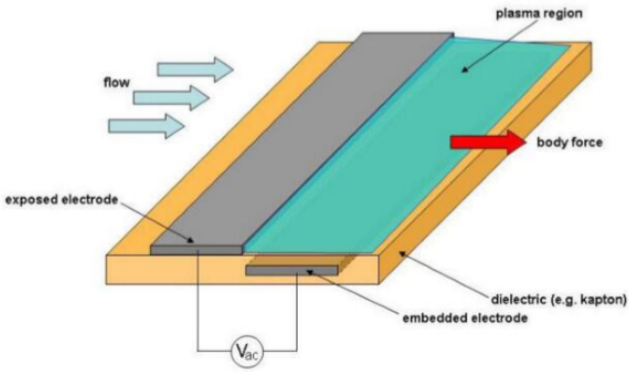


Fig. 2.14 Plasma actuator configuration [83].

and the steady actuator can remove the sharp drop of lift in high incidence angles. Huang and Corke [52] investigated flow separation control on the wind turbine blades using plasma actuator at low Reynolds numbers. Two locations of the plasma actuator were examined, 40% and 67.5 % chord length. They found that the device was effective in both location. But the plasma actuator that was installed near the separation location was more effective. Furthermore, They compared the performance of plasma actuators with vortex generators and discussed the advantages of both.

### Shape change aerofoil

Shape change aerofoil is also called adaptive aerofoil. The camber of the aerofoil changes in working by mechanical configuration. The main goal of this device is maintaining the high performance of aerofoils when flow conditions change, making the aerofoil can adapt a wide range of working environment.

Usually the adaptive aerofoil consists of a flexible upper surface. Currently there are two common methods to achieve the shape change. One is using the smart material actuators and the other is relying on compliant mechanisms as shown in Figure 2.15. Sometimes the shape change configuration can combined with vortex generators.

Although the development of adaptive aerofoil is not mature because of its complicated mechanism, some research has been conducted in both experiment and numerical simulation. Roh and Kim [93] studied the effect of adaptive aerofoil with shape memory alloy actuator in improving the aerodynamic performance by numerical method. They also compared the result with the aerofoil with different style of flaps. It was found that the adaptive aerofoil is more effective than the structure of a plain flap and a slotted flap.

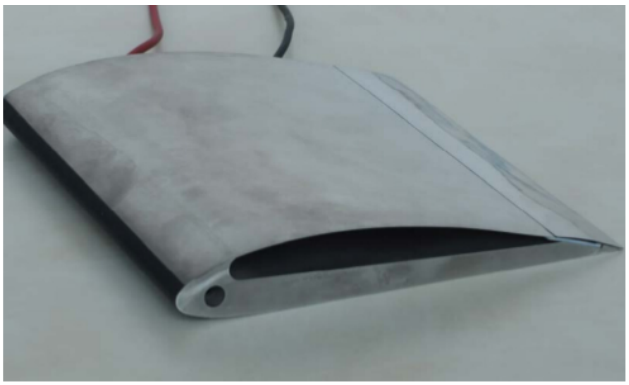

Fig. 2.15 Shape change aerofoil[20]

**Blowing and suction**

Blowing and suction are popular boundary layer control methods for aircraft and turbo-machines as shown in Figure 2.16. Suction has a longer history compared to the blowing method, because of its simple configuration. The mechanism of suction mainly has two aspects [112]. One is that the suction can remove the decelerated fluid near the surface within boundary layer. The other effect is to reflect the high-momentum fluid to the boundary layer, which can reduce the possibility of flow separation. However, the extra weight and mechanical complexity brought from this device may offset its advantages. Further research is needed for an optimized device of better performance.

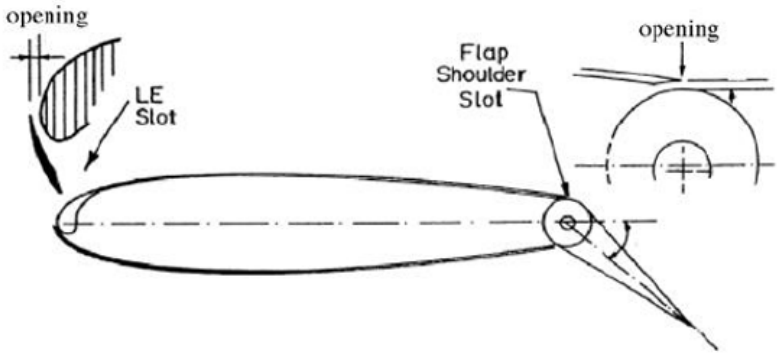


Fig. 2.16 Blowing/Suction configuration showing slot locations and deflectable flap [112].

The mechanism of blowing is introducing fluid of high-momentum into boundary layer, which can help overcome the adverse pressure gradients. This device usually consists of a slot on the surface of both leading edge and trailing edge of aerofoil for wings or blades, which stored accelerated fluid. However, the presence of slot may increase drag force and degrade efficiency of the aerofoil [112].

## 2.2 Aerodynamic Performance of Vertical Axis Wind Turbines

Increasing interest is being paid on the aerodynamic analysis and optimum design of vertical axis wind turbine by means of CFD and experimental measurements. In the last decades, a large number of studies were carried out to investigate the flow control techniques to control dynamic stall which is the dominate flow characteristic in VAWTs operation [116]. In order to determine effective methods to improve the performance and efficiency of the VAWT, an in-depth investigation on the aerodynamic behavior of turbine blades especially for the stall and post stall condition is required.

### 2.2.1 Numerical and Experimental Study of Vertical Axis Wind Turbines

The VAWTs experience the variation of angle of attacks (AoA) in operation because of their structure features, leading to unstable aerodynamic performance, which are different from HAWTs. Figure 2.17 shows the AoA variation in terms of the phase position in one rotation cycle at different TSRs. The static stall angle is labeled in the plot. As we can see in the figure, for a lower TSR, a larger portion of the incidence angles in one revolution exceed the static stall condition [116].

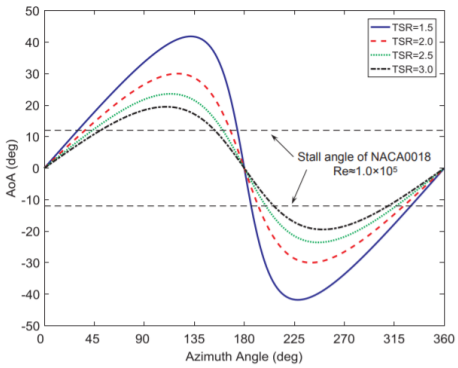


Fig. 2.17 The AoA versus azimuth angles of the turbine blade[116].

The development of dynamic stall of a VAWT was analyzed via experiment by Ferreira et al.[26]. The revolution of the flow field around the turbine blade was visualized by PIV. The process of leading-edge separation and trailing-edge vortex shedding were detected. The velocity and vorticity distribution of both random flow field and phase averaged flow field were analyzed quantitatively by the authors. In addition, the effect of Reynolds number

on the dynamic stall was discussed. Figure 2.18(a) presents the development of clockwise leading edge vortex on the suction side of the aerofoil at six azimuth angles ranging from 72° to 223°, corresponding to high AoAs. The discontinued change of the magnitude of leading edge vortex was analyzed. Figure 2.18(b) shows the counter-clockwise vortex shedding for the trailing edge after rolling up at $\lambda = 2$.

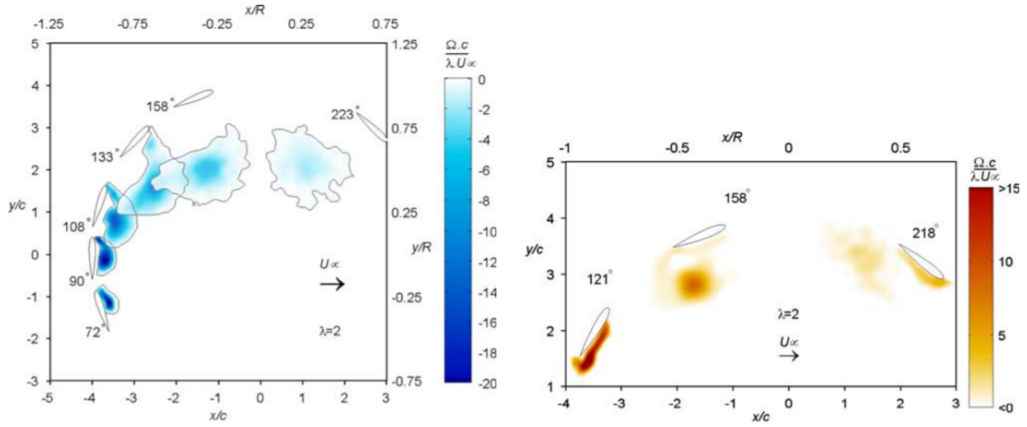


Fig. 2.18 (a)The revolution of vorticity of leading-edge vortex. (b) The display of trailing-edge vortex shedding $\lambda = 2$[26].

A combined experimental and computational study of the three-blade and two-blade small scale VAWTs was presented by Howell et al. [51]. The effect of free stream velocity (Reynolds number), turbine solidity, tip speed ratio and the condition of turbine blade surface on the aerodynamics and performance of the VAWT were investigated by wind tunnel test. It was found that at lower TSRs, the power coefficient of the turbine increased with TSR and then went down after reaching the peak value. In addition, the effect of blade surface roughness on the performance of turbine depended on the wind velocity. In this work, if the wind velocity was lower than 5 m/s, removing the surface roughness could degrade the performance of the wind turbine. On the contrary, if the wind velocity was higher than this value, the VAWT with smooth blade surface performed better. It was verified that the computational results of 3D model match well with the measured data, while the power coefficient obtained from 2D model was much higher than the experimental result, due to the presence of over tip vortices in the 3D simulation and experiment.

Furthermore, the computational study on the development of dynamic stall of VAWTs was conducted by Hamada et al. [40]. A rooftop size H-type wind turbine based on NACA 0022 aerofoil was chosen. They found the behavior of dynamic stall of VAWT was quite different with that in a pitching aerofoil because of the complex change in direction and magnitude of incoming wind velocity. The dynamic stall characteristics of the turbine blades

were quantitatively investigated as shown in Figure 2.19. The instantaneous and adjusted lift coefficient could be present as the function of the angle of attack. The instantaneous lift was base on the instantaneous relative velocity. It can be seen in Figure 2.19 (a), stall occurred at $\theta = 79.2°$, where the lift reached the negative peak value. In Figure 2.19 (b) the adjusted lift was calculated using the mean value of the relative velocity, which shows the variation of lift in one revolution. The lift on the downstream half cycle is much lower than that in the upstream half cycle, leading to low power output.

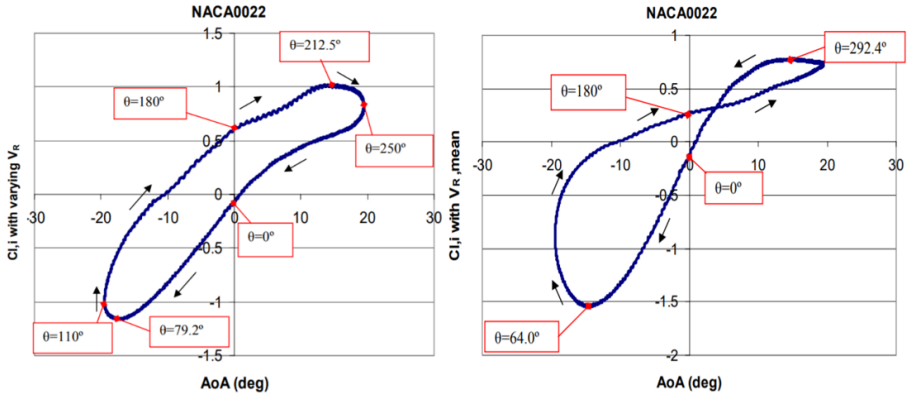


Fig. 2.19 Variation of instantaneous lift coefficient(left) and adjusted lift coefficient(right) with angle of attack[40].

### 2.2.2 Flow Control Methods on the Vertical Axis Wind Turbines

The main goal of flow control for wind turbines is delaying dynamic stall of the blade profiles and reducing the noise level, in order to improve the performance and efficiency of turbines. The passive and active flow control methods usually involve blade modification, trailing edge flap, vortex generator, plasma actuator et al.

The trailing edge flap was applied to helicopters for vibration reduction in early time [121]. Much research has been conducted on flapped aerofoils of various styles and parameters applied on wind turbine blades. An H-type Darrieus wind turbine based on NACA 0012 aerofoil with a trailing edge flap was designed by Yang et al [121]. The schematic view of the flapped aerofoil is shown in Figure 2.20. The aerofoil chord changed by altering the flap angle. As a result, the AoA changed by $\Delta\alpha$. As discussed in the previous section, the AoA of turbine blades exceed the static stall angle for a large portion of the azimuth angles in one cycle, pointing to deep dynamic stall. In this study, the flap control strategy was defined to limit the AoA within a safe range [121]. The flow field around the rotating blades was

examined and it was found that the flow separation was suppressed and the vortices with large intensity were reduced significantly.

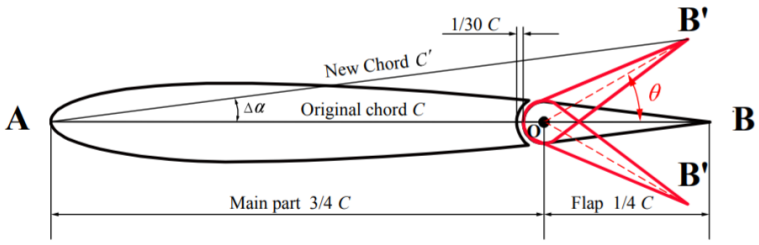


Fig. 2.20 Schematic view of the flapped aerofoil [121].

Wang and Zhuang [116] investigated the mechanism of dynamic stall of the H-type Darrieus turbine and applied blade leading-edge serration to improve its aerodynamic performance using numerical method. It was found that in one revolution, the main difference between turbines with and without modification in terms of torque generation occurred at the azimuth angles ranging from 75° to 160°. The improved case had a higher torque coefficient within this range of AoAs, in which the blade experienced flow separation and dynamic stall as discussed in the previous section. The authors presented the vortice distribution near leading edge of the blades as Figure 2.21. Several counter-rotating vortex pairs could be observed on the modified blade on its suction side and the flow separation was suppressed. Therefore, it is reasonable to note that the improved model has relatively higher power coefficient at low TSRs from 1 to 3. Because the turbine blades experienced the post stall incidence angles for a longer time in one revolution as compare to that at high TSRs.

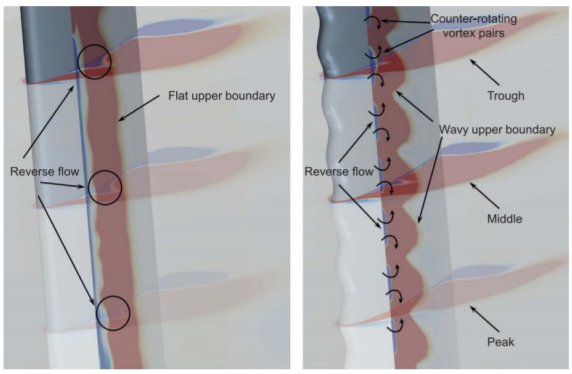


Fig. 2.21 Comparison between modified and original turbine blades in terms of instantaneous vorticity distributions near the leading edge of the blade section [116].

Synthetic jet is another type of modern active flow control device for turbomachinery and wind turbines. A 2D computational study of straight blade Darrieus turbines equipped with synthetic jets were conducted by Velasco et al.[113]. The synthetic located that on upper and lower surface of blades were investigated. Torque coefficient for one revolution of modified turbines were compared with the clean turbine as shown in Figure 2.22. It was clear to find that the synthetic jet on the lower surface of the blade could increase the torque coefficient in the upstream half cycle at the azimuth angle ranging from 90° to 180° but had nearly no effect on the downstream half cycle. On the contrary, the synthetic jet on the upper surface of the blade had positive on the torque output for the downstream half cycle. In addition, the control system with synthetic jets on both upper and lower surface achieved a better flow control in both upstream and downstream regions [113]. The comparison of vorticity field between improved model and unmodified model were presented by the authors. It was found that the strength and size of vortices were degraded with synthetic jets, indicating the suppression of flow separation and dynamic stall. Similar effect of synthetic jets was obtained by Zhu et al.[129] by numerical simulation. The control strategy of synthetic jet actuator was optimized by the authors. The results indicate that a reasonable synthetic jet control strategy can decrease the energy assumption of itself and at the same time increase the power generation of the wind turbine.

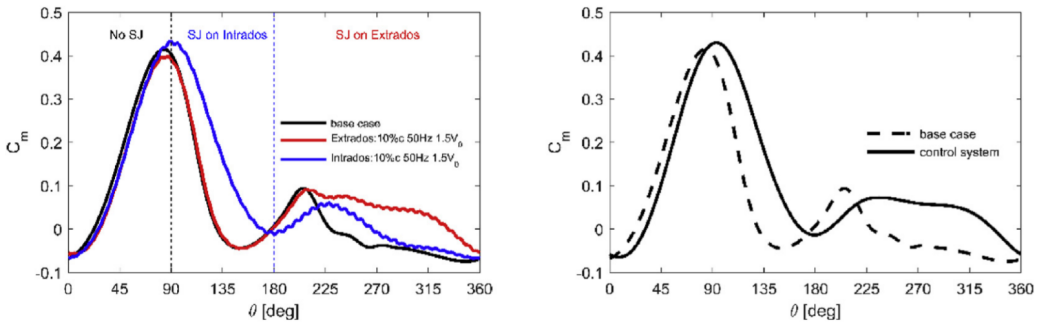


Fig. 2.22 Comparison between modified and original turbine blades in terms of torque coefficient [113].

Sasson and Greenblatt [97] performed an analysis of a novel design called leading-edge slot blowing on an H-type Darrieus turbine. The locations and parameters of the single leading-edge slot are shown in Figure 2.23. The high pressure air was introduced into the blade and directed into the slot. Then the air of high momentum is ejected to the boundary layer to make the flow in the boundary layer turbulent in order to delay the flow separation. It should be noticeable that the suction and pressure surfaces of blades change with each other from the upstream side to the downstream side of one revolution and the leading-edge

slot blowing is only effective in the upstream half cycle. In order to control the dynamic stall over the other half cycle, a configuration of double-slot, one on each side, was considered by the authors. The fluidic oscillatory valves were adopted to control the direction of the high-pressure air. It could be concluded that the leading-edge slot blowing is a effectively way to improve the dynamic performance of VAWTs.

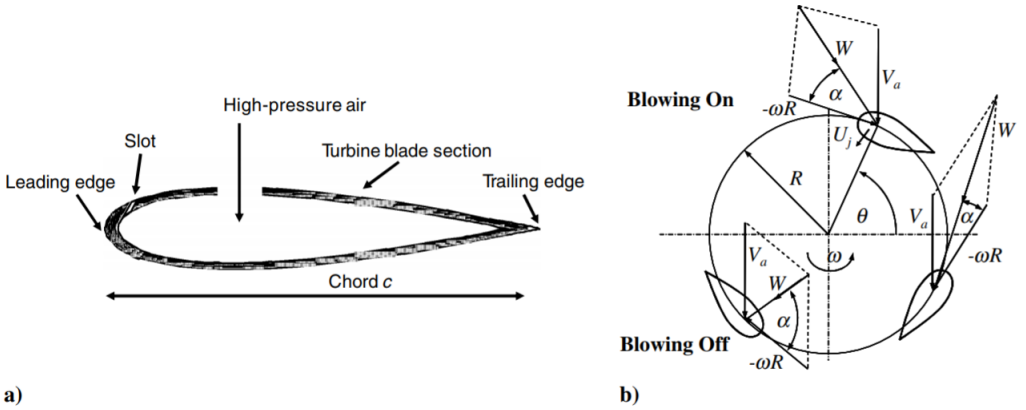


Fig. 2.23 (a)Schematic view of blade section with leading-edge slot. (b) The top view of the turbine [97].

Greenblatt et al. [34] conducted a wind tunnel test of a two-bladed H-type wind turbine equipped with leading-edge DBD plasma actuators to investigate their effect of dynamic stall control. The schematic view of the structure is shown in Figure 2.24. The mechanism of plasma actuators were discussed in the previous chapter in detail. The turbine power was detected by means of PIV measurement [34]. The results indicate that the vortex shedding near the blades was weakened and the flow separation was suppressed with plasma actuators significantly. However, as a active technique, extra power was needed to drive the plasma actuators. Therefore, an adjusting control device was required to deactivate the plasma actuator if not needed.

## 2.3 Summary

This chapter summarizes the previous research about the aerodynamic analysis for aerofoils and VAWTs, especially focusing on the flow control methods for the improvement of their performance and efficiency. A review of numerical methods on solving these unsteady flows is also provided. The difficulty points in research and some of the questions that have not been answered are also point out.

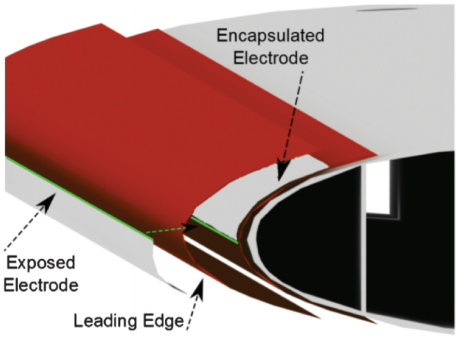


Fig. 2.24 Schematic view of leading-edge DBD plasma actuators [34].

# Chapter 3

# Numerical Methods

## 3.1 Introduction

The numerical methods that carried out in this study were ANSYS Fluent and Code_Saturne. ANSYS Fluent is a commercial CFD software, which is widely-used for industry applications including flow, turbulence and heat transfer modeling. It contains a list of models and offers many types of fluid from their database that users can chose for a wide variety of numerical problems. Fluent uses unstructured mesh based on finite volume method to solve Navier-Stokes equations and provides various choices for spatial and temporal discretization. Detailed descriptions of ANSYS Fluent can be found in Fluent Users Guide [36].

Code_Saturne is an open-source Computational Fluid Dynamics (CFD) software package developed by Électricité de France (EDF) R&D since 1997 [98]. Similar to Fluent, it solves the Navier-Stokes equations by finite volume method and cell-centered approach for the computation of compressible and incompressible flow applications with and without heat transfer. It accepts three-dimensional meshes built with any type of cell grid structure [31]. Several turbulence models are available, from Reynolds-Averaged models ($k-\omega$ SST, $k-\varepsilon$, Apalart Allmaras et al.) to Large-Eddy Simulation models. The It is validated in numerous RANS and LES applications. Version 5.2.0 of incompressible flow module was used for this study.

Code_Saturne has been developed to run on HPCs like Archer and it is opensource, whereas the Fluent licenses are only available on the university cluster which is not design for running large cases. Therefore, to minimize the computational cost, Fluent version 18.2 is used as URANS solver for small cases like the isolated aerofoil, and Code_Saturne is deployed for computational demanding ILES simulations like the VAWT case in present study.

In the following sections, the generalized theory, choice of turbulence model, detailed numerical setup and boundary conditions for both Code_Saturne and the ANSYS Fluent will be discussed.

## 3.2 Governing Equations

The CFD is carried out by solving Navier-Stokes equations that consists of several governing equations. The N-S equations describe a fluid based on the principles of conservation of mass, momentum, and energy.

$$\frac{\partial \rho}{\partial t} + \frac{\partial \rho u_i}{\partial x_i} = 0 \tag{3.1}$$

$$\frac{\partial (\rho u_i)}{\partial t} + \frac{\partial (\rho u_i u_j)}{\partial x_j} = -\frac{\partial p}{\partial x_i} + \frac{\partial T_{ij}}{\partial x_j} + \rho g_i \tag{3.2}$$

The continuity and momentum equations are listed above. $T_{ij}$ is the stress tensor, which is the combination of normal stress tensor and viscous stress tensor. For the Newtonian fluid, in which the viscous stresses are linearly proportional to the local strain rate, the stress tensor can be expressed as follows,

$$T_{ij} = \mu(\tau_{ij}^s - \frac{2}{3}\mu\delta_{ij}\frac{\partial u_j}{\partial x_j}) \tag{3.3}$$

where $\mu$ is the dynamic viscosity. At Mach numbers of less than 0.3, the flow is incompressible. The dynamic viscosity and $\rho$ can be consumed as constant ($D\rho/Dt$=0) and the gravity of air can be ignored. So the governing equations could be simplified to its incompressible form as follows,

$$\frac{\partial u_i}{\partial x_i} = 0 \tag{3.4}$$

$$\rho\frac{\partial (u_i)}{\partial t} + \rho\frac{\rho u_i u_j}{\partial x_j} = -\frac{\partial p}{\partial x_i} + \frac{\partial T_{ij}}{\partial x_j} \tag{3.5}$$

The non-linear partial differential equations contain one continuity equation and three momentum equations. Since the Navier-Stokes equations is the function of pressure and velocity, the equations is closed. However, the Navier-Stokes equations is difficult to solve because of its non-linear characteristics. Therefore, the numerical approach is necessary instead of a general solution.

## 3.3 Turbulence Modeling

Turbulent flows are commonplace in most real life fluid. Although endless effort has been contributed by researchers for decades, there is no analytical theory to understand and predict the origination and evolution of these turbulent flows [107]. As the result, the key factor of solving the Navier-Stokes equations is the turbulence. There are three basic methods for turbulent flow simulation. The first one is to solve the N-S equations directly, which is called as Direct Numerical Simulation (DNS). In this approach, the whole range of spatial and temporal scales of the turbulence is resolved in the computational mesh. However, the strict requirement of mesh resolution and high demand of computational cost of DNS prohibits its widely application in practical engineering with complex flow configurations. To overcome the high requirement of LES, the small-scale structures, which are most computationally expensive to resolve of the flow structure are ignored while modeling and only the large eddies are resolved in the numerical solution. This approach is called as Large-Eddy Simulation (LES). It can extracted the majority of flow structure features and offers relatively low computational cost as compared to DNS. However, LES still require fine resolved mesh and high order schemes [45]. Further reduction of computational cost can be achieved by the Reynolds-Averaged Navier-Stokes (RANS) equations that provide approximate time-averaged solutions to the N-S equations. The RANS equations are primarily used to model turbulent flows.

In this study, the LES and RANS simulation were adopted for the low-Reynolds number applications. The DNS method will not be used for the consideration of its high computational cost.

### 3.3.1 Reynolds Averaged Navier-Stokes Equations

The instantaneous quantities of turbulent flow can be characterized as the combination of its mean and fluctuating components theoretically, which is the idea behind Reynolds Averaged Navier-Stokes (RANS) Equation. The mean value is averaged over an infinite large time step. Take velocity for example,

$$u_i = \overline{u_i} + u_i' \tag{3.6}$$

$$\overline{u_i} = \lim_{t\to\infty} \frac{1}{t} \int_0^t u(x,t)dt \tag{3.7}$$

Reynolds Averaged Navier-Stokes Equations for incompressible flow could be expressed as:

$$\frac{\partial \overline{u_i}}{\partial x_i} = 0 \tag{3.8}$$

$$\rho \frac{\partial \overline{u_i}}{\partial t} + \rho \overline{u_i} \frac{\overline{u_i}}{\partial x_j} = -\frac{\partial p}{\partial x_i} + \frac{\partial}{\partial x_j}(2\mu S_{ji} - \rho \overline{u'_j u'_i}) \tag{3.9}$$

### 3.3.2 Turbulence model

In the momentum equation, the nonlinear, fluctuating term $-\rho \overline{u'_j u'_i}$ in unknown, which makes the N-S equations unclosed. This term is known as Reynolds stress $R_{ij}$. The key problem for RANS modeling is resolving the Reynolds stress by modeling it as a function of the mean flow.

The first order closure model is known as eddy viscosity model and can be expressed as,

$$-\rho u'_j u'_i = \mu_t \left(\frac{\partial u_i}{\partial x_j} + \frac{\partial u_j}{\partial x_i} + \frac{2}{3}\frac{\partial u_k}{\partial x_k}\delta_{ij}\right) - \frac{2}{3}\rho k \delta_{ij} \tag{3.10}$$

This model is based on Boussinesq hypothesis that eddy viscosity is related to turbulence modeling. This closure model works well for some free shear flows such as axisymmetric jets and 2-D jets.

Based on the idea of eddy viscosity model, the turbulence models can be further divided into three categories. The first and simplest one is known as zero-equation model or Algebraic model that do not require any additional equations. This model is usually applied to simpler flow geometries, although it may not be able to predict the turbulent flow precisely in general situation. Another type of turbulence model is called as one-equation model that introduce a transport equation for turbulent kinetic energy k. Spalart-Allmaras model is a one of the typical one-equation model, in which the turbulent eddy viscosity is given by $\mu_t = \tilde{\mu} f_{\mu 1}$. Two-eqution model models the eddy viscosity by solving two additional transport equations for both k and its rate of dissipation. $k-\varepsilon$ and $k-\omega$ models are two common two-equation models that applied for most types of engineering problems.

The ANSYS Fluent and Code_Saturne have all the popular turbulence model choice including Spalart-Allmaras, $k-\varepsilon$ and $k-\omega$ SST models.The $k-\omega$ SST model were adopted in this computational study and it will be discussed in detail in the following section.

### $k-\omega$ SST model

$k-\omega$ model is one of the popular two-equation turbulence models introduced by Wilcox in 1988 [117]. This model attempts to solve two transport equations for the turbulence kinetic energy (k) and the specific dissipation rate ($\omega$). The eddy viscosity is given by $\mu_t = \frac{k}{\omega}$.

The original $k-\omega$ model is effective for wall-bounded cases, particularly for adverse pressure gradient. However, the standard $k-\omega$ model is sensitive to free stream conditions. It was further improved by Menter in 1993 [80]. He combined the $k-\omega$ model with $k-\varepsilon$ model to overcome the weakness of the original $k-\omega$ model. For the inner flow the basic $k-\omega$ model is used, while in the outer region of the boundary layer and mixed regions $k-\varepsilon$ model is adopted. It has been proved that $k-\omega$ SST model is less sensitive to the free stream conditions in comparison with many other turbulence models. The modified model is called as $k-\omega$ SST model. k and $\omega$ are modeled as:

$$\frac{\partial k}{\partial t} + \frac{\partial}{\partial x_i}(\rho k u_i) = P_k - \beta^\star k\omega + \frac{\partial}{\partial x_j}((\mu + \sigma_k \mu_t)\frac{\partial k}{\partial x_j}) \tag{3.11}$$

$$\frac{\partial \omega}{\partial t} + \frac{\partial}{\partial x_i}(\rho \omega u_i) = \frac{\gamma}{\mu_t} P_\omega + \beta \omega^2 + \frac{\partial}{\partial x_j}((\mu + \sigma_k \mu_t)\frac{\partial \omega}{\partial x_j}) + 2(1-F_1)\sigma_{\omega 2}\frac{1}{\omega}\frac{\partial k}{\partial x_i}\frac{\partial \omega}{\partial x_i} \tag{3.12}$$

The terms of $P_k$ and $P_\omega$ can be approximated as:

$$P_\omega = \mu_t S^2/\rho - \frac{2}{3}k\frac{u_i}{x_i} \tag{3.13}$$

$$P_k = min(P_\omega, c_1 c_\mu \omega k) \tag{3.14}$$

The blending function $F_1$ is defined as:

$$F_1 = tanh((min[max(\frac{\sqrt{k}}{\beta^\star \omega y}, \frac{500\mu}{y^2\omega}), \frac{4\sigma\omega 2k}{CD_{k\omega}y^2}])^4) \tag{3.15}$$

$$CD_{k\omega} = max(2\rho\sigma_{\omega 2}\frac{1}{\omega}\frac{\partial k}{x_i}\frac{\partial \omega}{x_i}, 10^{-10}) \tag{3.16}$$

The blending function $F_2$ is defined as:

$$F_2 = tanh((max(\frac{2\sqrt{k}}{\beta^\star \omega y}, \frac{500\mu}{y^2\omega}))^2) \tag{3.17}$$

The eddy viscosity $\mu_t$ can be expressed as :

$$\mu_t = \frac{a_1 k}{max(a_1 \omega, SF_2)} \tag{3.18}$$

One of the challenge of tested cases is to accurately predict the stalled flow of wind turbine rotor. $k-\omega$ SST turbulence model have shown good performance for the flow characteristics prediction for flow separation. The extensive literature on the usage of $k-\omega$ SST turbulence model can be very useful to validate its effectiveness on the wind turbine simulation. Three sets of validation studies including smooth cylinder, a rough cylinder and a VAWT are performed by Rezaeiha et al.[91]. Roshan et al.[94] conducted the numerical study about a dusted wind turbine using the similar simulation procedure and found there is a good agreement between the results of the numerical simulations and manufacturer's experimental data [94]. In the present study $k-\omega$ SST model was used in RANS simulation for both isolated aerofoil and the VAWT. The CFD results of the aerofoil and VAWT have been extensively validated against experimental data in detail in chapter 4 and chapter 5.

### 3.3.3 Large Eddy Simulation

The principal idea behind LES is to simulate the large-scale length scales, while ignore the smallest eddies that are the most computationally expensive to resolve, via low-pass filtering of N-S equations. A spatial filtering operation can be performed by an LES filter. The filtered field $\tilde{\phi}$ can be defined as:

$$\tilde{\phi} = \int G(x,x')\phi(x')dx' \tag{3.19}$$

where G is the filter convolution kernel that associated with a length scale $\tilde{\Delta}$. Any eddies smaller than this length scale are not resolved, but modeled. Using the above filter definition, any variable can be split up into a filted and unresolved portion, as

$$\phi = \tilde{\phi} + \phi' \tag{3.20}$$

Similarly, performing this filter to the incompressible Navier-Stokes equations can be expressed as,

$$\frac{\partial \tilde{u}_i}{\partial x_i} = 0 \tag{3.21}$$

$$\frac{\partial \tilde{u}_i}{\partial t} + \frac{\partial}{\partial x_j}(\tilde{u}_i \tilde{u}_j) = -\frac{1}{\rho}\frac{\partial \tilde{p}}{\partial x_i} + 2\mu \frac{\partial}{\partial x_j}\tilde{S_{ij}} - \frac{\partial \tau^{\star}_{ij}}{\partial x_j} \tag{3.22}$$

Unclosed term $\tau_{ij}^{\star}$ is called as subgrid stress tensor or residual stress tensor, is introduced in the filtered N-S equations and it need to be modeled, which is known as sub-grid scale model. The subgrid stress tensor can be approximated by Boussinesq hypothesis.

$$\tau_{ij}^{\star} = 2\mu_t \tilde{S_{ij}} + \frac{1}{3}\tau_{kk}\delta_{ij} \tag{3.23}$$

where $S_{ij}$is the rate-of-strain tensor. The eddy viscosity $\mu_t$ can be calculated by several sub-grid scale models. The first one is called as Smagorinsky–Lilly SGS model, which is developed by Smagorinsky. It modeled $\mu_t$ as,

$$\mu_t = (C_s\Delta_g)^2\sqrt{2\tilde{S_{ij}}\tilde{S_{ij}}} = (C_s\Delta_g)^2|S| \tag{3.24}$$

where $\Delta_g$ is the filter width (grid size) and $C_s$ is constant. The main weakness of Smagorinsky–Lilly SGS model is that $C_s$ can not be adjusted to a validated value of the cases of complex flow. Germano dynamic model was proposed to formulate a more universal method to SGS models. It uses a test filter with twice the width of the original filter to be performed to N-S equations. The difference between the two filtered field is assessed and $C_s$ is defined by the a minimum least-square error method.

$$C_S^2 = \frac{\langle L_{ij}M_{ij}\rangle}{\langle M_{ij}M_{ij}\rangle} \tag{3.25}$$

Germano dynamic model is more stable and adaptive for more widely applications, but is more computationally expensive as compared to Smagorinsky-Lilly model.

An unconventional large eddy simulation called as Numerical or implicit LES is developed by Boris in 1959 [11]. The main difference between numerical LES and normal LES is that in the former approach no subgrid scale models are used, and the effects of small eddies are incorporated in the dissipation of a class of high-order non-oscillatory finite-volume numerical schemes [24]. The numerical LES is an advanced approach with less computational cost needed. Moreover, the modeling errors from explicit Subgrid-Scale modeling can be eliminated. It has been found that the contribution of SGS terms dominates only with eighth order schemes or for second order schemes with high ratio of filter size and grid size. Since in this study, a second order finite volume method is adopted, the numerical LES with no SGS models is performed.

## 3.4 Moving Reference Frame

In real life many engineering problems involve rotational flow domains, such as wind turbine and centrifugal compressor. It is advantageous to use the moving reference frame with a rotating angular velocity $\vec{\omega}$ instead of normal inertial reference frame to solve such problems.

The velocity from the moving reference frame can be related to the inertial frame as following equation,

$$\vec{u} = \vec{u_r} + \vec{\omega} \times \vec{r} \tag{3.26}$$

where $\vec{u_r}$ is the relative velocity. The Navier-Stokes equations can be reformulated using the relative velocities as dependent variables as follows:

$$\frac{\partial \rho}{\partial t} + \nabla \cdot \rho \vec{u_r} = 0 \tag{3.27}$$

$$\frac{\partial}{\partial t}(\rho \vec{u_r}) + \nabla \cdot (\rho \vec{u_r} \vec{u_r}) + \rho(2\vec{\omega} \times \vec{u_r} + \vec{\omega} \times \vec{\omega} \times \vec{u_r}) = -\nabla p + \nabla \cdot \bar{\bar{\tau}}_r + \vec{F} \tag{3.28}$$

Two addition terms are introduced in the momentum equation: a Coriolis acceleration term ($2\vec{\omega} \times \vec{u_r}$) and a centripetal acceleration term ($\vec{\omega} \times \vec{\omega} \times \vec{u_r}$).

The Navier-stokes equations can be also formulated using the absolute velocities as dependent variables, which is known as absolute velocity formulation. The N-S equations can be written as follows:

$$\frac{\partial \rho}{\partial t} + \nabla \cdot \rho \vec{u_r} = 0 \tag{3.29}$$

$$\frac{\partial}{\partial t}(\rho \vec{u}) + \nabla \cdot (\rho \vec{u_r} \vec{u}) + \rho(\vec{\omega} \times \vec{u}) = -\nabla p + \nabla \cdot \bar{\bar{\tau}} + \vec{F} \tag{3.30}$$

## 3.5 Sliding Mesh

In order to model the rotation of turbine rotor, the relative motion is necessary between computational domains. The modeling interface between two meshes of different motion can be achieved by two numerical methods known as overset (chimera) mesh and dynamic mesh. The overset mesh means that the two adjacent domains have overlapping mesh. The dynamic mesh is composed of several meshes with relative motion and share the same interface

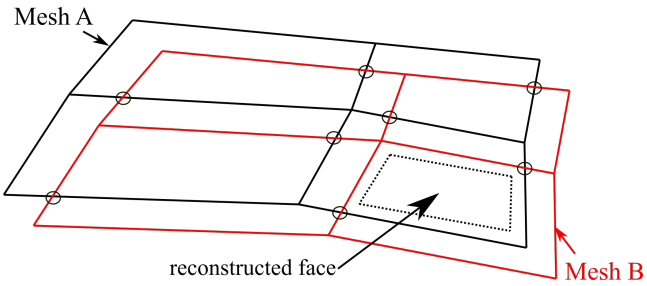


Fig. 3.1 Mesh joining.

between them. The sliding mesh is one type of dynamic mesh, in which this interface is rigid and keep a same shape while moving. Both methods give the similar result for the wind turbine modeling in terms of accuracy, the sliding mesh is selected in both ANSYS Fluent and Code_Saturne.

The computational method is required to achieve the information transportation through the interface between the two domains. ANSYS Fluent and Code_Saturne have the similar sliding mesh algorithm. The schematic view of mesh joining in the process of sliding mesh is shown in Figure 3.1. Two computational domain Mesh A and Mesh B are labeled in the figure. At the end of a certain time step, the dashed line represents the reconstructed face, which is regarded as the internal face for the solution for the governing equation. In the next time iteration, the joined mesh is broken, move and join again. A new reconstructed face is formed.

Figure 3.2 shows the topology structure of 2D computational domain for the VAWT, which consists of two parts, ROTOR and STATOR. The ROTOR is a circular zone as a rotating part in the domain and the STATOR is stationary. The sliding mesh interface is also labeled in the figure as INTERFACE that allows the grids in ROTOR to slide relative to STATOR zone.

## 3.6 Summary

This chapter described the numerical methods that are implemented in ANSYS Fluent and Code_Saturne in this study. The generalized theory, choice of turbulence model and detailed numerical setup are then introduced. At the end, the sliding mesh approach is described in this chapter.

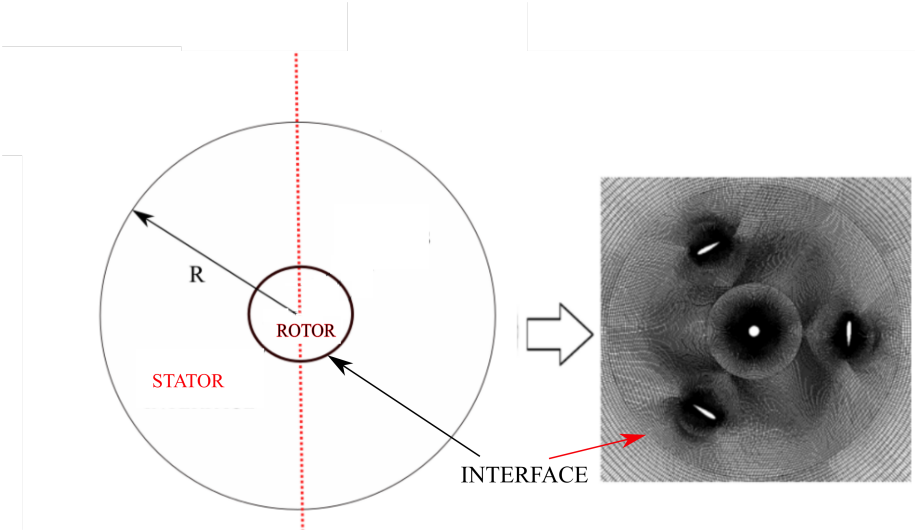


Fig. 3.2 Mesh joining in VAWT modeling.

# Chapter 4

# CFD Analysis for the Performance of Gurney Flap on Aerofoil and Vertical Axis Turbine

The Gurney flap (GF) is a widely used flow control device for various aerodynamic applications. Numerical study was conducted in this chapter aiming to investigate the mechanism and aerodynamic effect of GFs on a two dimensional isolated stationary aerofoil and a H-type vertical axis wind turbine. In addition, the optimal variables of the Gurney flap including height and mounting angle are determined in this study.

## 4.1 CFD Domain Characteristics

Generating the right computational domain for a fluid dynamics problem is one of the crucial tasks in the modeling process. Some necessary requirements need to be taken into account. The domain should be large enough to capture the whole flow phenomenon. The cells number of the grid with a suitable mesh quality and the first cell height near the wall boundary need to be carefully chosen. On the other hand, the mesh should not be too large leading to a high computational cost.

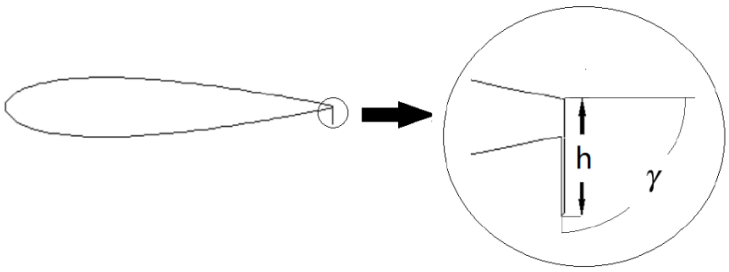


Fig. 4.1 The schematic view of Gurney flap of the NACA 0018 aerofoil.

### 4.1.1 Isolated aerofoil

#### Description of the numerical flow field

In this study, unsteady flow computations were carried out for the NACA0018 aerofoil with a Gurney flap. A number of wind tunnel tests and numerical studies have been conducted on aerofoils with Gurney flaps of different sizes. Figure 4.1 shows the structure of Gurney flap (GF) attached perpendicular to the chord line of the aerofoil. h refers to the height of GF. $\gamma$ is its mounting angle. In most conditions, $\gamma = 90^{\circ}$ is the optimum chosen as the mounting angle. However, in some cases, a different angle may make the GF perform better.

In the simulation of an isolated aerofoil, the chord length is 0.246m. The Reynolds number based on the aerofoil chord length (c) is 160k and the Mach number is 0.03, i.e. the flow is incompressible. Such conditions are appropriate for small wind turbines [82]. GFs of h=1.0%, 2.0%, 3.0%, 4.0% and 5.0% of the chord length were studied. Figure 4.2 portrays the computational domain and main boundary conditions. The inlet has been set as a velocity inlet, with a constant wind velocity profile of 10 m/s, while, the outlet has been set as a pressure outlet with atmospheric pressure value. Symmetry boundary condition was adopted for the stream normal boundaries. No-slip wall boundary condition was implemented on the aerofoil and flap surface..

#### Domain meshing

The C-type structured grid has been chosen for the whole computational domain in order to reduce the computational time and increase the accuracy. Figure 4.3 shows the far-field and zoomed view of the computational mesh. There are 200 points along the surface of aerofoil. In order to capture the physics around the aerofoil, the grids were refined in the area close to the aerofoil profiles especially near the leading edge and trailing edge.

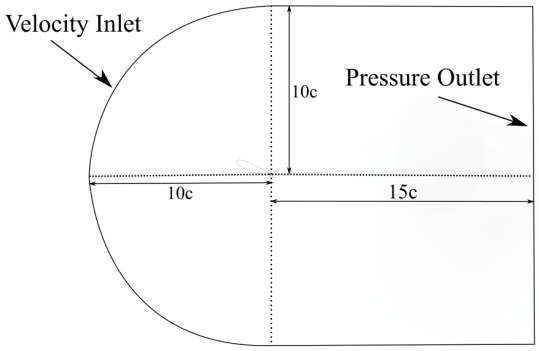


Fig. 4.2 Geometrical features and main dimensions of the computational domain.

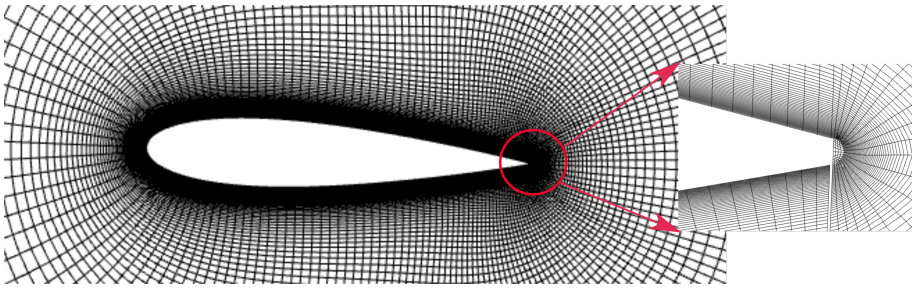

Fig. 4.3 Farfield and zoom view of the computational mesh of the isolated aerofoil NACA 0018.

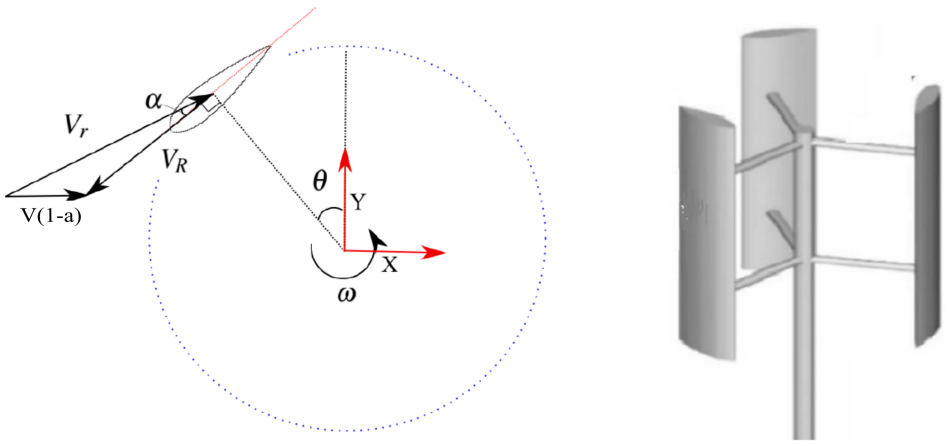


Fig. 4.4 Farfield and zoom view of the computational mesh of the isolated aerofoil NACA 0018.

### 4.1.2 Structure of the VAWT

In the second part of this chapter, a computational study was conducted on a H-type Darrieus wind turbine. The schematic view of the turbine is given in Figure 4.4. This style of wind turbine has a simple configuration, which is consisting of three vertical blades, one vertical support and six horizontal struts.

The rotor rotates in a fixed angular velocity $\omega$. Hence, the blades have a velocity of $R\omega$. The Tip Speed Ratio (TSR) is defined as $\lambda = \frac{R\omega}{V}$(V stands for the wind velocity). Thus the velocity 'seen' by the blade is composed of these two components. Normally the wind turbine is propelled by the force tangential to the struts and the normal force into the struts has no use, except causing structural stresses.

The H-type Darrieus rotor, found in reference [82], was used to develop and validate the 2D CFD model. The rotor features are listed in the table below (Table 1). For this work, a relatively small rotor was chosen. To reduce time and resources needed for numerical simulation, a 2D cross-section of H-type turbine based on the NACA 0018 aerofoil was used, which can give relatively a high lift-to-drag ratio [8]. This kind of rotor gives about 300W per unit length for wind speed of 8 m/s.

During the rotation cycle, the angle of attack AoA ($\alpha$) varies the azimuth angle ($\theta$). The definition of azimuth angle ($\theta$) is shown in the velocity triangle on the blades in Figure 4.4. The induction factor a can be calculated according to the study by Bianchini et al.[10]. However, to simplify the analysis in the current study, a=0 has been adopted. This practice

Table 4.1 Rotor Parameter

| | |
|---|---|
| Number of blades | 3 |
| Blade aerofoil | NACA0018 |
| Blade chord (L) [m] | 0.246 |
| Radius (R) [m] | 0.85 |
| Wind speed ($V_W$) (m/s) | 8 |
| Tip speed ratio ($\lambda$) | 1-3.5 |

can also be found in [81]. Therefore, the angle between the relative velocity and chord line of the aerofoil is defined as theoretical AoA ($\alpha$). For a given tip speed ratio $\lambda$, $\alpha$ is the function of $\theta$ and $\lambda$ as follows,

$$tan\alpha = \frac{(1-a)sin\theta}{\lambda + \cos\theta} \tag{4.1}$$

### 4.1.3 Domain meshing

In the present study, all the simulations are carried out in 2D and effect of supporting arms, central shaft and three dimensionality in the flow are not considered. The geometry of the computational domain and mesh distribution are given in Figure 4.5. To simulate the rotation of the rotor, the computational domain was divided into two sub-domains (rotor and stator) with an interface between them. The interface merged the two separated computation zones into a single and continuous one. The rotor domain is a circular inner zone that includes the actual wind turbine rotor. The rotor and the rotor zone have the same rotational angular velocity. The stator domain is a large stationary circular domain outside the inner zone. The mesh on both sides of the interface have the same cell size to achieve a smooth and sliding transition between the two zones.

The turbine was assumed to operate in an open field. To avoid wall blockage, the computational domain should be large enough. In this research, the radius of the stator domain is 15 times the radius of the turbine ensuring a full development of the wake. The radius of the rotor zone is 1.5 times of the turbine. The inlet boundary was set as a velocity inlet boundary with a constant wind speed of 8 m/s and the outlet was set as pressure outlet with the atmosphere pressure value. The turbine operated with a fixed wind speed and the rotation speed of turbine changed, to achieve different tip speed ratios.

The structured mesh was applied to both rotor and stator zones. Areas around turbine blades were locally refined in order to capture the flow field more accurately. The stator mesh

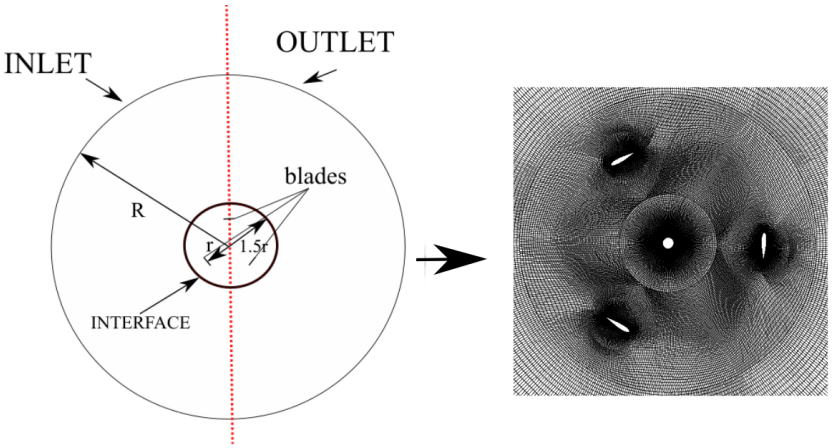


Fig. 4.5 The computational domain and mesh distribution of 2D H-type wind turbine.

is relatively coarsened in order to minimize the CPU time. Sliding mesh technique was used to couple the two computational domains of different rotation speed. The total grid size of the computation domain is about $0.546 \times 10^6$.

## 4.2 Numerical Solution

In this study, ANSYS Fluent was used to generate the 2D CFD model for both the isolated aerofoil and the VAWT. A finite volume method was applied. The solver was set as pressure based in the unsteady RANS version. Spatial and temporal of second order accuracy were used. The Coupled algorithm was used for the time marching and the convergence was monitored per time step.

The two-equations SST (Shear Stress Transport) $k\omega$ turbulence model was chosen as it has shown good performance in turbo-machinery experiencing flow separation as expected for the blades of VAWT during the rotation [80]. The time step was set to guarantee that one revolution was discretized by around 2100 time steps for all the tip speed ratio tested. This results in a smaller time step for a larger tip speed ratio.

The phase average was performed after the periodicity was observed. If the average torque coefficient of turbine in one revolution was less than 0.1% compared to the value of last period, the simulation was considered to be converged. Typically, this happened after around 10 revolutions. Then, the phase averaging of the following 5 revolutions are performed to calculate the final result for a specific azimuth angle.

## 4.3 Flow Control on NACA 0018 Aerofoil

### 4.3.1 Baseline and Mesh Sensitivity

In order to verify the validity of the numerical method, a baseline of the isolated aerofoil NACA 0018 was carried out to establish the sensitivity of the simulation to the mesh revolution. Mesh refining was carefully conducted near the aerofoil wall boundaries with three different height of first grid cells near the wall. The mesh parameters are presented in Table 4.2. The experimental data from the literature of Sheldahl et al. [101] was chosen for comparison.

Table 4.2 Mesh

| | Height of the First Grid Cell | Total Cells | Y Plus |
|---|---|---|---|
| Mesh 1 | $2 \times 10^{-5}$ | $2.87 \times 10^{5}$ | 1 |
| Mesh 2 | $5 \times 10^{-5}$ | $1.76 \times 10^{5}$ | 2.5 |
| Mesh 3 | $2 \times 10^{-4}$ | $0.8 \times 10^{5}$ | 10 |

The coarsest grid yields a deviation of 5.40% compared with experimental result in terms of lift, while the drag difference is as large as 20.8% as shown in Table 4.3. The finest mesh is the optimum with the least deviation for both lift and drag compared with measured data. However, It seems that the medium size ($5 \times 10^{-5}$) for the height of first grid cell near the wall is acceptable with a discrepancy of 2.30% for the lift and 11.1% for the drag. As the result, Mesh 2 was used in the simulation for the consideration of less computational resource and time compared to the finest mesh.

Table 4.3 Comparison of URANS result and measured data in terms of lift and drag

| | Angle of Attack | $C_l$ | $C_d$ |
|---|---|---|---|
| Mesh 1 | 14.00° | 0.945 | 0.067 |
| Mesh 2 | 14.00° | 0.934 | 0.064 |
| Mesh 3 | 14.00° | 0.907 | 0.057 |
| Experiment | 14.00° | 0.956 | 0.072 |

Shown in Figure 4.6 is a comparison of the computed lift and drag to the experimental values for angles of attack (AoA) between 0° to 20° (no Gurney flap simulation)[101]. It can be seen that the value of lift from the computations agree well with the experimental data

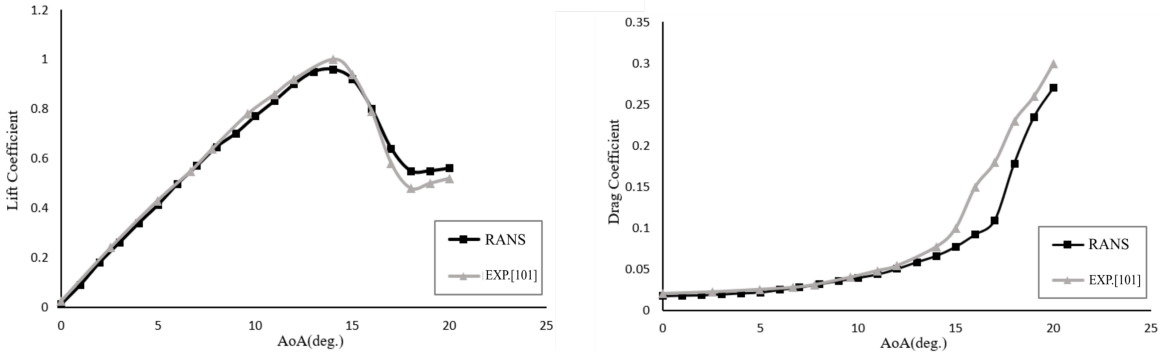


Fig. 4.6 Lift and drag coefficients variations with angle of attack for the clean NACA 0018, $Re_c = 2 \times 10^5$, where c is the chord length.

up to $\alpha = 16^\circ$. There is a very good quantitative agreement between the experimental data and numerical result in terms of drag when $\alpha < 14^\circ$. The experimental results exhibit higher drag values after stall at AoAs ranging from more $14^\circ$ to $20^\circ$, although both the experimental and numerical values show the same qualitative behaviour of rapid drag increase after stall at a similar rate. similar result of RANS modeling could be found in many literatures [9] [125][66]. The application of RANS turbulence model may underestimate the value of drag in numerical method after stall. Another reason could be the presence of a significant amount of 3D flow in the separated regions of the wind tunnel model, which the 2D numerical results obviously cannot resolve [66].

### 4.3.2 Flow Control effect

#### Lift and Drag

The effect of GFs attached to the NACA 0018 aerofoil was investigated in this section. Figures 4.7 and 4.8 show the lift and drag coefficients of aerofoils with and without GFs. The "clean" data is from the aerofoil without GF, whereas the lines denoted as '$GFx\%c$' are the cases where the aerofoils are equipped with GFs. The length of the GF is '$x\%$' of the aerofoil chord length. The time-averaged lift coefficient ($C_L$) increases as the AoA rises. In addition, The $C_L$ increases with an increase in the GF height at the AoA ranging from $0^\circ$ to $17^\circ$ as shown in Figure 4.7. Also, the effect of the GF is to substantially increase the maximum $C_L$. Compared to the clean model , the values of the maximum $C_L$ increased by 16.5%, 28.7%, 39.5%, 48.8% and 67.1% for the GF heights %1c, %2c, %3c, %4c and %5c, respectively. The figure also shows that the stall angle decreases from $14^\circ$ of the clean aerofoil case to $12.5^\circ$ of the case with a 5%c GF. Similar results were reported for NACA 0012 aerofoil by

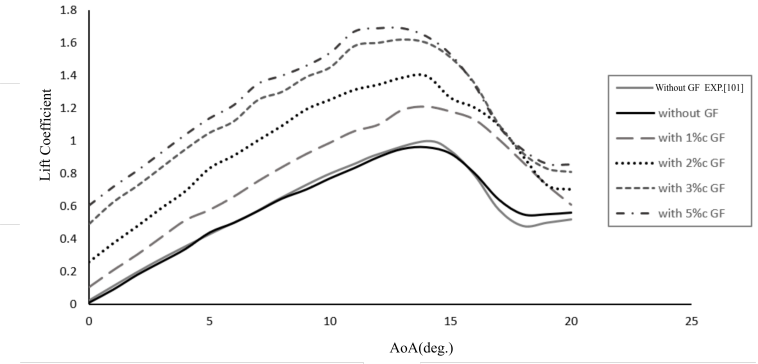


Fig. 4.7 Lift coefficient comparison of the aerofoil.

J.Wang et al.[114], for LA203A aerofoil by Gigukre [33] and for NACA 4412 aerofoil by Storm et al.[108]. They are caused by an earlier burst of leading edge separation bubble [70][102].

Shown in Figure 4.8 are the time-averaged drag coefficient ($C_D$) for the same configurations. Obviously, as the angle of attack increases, the drag coefficient increases as well. At low AoA ranging from 0° to 12°, the aerofoils with 1%c and 2%c GF have a $C_D$ similar with the clean model, which is lower than the value of the aerofoils with 3%c, 4%c and 5%c. So it is clear that the flaps with a height higher than 2%c will significantly increase the drag. There is a large drag penalty associated with the GFs at moderate-to-high AoAs, although the $C_L$ increases as well. Therefore, the effect of GFs on the lift-to-drag ratio is limited. So the optimum height of the GF needs to be investigated. The GF can effectively increase the lift-to-drag ratio, especially for low angles of attack ranging from 0° to 12° as shown in Figure 4.9. However, it is not increase with the enhancement of GF height. The aerofoil with 2%c GF has the largest lift-to-drag ratio as compared to other cases at the AoA ranging from 5° to 12°.

### Pressure Distribution

Figure 4.10 shows the pressure coefficient distribution at AoA of 3°. The pressure coefficient is defined as followed:

$$C_p = \frac{p - p_\infty}{0.5\rho V^2} \tag{4.2}$$

where $p_\infty$, $\rho$ and V is the static pressure, density and velocity of free stream respectively.

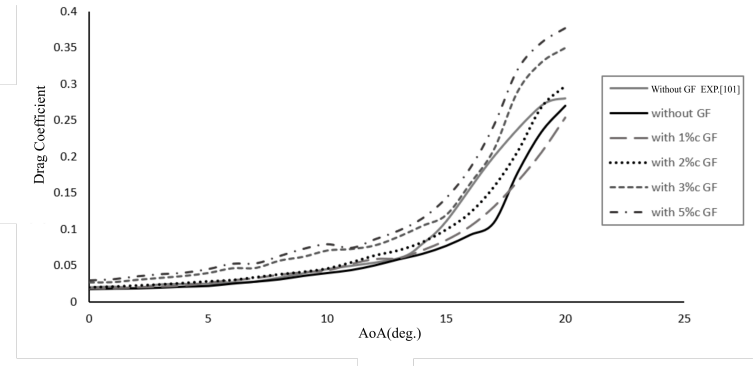


Fig. 4.8 Drag coefficient comparison of the aerofoil.

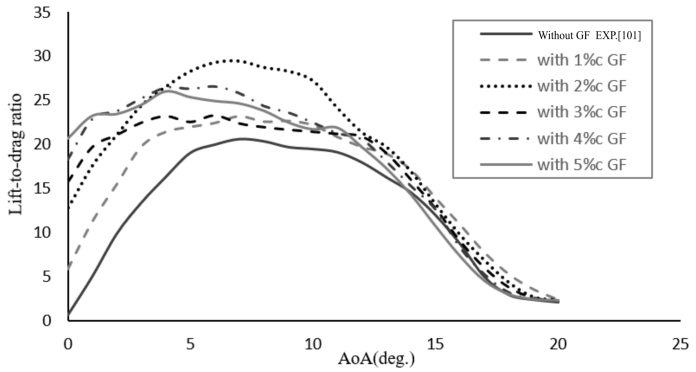


Fig. 4.9 Lift-to-drag ratio comparison of the aerofoil.

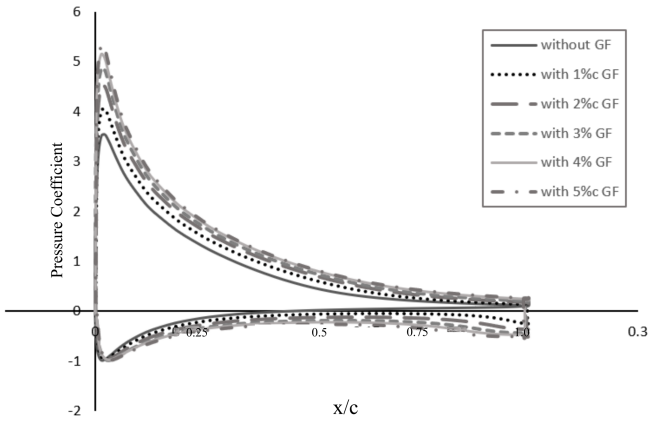


Fig. 4.10 Pressure coefficient on the aerofoil at $\alpha = 13°$.

It can be seen that the GF can effectively increase the loading on the aerofoil. With the increasing height of GF, the pressure difference between the lower and upper surfaces of the aerofoil becomes larger, especially near the trailing edge where the GF is attached. This is consistent with the improvement of the lift coefficient given in Figure 4.7. It should be noted that an adverse pressure gradient occurs near the trailing edge of the aerofoil due to the presence of GFs. A similar result was obtained by Jang et al.[55]. This was also found in previous research by Liebeck who indicated that the existence of a circular vortex that was associated with the adverse pressure gradient before the GF [72].

**Separation Control**

The effect of the GF on the upper surface separation location of the aerofoil is of particular interest. Figure 4.11 gives the movement of the separation point with different GFs. At the separation point, the skin friction coefficient ($C_f$)is nearly zero. The definition of $C_f$ is as follows,

$$C_f = \frac{\Gamma_w}{0.5\rho V^2} \tag{4.3}$$

where $\Gamma$ refers to the wall shear stress. It is clear that the GF changes the flow separation significantly by delaying the onset of separation point.

At AoA of 5°, the 1%c GF moves the separation point downstream by 2% in comparison with the clean aerofoil. This value can reach 5%, if the height of GF increases to 2%c. At $\alpha = 10°$ the effect of GF on the separation point is much stronger. The GF of 2%c moves the separation point downstream by 18% compared to the clean aerofoil case. However, it could

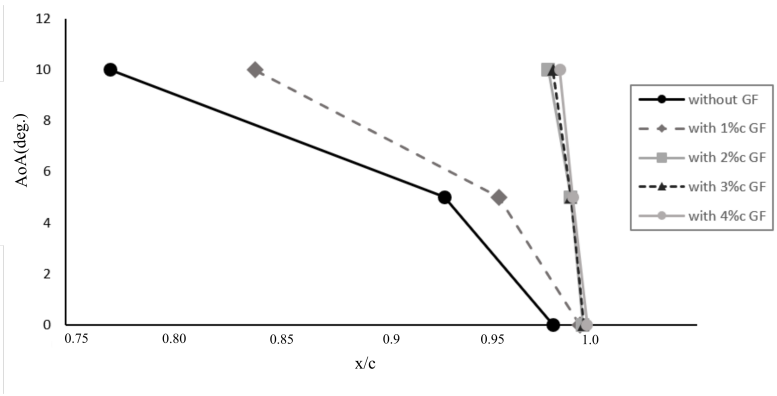


Fig. 4.11 Separation point variation versus angle of attack of different aerofoils.

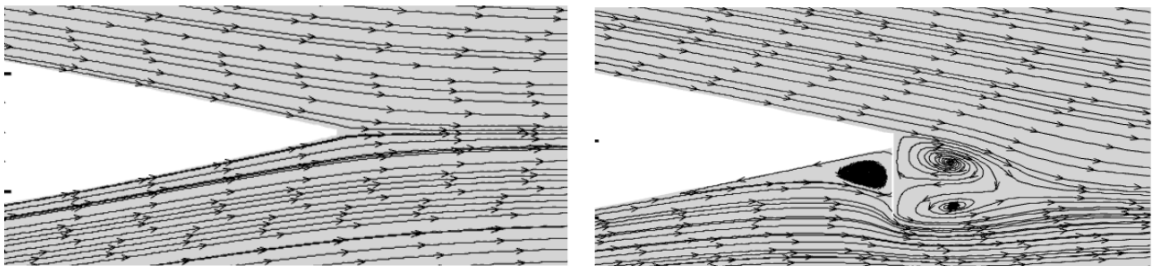

(a) (b)

Fig. 4.12 Flow patterns near the trailing edge of aerofoils at $\alpha$=0° (a) Clean aerofoil (b) 2%c GF.

not further shift the separation point by improving the GF height when the GF is higher than 2%c.

### Trailing Edge Flow Structure

To better understand the influence of GFs on the aerofoil performance, Figures 4.12 to 4.14 compare the streamlines of the flow field with and without GFs. At $\alpha = 0°$ as in Figure 4.12, the streamlines are generally very smooth and there is no separation near the trailing edge of the clean aerofoil. However, when the 2%c GF is attached to the aerofoil, two separation regions form in the trailing edge of the aerofoil with %2c GF, upstream and downstream the GF respectively, which altered the Kutta condition and circulation in the region.

At $\alpha = 9°$, a clean aerofoil suffers an observable separation on its suction side due to the adverse pressure gradient as in Figure 4.13 (a). However, a 2%c GF effectively eliminates such flow separation by pushing the vortices further downstream (Figure 4.13(b)), which

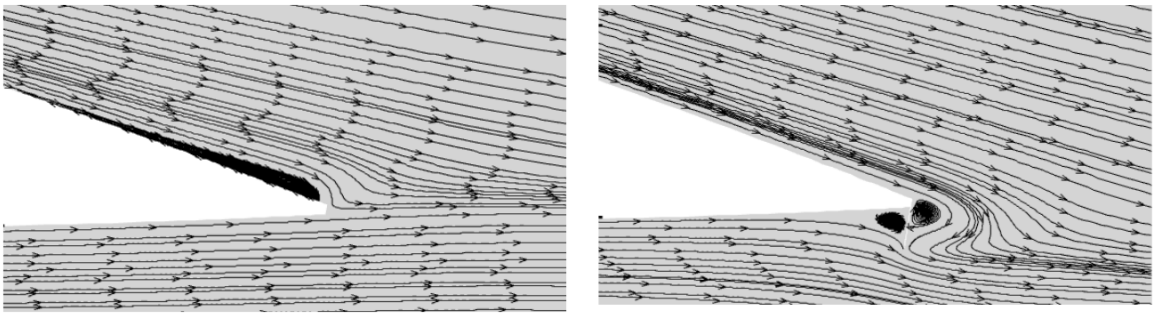

(a) (b)

Fig. 4.13 Flow patterns near the trailing edge of aerofoils at $\alpha$=9° (a) Clean aerofoil (b) 2%c GF.

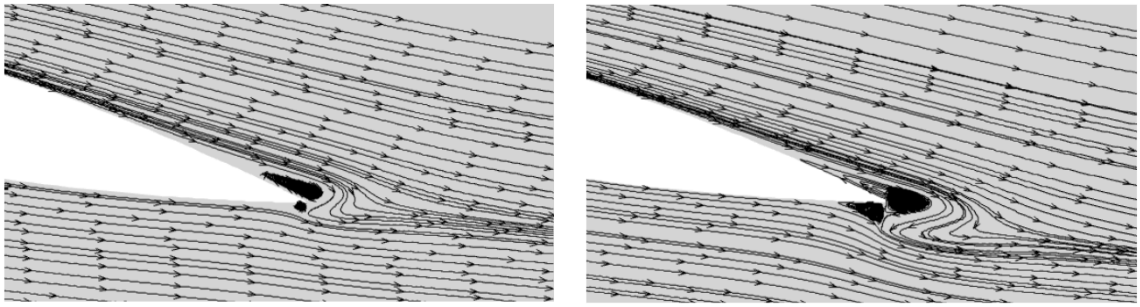

(a) (b)

Fig. 4.14 Flow patterns near the trailing edge of aerofoils at $\alpha$= 13° (a) 2%c GF (b) 5%c GF.

can be regarded as the extension of the effective chord length of the aerofoil, leading to the lift enhancement. A similar result was found by T. Yu [126] and Wang et al. [114]. This phenomenon agrees well with the calculated separation locations given above.

Figure 4.14 illustrates the effect of the height of the GF on the flow separation at high AoA of $\alpha$=13°. The length of the separation bubble on the suction side of the aerofoil marked with 2%GF is larger than that of 5%c GF case and the centre of the vortices moves downstream with the increase of GF's height, which can give an explanation why the lift force increased with the increase of the GF's height.

On the other hand, the working mechanism of the GF lies in its effect on the Kutta condition as well. The presence of the low pressure area behind the GF causes a downward turning of the flow when it leaves the trailing edge of the aerofoil. As a result, the downward momentum of the flow increases. So the flow velocity on the suction side is improved. Correspondingly the pressure decrease, leading to the enhancement in lift. At high AoAs,

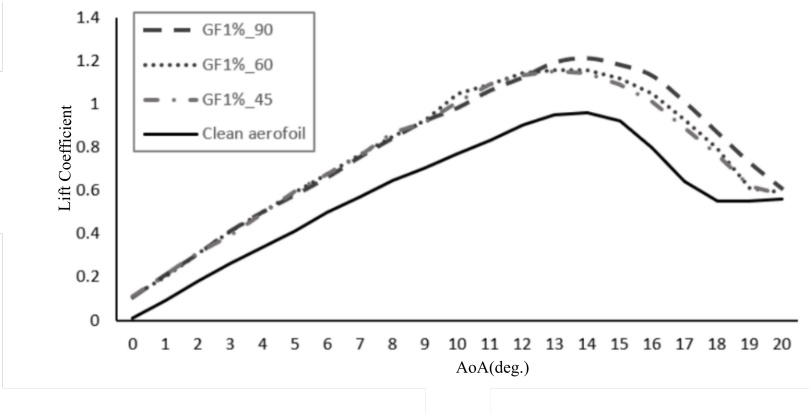


Fig. 4.15 Lift coefficient variation with aerofoil's angle of attack.

the vortices are pushed downstream due to low pressure field behind the GF and the flow separation is suppressed.

### Effects of the GF Mounting Angle

A numerical simulation was also conducted to investigate the effect of the GF's mounting angle $\gamma$ on the aerodynamic performance of the aerofoil. Normally the GF is mounted normal to the chord line, i.e $\gamma = 90^\circ$ In this work the GF with a size of 1% chord length was chosen for discussion. As shown in Figure 4.15, "GF1%$X$" refers to the aerofoil with GF of the mounting angle "X". The variation of $C_L$ versus the AoA is shown in Figure 4.15 for the aerofoils with GFs of various mounting angles: 45°, 60° and 90°. It can be seen that all cases have a similar slope of the lift coefficient curve and the GFs increase the lift coefficient and reduce the stall angle as compared to the clean aerofoil. The flap with the mounting angle of 90° provides better performance for lift enhancement compared to other two mounting angles near the stall condition by around 5%.

On the other hand, Figure 4.16 shows the comparison of the aerofoils of different mounting angles in terms of drag coefficient. It can be seen that the $C_D$ stays almost unchanged at the AoAranging from 0° to 13° and there in no clear discrepancy between the aerofoils with GFs of different mounting angles. However at higher AoA ranging from 14° to 20°, the drag penalty by the GF increases with the improvement of the mounting angle as shown in Figure 4.16.

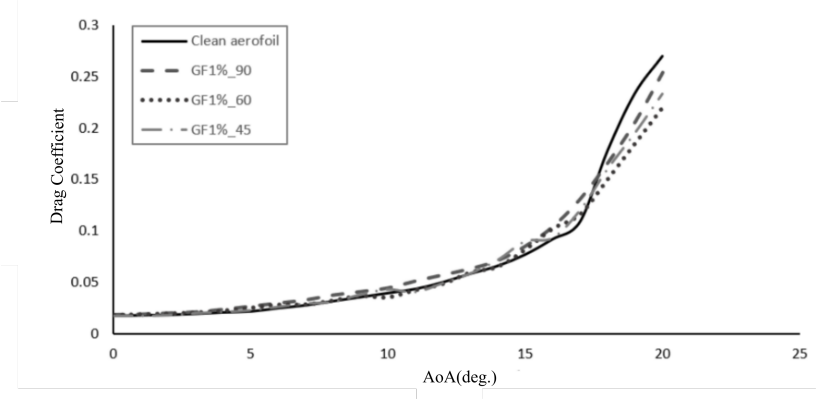


Fig. 4.16 Drag coefficient variation with aerofoil's angle of attack.

## 4.4 Flow Control in a H-type Darrieus Turbine

### 4.4.1 Dynamic characteristics of the 2D clean VAWT

As a reference case, the flow field and aerodynamic characteristics for the VAWT without flap control are firstly discussed in this section.

#### Grid independence

In the first step, the analysis of grid independence was carried out for the unmodified turbine. In order to capture the fluid flow structure, the mesh near the blade wall boundaries were well refined with three meshes of different total cells and the size of the first layer of grid cells. Mesh 1, Mesh 2 and Mesh 3 have $0.179 \times 10^6$, $0.546 \times 10^6$ and $0.713 \times 10^6$ cells respectively. As the torque coefficient is sensitive to the mesh quality near the blade surface, it is chosen as the criteria for evaluation. Figure 4.17 shows the comparison of the time-averaged torque coefficient for one rotation cycle and for one blade of the different mesh resolutions at TSR=2. It clear that there is a large discrepancy between the coarsest grid and medium one. The peak value of torque coefficient over one cycle is 0.241, which is 10.4% lower than the value from Mesh 2 and Mesh 3. Since there is only very little difference between medium and the finest meshes, the mesh of the medium size is sufficient enough to obtain reliable results with $0.546 \times 10^6$ cells in total. The height of the first grid cell near the wall is $3.2 \times 10^{-5}$m.

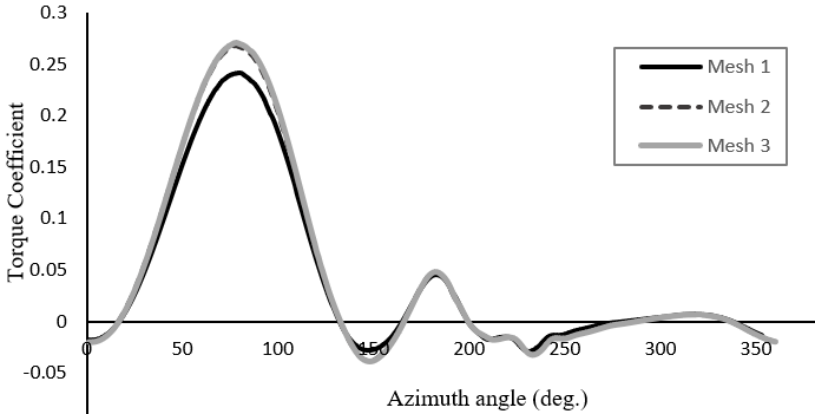


Fig. 4.17 Torque coefficient vs. Azimuth angle at TSR=2.

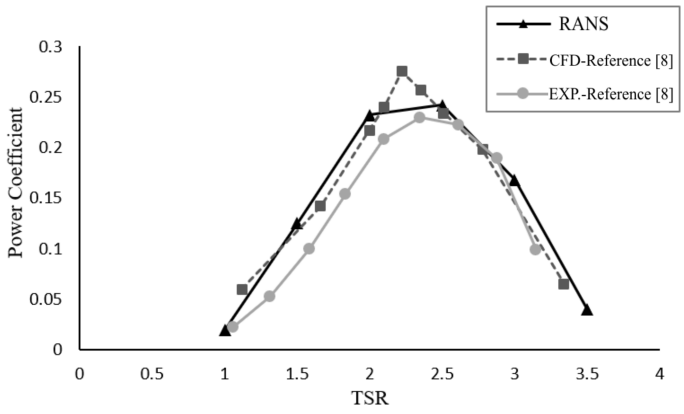


Fig. 4.18 Comparison of power coefficient of VAWTs of experiment and CFD results [8].

**Validation of numerical simulation**

The verification of the computational framework of VAWTs was conducted by comparing to published results [8]. Figure 4.18 shows the comparison of measured data [8] and the current CFD results in terms of the power coefficient variation with the tip speed ratio. The rotor's characteristics in current study is the same as in the publication (experiment and numerical simulation by Balduzzi [8] ).

According to the tested conditions, the tip speed ratios are from 1 to 3.5. It is obvious that the present numerical result has a similar variation as the reference numerical simulation and experimental measured results. The simulation results obtained by 2D methods overestimates the results as compared to the experimental data. This is mainly due to the omission of the 3D effects and the tip losses which occur in the wind tunnel test and these are not accounted for

in the 2D model. This difference has been reported in many similar researches [3][51][15]. However the difference does not change the behavior of the $C_P$ with the variation of TSR and the difference with the CFD reference result is small. This demonstrates that the present CFD procedure and grid distribution are suitable for predicting the aerodynamic performance of this rotor model. This good match is partly due to the fact that in the experiment a very long blade was chosen to reduce the influence of the tip-loss [8].

**2D Unsteady Flow Field**

Figure 4.20 shows the variation of the AoA in one revolution as the function of azimuth angle at TSR=2. The combining torques generated by the three turbine blades is shown in Figure 4.19. Take Blade 1 for discussion, at a very small azimuth angle from $\theta = 0^\circ$ to $\theta = 10^\circ$, the lift is very small because of the low AoA as in Figure 4.20 and its direction is almost perpendicular to the aerofoil chord line. Negative torque was generated and the minimum phase averaged $C_m$ is obtained at $\theta = 10^\circ$. After that, the torque coefficient starts to increase with the increase in AoA. Positive torque starts to appear at $\theta = 20^\circ$ and reaches the peak value at around $\theta = 90^\circ$, whose AoA is about 26.5°. With the increase of AoA, stall occurs on the blade leading to lift decrease and thus torque decrease. The value of AoA reaches the maximum value of 29.9° at $\theta = 125^\circ$. Then it goes down to 0° at $\theta = 180^\circ$. As a result, the lift and torque generation decrease.

In the downstream half cycle, although the variation of the absolute value of AoA has a trend similar with that the upstream half cycle, the torque generation is very small. This is because the majority of kinetic energy from wind has been extracted by the turbine in the upstream half cycle. Therefore, the wind flow reaches the downstream region of the rotor has relatively a smaller velocity and thus a lower kinetic energy.

The wake vortex structures in the flow field at TSR=2 are presented in Figure 4.21. It can be seen that there are two typical wake structures: longitudinal wake and circular wake. The longitudinal wake appears when the blade moves windward in a rotation cycle. When the blade moves against the wind stream, several circular areas with high vorticity magnitude occur pointing to the reduced aerodynamic efficiency of the blade and thus its very reduced torque coefficient as seen in the Figure 4.17. It should be noticed that the blade would has interaction with the vortex produce by the upstream blade, which made the flow field more complicated.

The evolution of the wake structure is shown in Figure 4.22 for one rotating cycle. Figures 4.22 (a) to (d) illustrate the vorticity magnitude distribution in the flow field at $\theta = 0^\circ$, $\theta = 90^\circ$ , $\theta = 180^\circ$ and $\theta = 270^\circ$ respectively. The distribution of the longitudinal

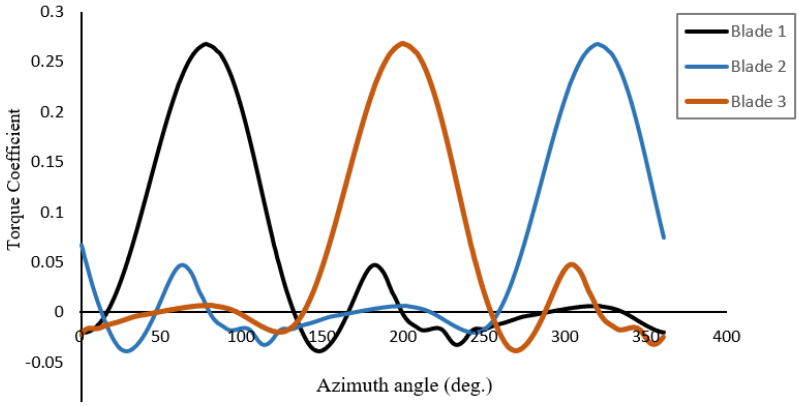


Fig. 4.19 Moment coefficient of three blades vs. Azimuth angle, at TSR=2

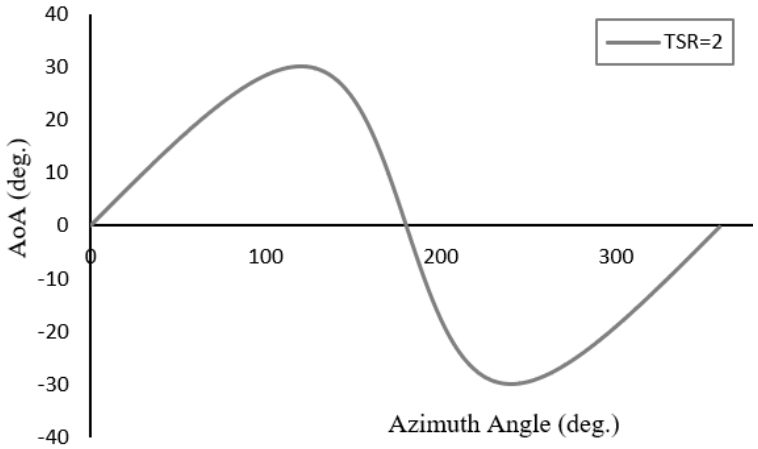


Fig. 4.20 AoA vs. Azimuth angle at TSR=2.

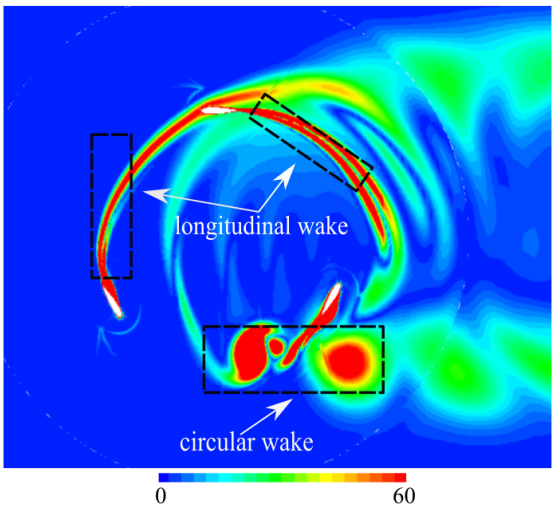


Fig. 4.21 The structure of wake vortex in the flow field, at TSR=2.

and circular wakes is consistent with the previous discussion. It should be noticed that there is aerodynamic interaction between the blades and the wake. The wakes behind the different blades also interact with each other. As shown in Figure 4.22 (a) and (b), the blade moves into the wake of the former blade in the downstream half cycle, which leads to a reduction of the lift and power generation. As a result, the relatively low torque coefficient is obtained in the downstream region as compared with that in the upstream half cycle.

The vorticity contour in areas surrounding the blades at various azimuth angles is shown in Figure 4.23. The aerofoils in Figures 4.23 (a), (d) and (f), move windward with the longitudinal wake, while Figures 4.23 (b), (c) and (e) show the vorticity magnitude distribution around the aerofoils that move against the direction of the wind velocity with a circular wake at the trailing edges of the aerofoils.

In Figure 4.23 (a), the flow surrounding the blade is attached to the wall surface and there is no separation at $\alpha = 16.1^{\circ}$. However, the isolated aerofoil experiences flow separation on the suction side at similar AoA and Reynolds number as in the analysis shown in the last section. This indicates that the flow mechanism of the aerofoil has been changed in the rotation process. The difference of flow behavior can be observed in Figure 4.23 (c) and (e). Although in both cases, the angle of the attack is small, the aerofoil is Figure 4.23 (e) experiences deep flow separation, while the flow around the aerofoil in Figure 4.23 (c) stays attached because of the different flow structures when the blade moves windward or leeward.

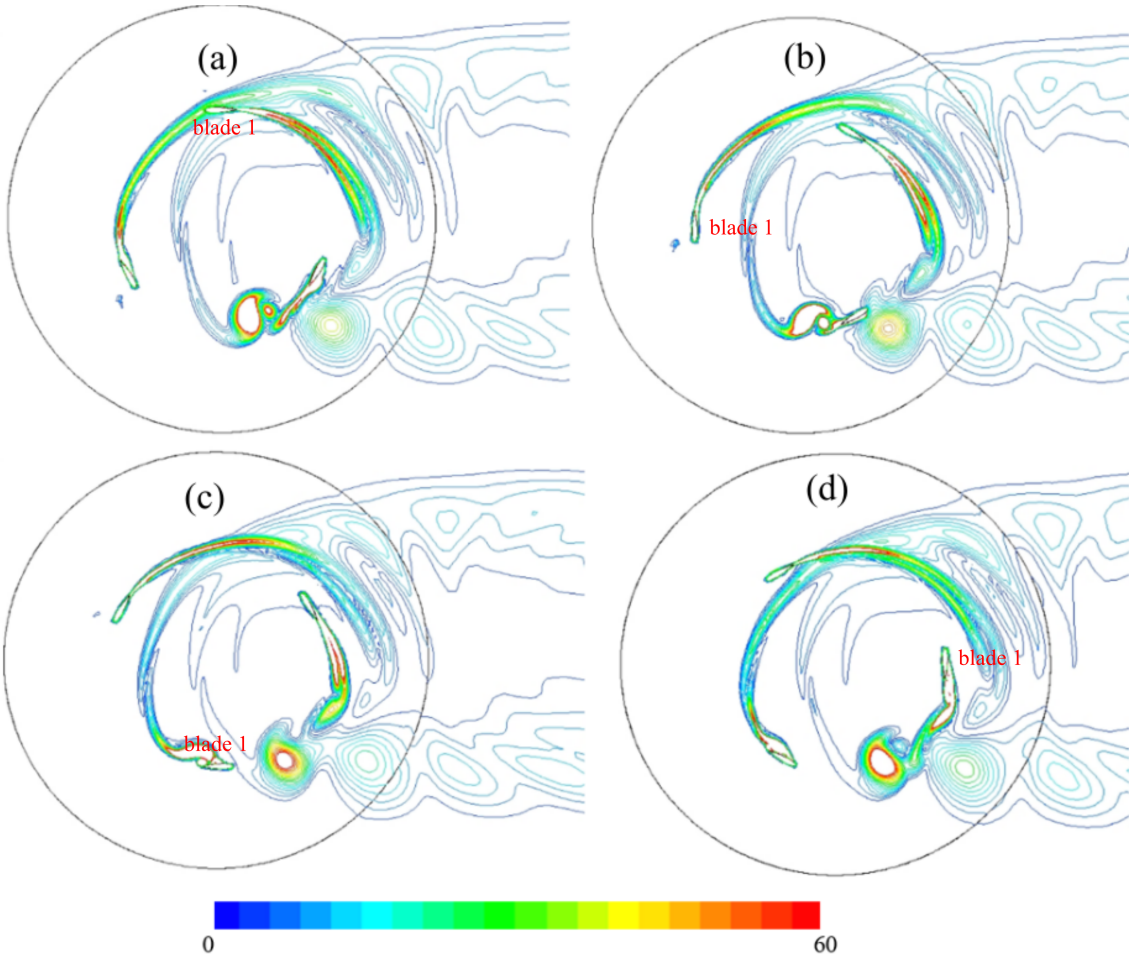


Fig. 4.22 Vorticity magnitude distribution at (a) $\theta = 0°$, (b) $\theta = 90°$,(c) $\theta = 180°$, (d) $\theta = 270°$, at TSR=2.

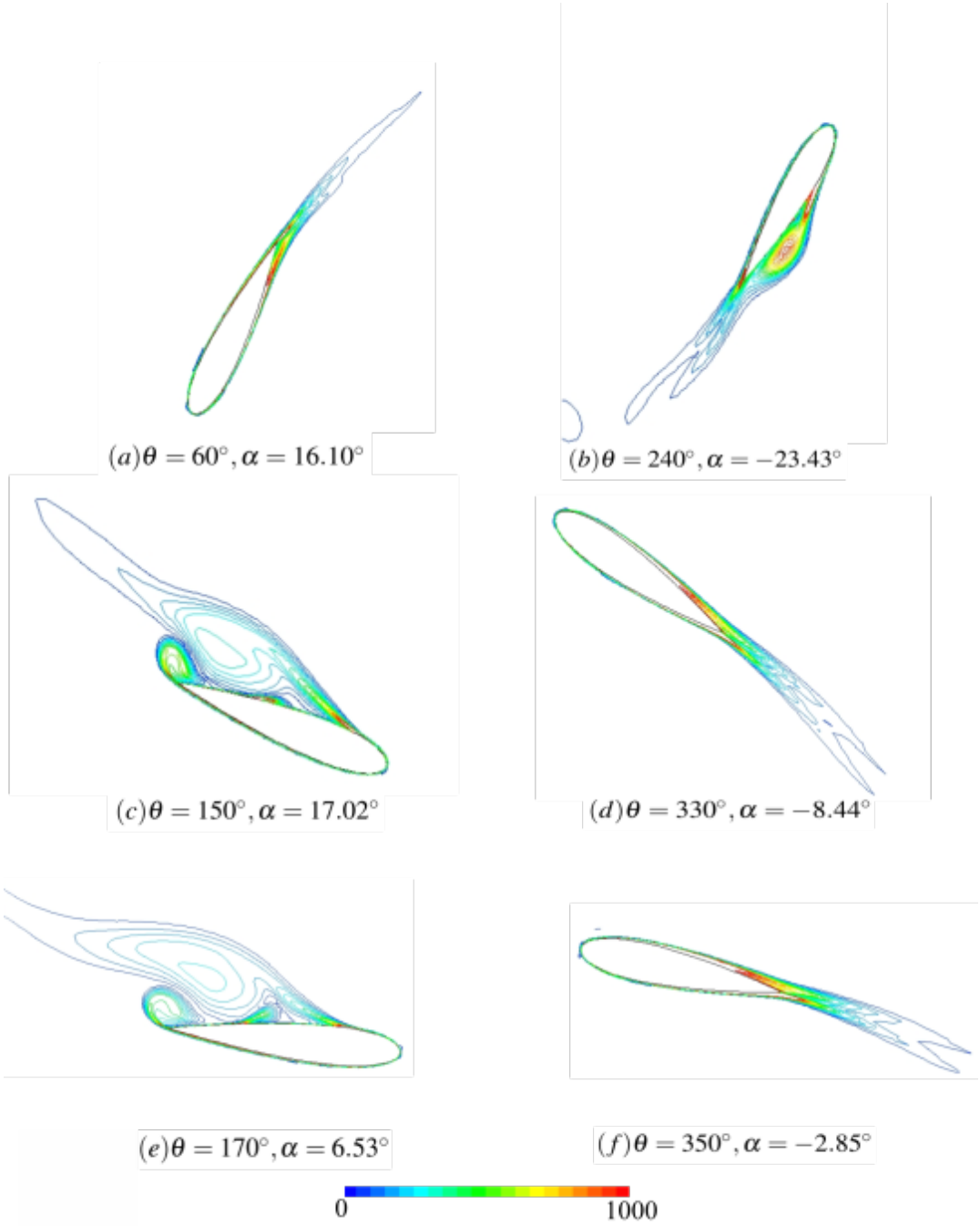


Fig. 4.23 Vorticity magnitude distribution at (a) $\theta = 0°$, (b) $\theta = 90°$,(c) $\theta = 180°$, (d) $\theta = 270°$.

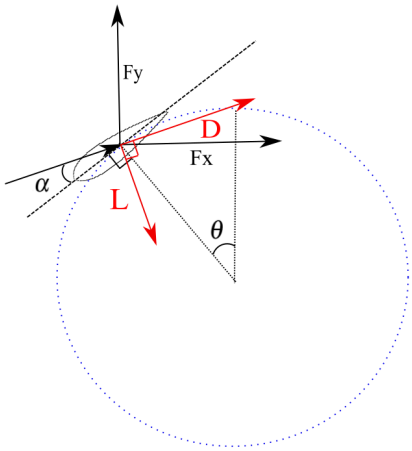


Fig. 4.24 Schemetic view of the dynamic forces on the blade.

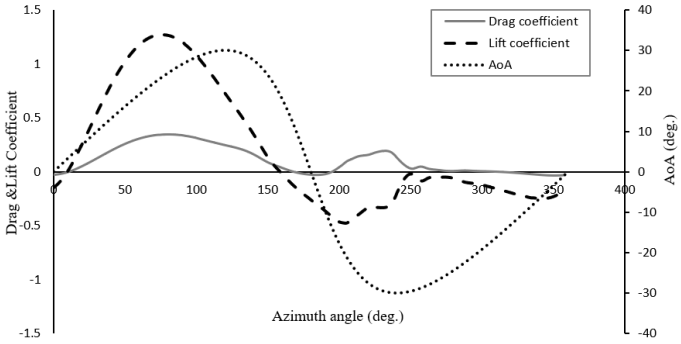


Fig. 4.25 Drag, lift coefficient and angle of attack variation with azimuth angle.

The force data in X and Y directions ($F_x$ and $F_y$) were extracted from the numerical method and converted into instantaneous lift and drag coefficient as equations below. The directions of $F_x$, $F_y$, lift and drag are shown in Figure 4.24.

$$D = cos\alpha(F_x cos\theta + F_y sin\theta) - sin\alpha(F_y cos\theta - F_x sin\theta) \tag{4.4}$$

$$L = -sin\alpha(F_x cos\theta + F_y sin\theta) - cos\alpha(F_y cos\theta - F_x sin\theta) \tag{4.5}$$

The variations of dynamic lift and drag coefficients during the rotation cycle are shown in Figure 4.25. In the upstream half cycle, a maximum lift coefficient of 1.24 is found at $\theta = 78°$. The maximum $C_L$ is improved by 27.7% compared to the statically isolated aerofoil. For the drag coefficient, the maximum value 0.343 is achieved at $\theta = 85°$, $\alpha = 25.29°$.

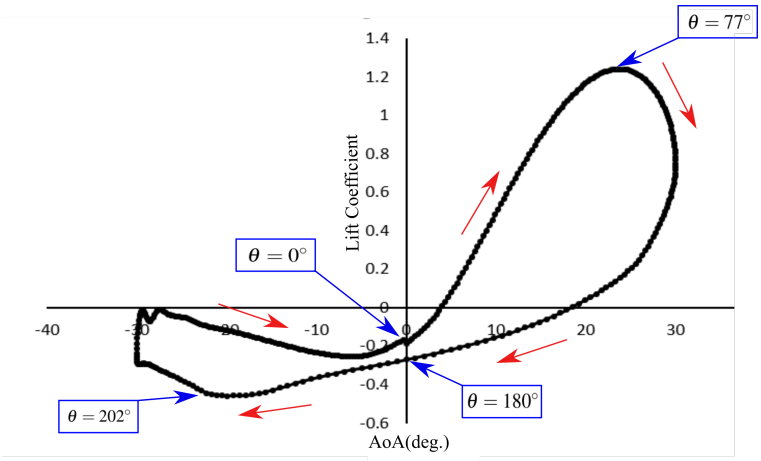


Fig. 4.26 Phase-averaged lift coefficient variation with angle of attack (AoA) of one blade for the unmodified aerofoil at TSR=2.

In order to investigate the characteristics of the rotor blades quantitatively, lift and drag coefficients against AoA of one blade are plotted in Figures 4.26 and 4.27. The arrows indicate the rotation direction of the rotor blade. The extreme values of $C_L$ and $C_D$ are labeled with the corresponding azimuth angles. At $\theta = 0^\circ$, although the AoA is $0^\circ$, the lift has a small value due to wake impingement as compared to the stationary aerofoil. In contrast to the $\theta = 0^\circ$ case, a relatively higher $C_L$ can be observed at $\theta = 180^\circ$ ($\alpha = 0^\circ$), which indicates the different flow field in which the rotor blade moves windward and leeward in one revolution. The blade at $\theta = 0^\circ$ travels into the wake generated by the former blade as shown in Figure 4.23 (a). In the downstream half cycle, the lift is much lower as compared to that in the upstream half cycle. It was also found that the blade in upstream half cycle plays the main role of lift generation. This because the majority of wind kinetic energy is extracted by the rotor of upstream half cycle. The velocity of the wind reaching the downstream half cycle of rotor is very low.

In addition to the lift coefficient, the drag variation of the single blade in one revolution with the azimuth angle is shown in Figure 4.27 at TSR=2. The maximum drag coefficient of 0.35 is observed at $\theta = 80^\circ$ in the motion of upstream half cycle. Similar to the lift coefficient, the drag in the downstream half cycle is much lower than that in the upstream half cycle.

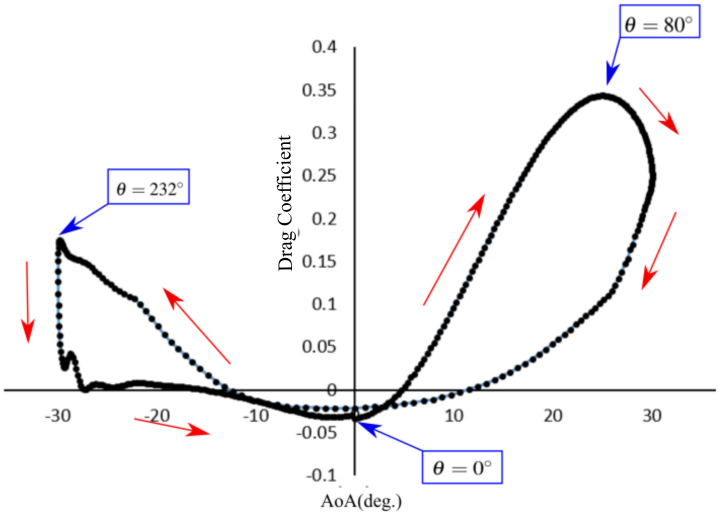


Fig. 4.27 Phase-averaged drag coefficient variation with angle of attack (AoA) of one blade for the unmodified aerofoil at TSR=2.

### 4.4.2 Flow control characteristics of the modified VAWT

#### Vorticity dynamics analysis

Based on the analysis of the aerodynamic characteristics of the isolated aerofoil with the GF flow control and the flow field around rotor blade, a GF control strategy is proposed to improve the performance and efficiency of the VAWT in the section. The GFs are mounted to the outside surfaces of the turbine blades. This is to improve the performance of the first half revolution, where the outside of the turbine blade acts as the pressure surface of the aerofoil and the GF was proved to be effective when it was installed on the pressure side.

Figure 4.28 shows the vorticity contour for the flow field around the rotor blade at various azimuth angles in the upwind half cycle, without and with flap control. The VAWT with 1%c and 2%c GF are chosen for analysis. It can be seen that the wake vortex structures have been substantially changed by the flap control, compared with the unmodified model. It was found that the GF restrains the formation and development of wake vortices near the aerofoil at $\theta = 90°$, $\theta = 120°$,$\theta = 150°$ and $\theta = 180°$. The vortex shedding can be observed in the improved models at $\theta = 120°$,$\theta = 150°$ and $\theta = 180°$ with less flow separation on the suction surface of the blade in comparison with the unmodified model. The dynamic stall condition is relatively softer for GF cases in comparison with the clean turbine blade at the azimuth angles selected in the figure. As the large proportion of power is generated in the upwind half cycle of one revolution, a large difference of power generation can be obtained

for the VAWT with and without GF control. The discrepancy of the wake structure of the two improved models with 1%c and 2%c GF is not significant.

Figure 4.29 further shows a comparison of the streamlines over a blade for three different models at $\theta = 85^\circ$. As shown in Figure 4.29 (a), flow separation occurs almost at the leading edge on the suction surface of the aerofoil. When 1%c GF control is applied as Figure 4.29 (b), separation length is less than that of the unmodified case and the area of the vortex is reduced with the attachment of GF, leading to an enhancement in torque coefficient generated by the blade. A similar trend can be observed in the model with 2%c GF as Figure 4.29 (c) where flow separation is reduced by the favorable modifications. Therefore, the GF is shown to be an effective flow control technique to suppress the flow separation [113].

### Dynamic force analysis

The variation of the dynamic lift of one turbine blade versus the angle of attack for one revolution at TSR=2 is shown in Figure 4.30. The unmodified turbine is compared with the control systems equipped with 2%c GF. The definition of $C_L$ is the same as the baseline case in the last section. The effect of dynamic stall reduction of the GF can be observed in this figure, which shows that in the upwind region the lift increases significantly from $\theta = 35^\circ$ to $\theta = 224^\circ$ with GF modification. The maximum dynamic lift coefficient was improved by 19.3% with the GF modification reaching 1.55.

### Moment and power coefficient

The power output from the turbine is of practical interest. Figure 4.31 shows the torque coefficient versus the azimuth angle in one revolution for one blade with and without GF control, at TSR=2. As seen in the figure, in the upwind region, the turbine with the flap control has a higher torque output than the unmodified model at the azimuth angle ranging from $\theta = 0^\circ$ to $\theta = 165^\circ$. Similar result about the effect of GF on the torque coefficient was obtained by Bianchini et al [9]. The effect of GF with the height of 2%c is relatively larger in comparison with 1%c GF, corresponding to the vorticity distribution in Figure 4.28.

The torque variation at a higher TSR (TSR=3) is illustrated in Figure 4.32. As seen in the figure, similar to the curve of TSR=2, the GFs can improve the torque generation of the turbine blade in the first half revolution at the azimuth angle ranging from $26^\circ$ to $112^\circ$. However, the improvement is not that obvious as compared to the low TSRs. In the downstream half cycle, the significant negative influence of GFs for power output can be observed for the cases of both 1%c and 2%c GFs in comparison with the unmodified turbine.

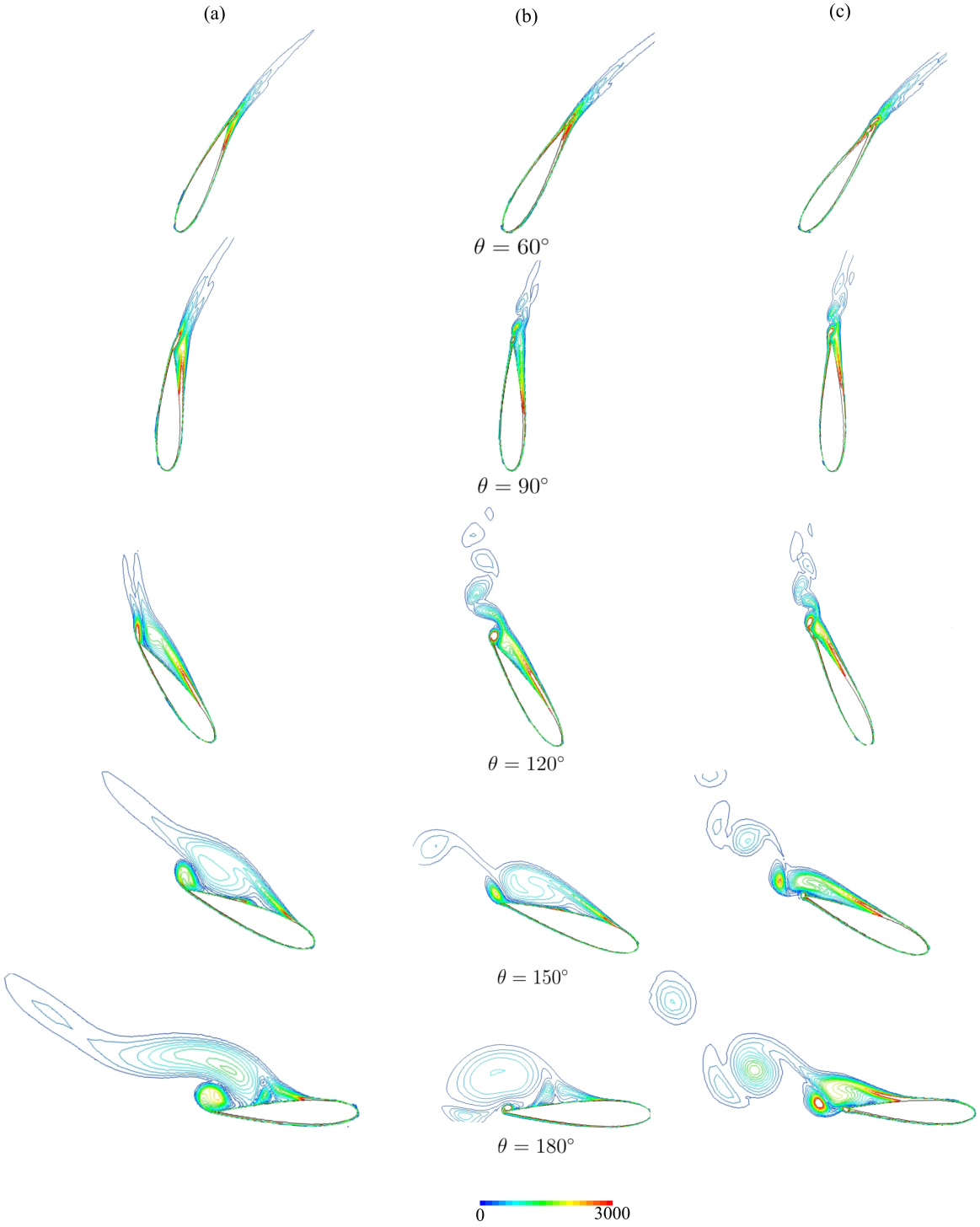


Fig. 4.28 Vorticity distribution in the nearby flow field around the aerofoil at TSR=2. (a) Without GF.(b) With 1%c GF. (c) With 2%c GF

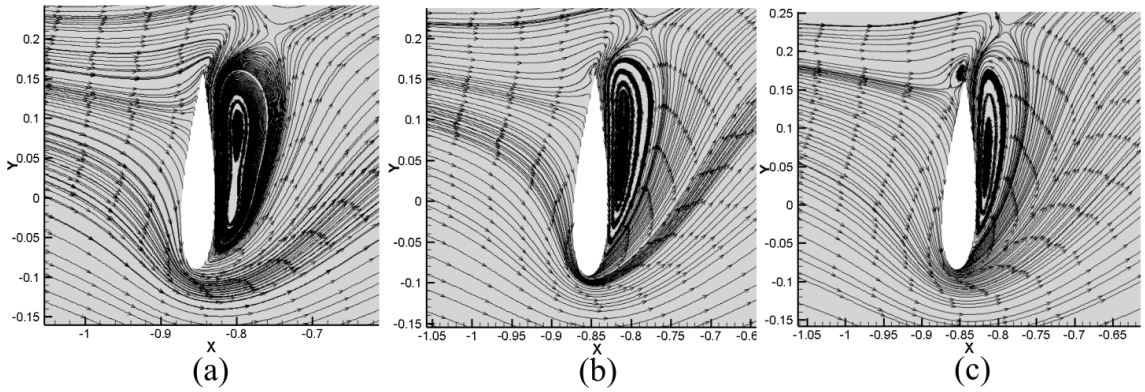


Fig. 4.29 Comparison of the time-averaged streamlines around the blade at $\theta = 85^\circ$ at TSR=2.(a) Without GF. (b) With 1%c GF. (C) With 2%c GF

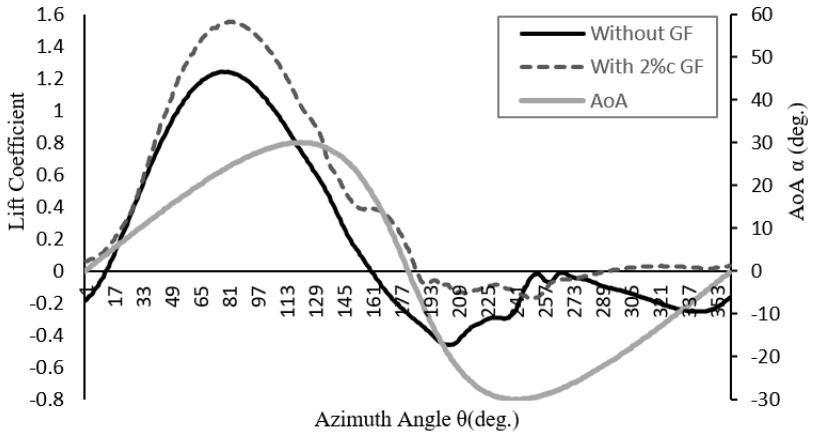


Fig. 4.30 Phase-averaged lift coefficient variation in one revolution at TSR=2.

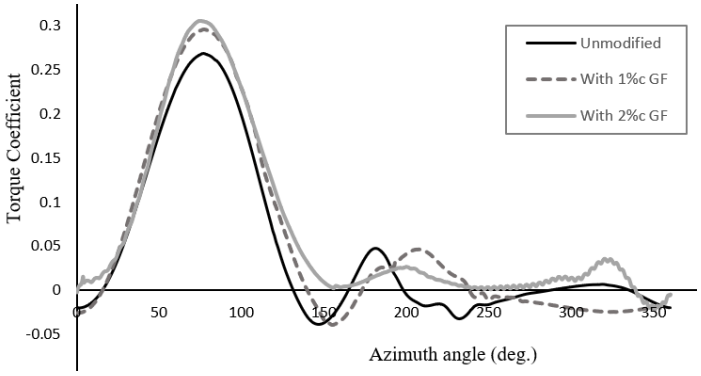


Fig. 4.31 Torque coefficient versus azimuth angle for different VAWTs, TSR=2.

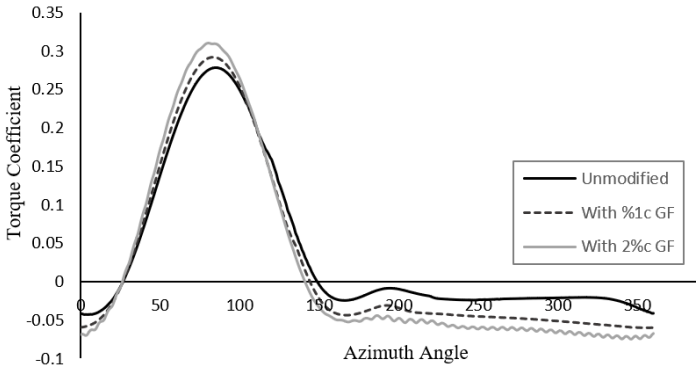


Fig. 4.32 Torque coefficient versus azimuth angle for different VAWTs, TSR=3.

This results in a lower power coefficient at higher TSRs as shown in Figure 4.33, which shows a comparison of the power coefficient between the baseline case and GF cases at several TSRs. By the way, for the torque profile,looking closely to the last 110 degree of the downstream in Figure 4.31 and the downstream half cycle in Figure 4.32, it could be identified oscillation of the torque coefficient because of the the onset of vortex shedding, which could be also found in the study by Bianchini et al.[9].

It can be seen that adding the GFs increases the power coefficient at lower TSRs (from 1 to 2). However, as the TSR goes above 2.5, both 1%c and 2%c GFs reduce the power coefficient.

At TSR=1, the $C_P$ does not change too much with different heights of GFs. However, as the TSR increases to 1.5, a noticeable enhancement of the $C_P$ can be observed from the models with different GFs compared with the unmodified turbine. It is interesting that the peak performance of the clean blade is at TSR=2.5. However, when a GF is installed, the power coefficient peaks at TSR=2. It is also clear that the 2%c GF offers the best effect in power generation for the turbine at TSR=1.5 and 2, while the 1%c GF performs better at other selected TSRs.

The kinetic energy of wind extracted by the turbine rotor is transferred to beneficial power including electric energy generated by the wind turbine. The kinetic energy of the wind that is left downstream is a loss, particularly when having unsteadiness as exhibited in the turbulent kinetic energy. It was assumed that the wind kinetic energy accepted by the turbine was the sum of mechanical energy of the rotor, kinetic energy of wind past the rotor and the turbulent kinetic energy, since the energy of other portion like internal energy, is very small and eliminated. Figures 4.34 and 4.35 compare the distribution of the turbulent kinetic energy and velocity magnitude in the flow field of turbines with and without GF at

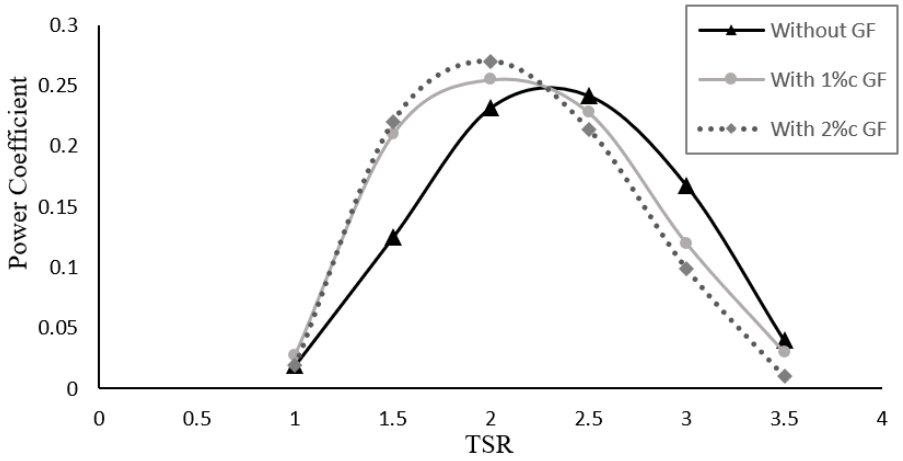


Fig. 4.33 Comparison of power coefficient of VAWTs with and without GFs.

TSR=1.5.It can be seen that there is no obvious discrepancy of the turbulent kinetic energy distribution downstream the wind turbine between the models with and without flap control.

However, in Figure 4.35 the instantaneous velocity magnitude of the flow in the downstream region equipped with 1%c and 2%c GF is obviously lower than the unmodified turbine, which indicates that the wind passed the rotor has a relatively smaller kinetic energy in modified turbine. Since the wake turbulent kinetic energy and heat loss is very similar for both cases, the modified turbine extracted more energy from wind compared with the clean turbine and can transfer more kinetic energy into electrical power as seen by the distribution of the wake's time-averaged velocity magnitude. Therefore, the 1%c and 2%c GFs can improve the power generation of the VAWT, leading to a higher power coefficient.

## 4.5 Conclusions

The major aim of this chapter was to provide useful engineering insight into the aerodynamics of a small vertical axis wind turbine with a Gurney flap.

For this purpose, numerical simulation was performed on the two dimensional aerofoil NACA 0018 and H-type Darrieus wind turbine based on the same aerofoil. Through an analysis of grid sensitivity and the validation of experimental results , this CFD process was shown to be reliable.

1. The effect of the GF with the height of 1%c to 5%c on the performance of the isolated aerofoil was examined. It was found that the GF can improve the lift coefficient of the

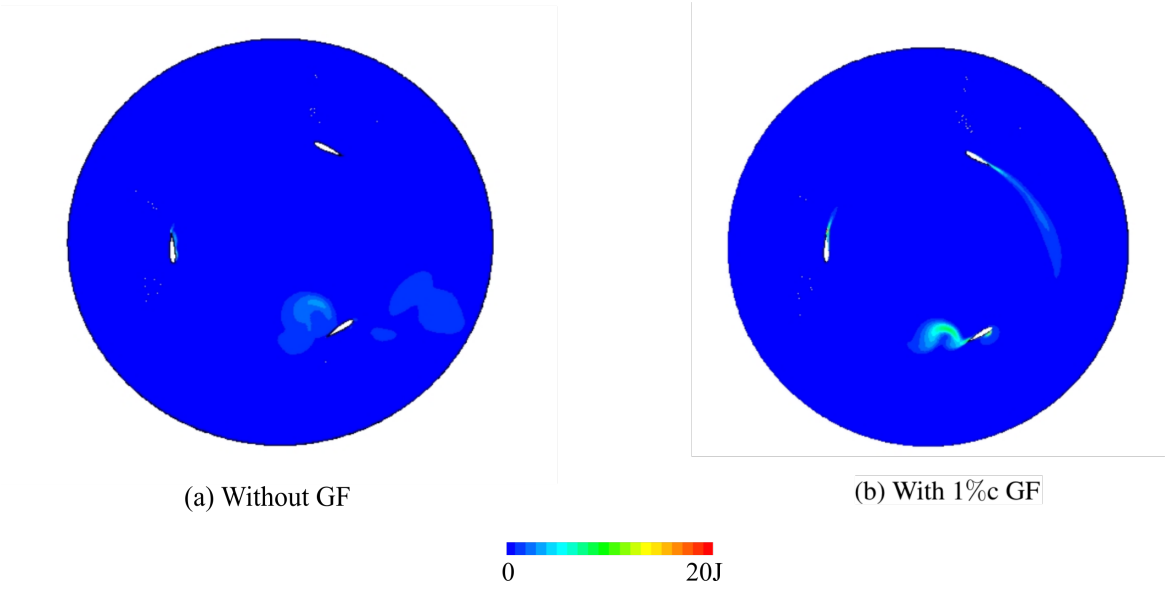


Fig. 4.34 Distribution of instantaneous turbulent kinetic energy at TSR=2.

aerofoil but also mildly reduce the stall angle. This enhancement becomes even greater when the height of Gurney flap increased.

2. For the tested Gfs with different mounting angles, the results indicated that the Gurney flap perpendicular to the chord line of aerofoil had the best effect compared to that with other mounting angles.

3. For the VAWT, the GFs can improve the aerodynamic performance of the VAWT in the upstream region, resulting in an overall improvement for low TSRs, while showing a reduced overall performance for high TSR. The GFs improve the torque coefficient of the rotor blade at the azimuth angle ranging from 0° to 180°.

4. It was found that the GF can diminish the trend of flow separation near the blade trailing edge and delay the dynamic stall by examining the flow detail near the rotor blade. The velocity magnitude contour in the flow field further shows that power generation is improved by adding the GFs on the VAWT for low TSR. Hence, this study points to the potential in using Gurney flaps in vertical axis wind turbine design.

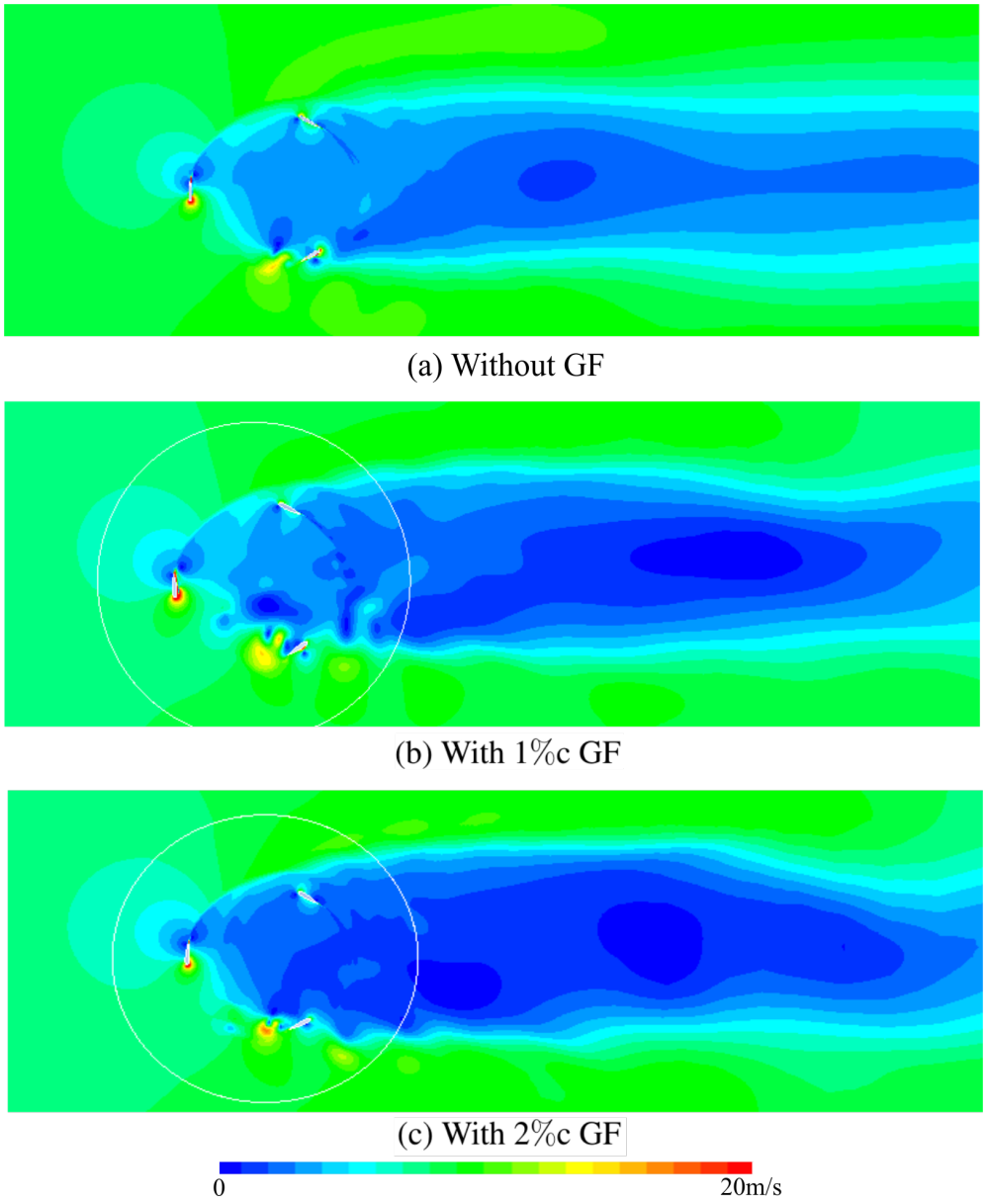


Fig. 4.35 Distribution of instantaneous velocity magnitude at TSR=2.

# Chapter 5

# Performance of Micro-vortex Generator on Aerofoil and Vertical Axis Turbine

## 5.1 Introduction

Passive micro vortex generators (VGs) have been widely used flow control devices for various aerodynamic applications, especially in the wind turbine industry for many years. The main objective of this work is to find an effective configuration of MVGs for an isolated aerofoil and a small-scale vertical axis wind turbine. Using the Computational Fluid Dynamics codes Code_Saturne and Ansys-Fluent, the present work aims to determine the optimal variables of MVGs including mounting angle, location and configuration, and investigate their aerodynamic effects on the turbines.

## 5.2 Geometry and Case Setup

### 5.2.1 A single Micro-Vortex Generator On the Plane

In order to understand the flow control's effect of MVGs and carry out the code validation, a single MVG perpendicularly installed on a flat plane is investigated first. The computational domain and mesh distribution on the wall surface are shown in Figure5.1. The mounting angle is set at 16º and the free stream velocity is 34.0 m/s. The MVG has a height of 7 mm and a length of 49 mm. It is mounted at the position where the thickness of the boundary layer is about 35mm. The length of the computational domain is about 4 m, which is nearly 1000 times of the length of the MVG. The total number of hexahedron cells are 2.34 million. The boundary conditions are labeled in Figure5.1 as inlet, outlet, symmetry and non-slip

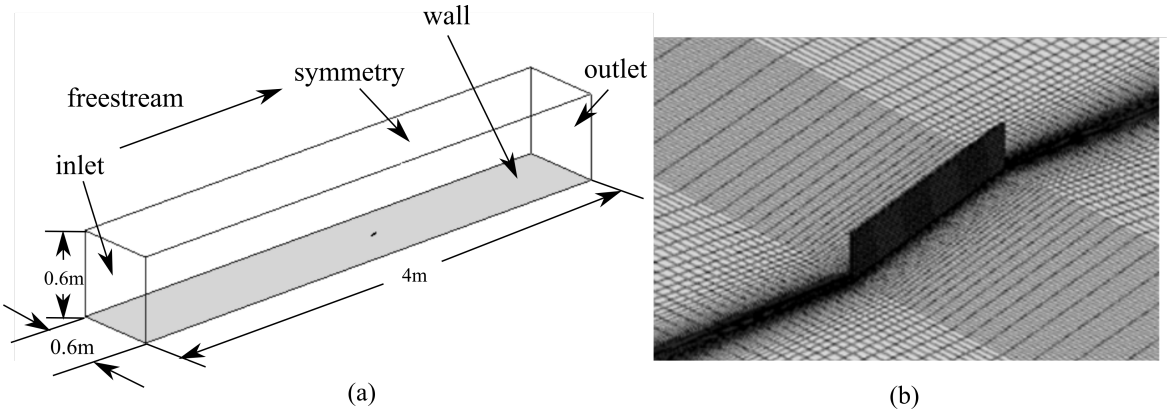


Fig. 5.1 Geometry (a) and mesh (b) in the local region around MVGs.

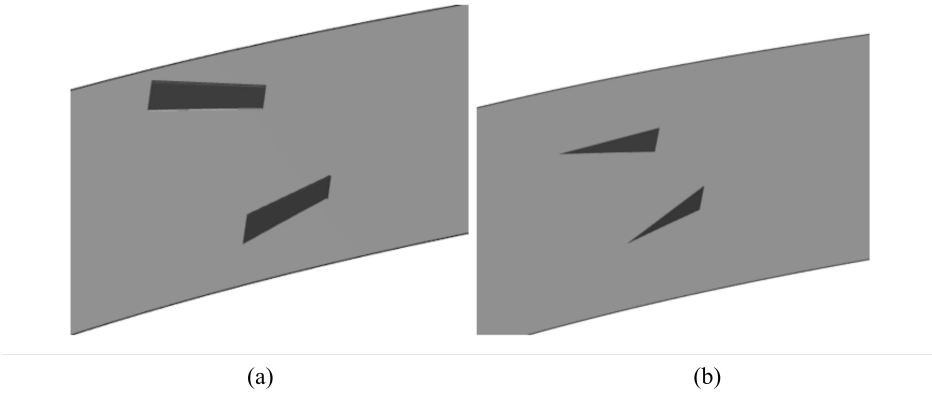


Fig. 5.2 (a) Aerofoil with rectangular MVGs. (b) Aerofoil with triangular MVGs.

wall. The inlet boundary is defined based on the free stream velocity 34 m/s. The downwind outlet is defined as pressure outlet, where static pressure is specified.

### 5.2.2 MVGs on A Single Stationary Aerofoil

Micro-Vortex Generators on the NACA0018 aerofoil were studied by unsteady Reynolds-averaged Navier–Stokes (URANS) method. It was sufficiently accurate and use Large Eddy Simulation (LES) did not change the results for the single stationary aerofoil. Both methods are detailed in Chapter 3. This NACA 0018 profile is typical for VAWTs. Figure 5.2 illustrates the geometry of the aerofoil section equipped with one pair of MVGs of rectangular and triangular shapes with counter rotating configuration.

Optimization of MVGs has been discussed by several authors with the consideration of the variables including chordwise location, mounting angle and length [32]. The study by Mueller-Vahl et al. shows that the MVGs located at 15% to 20% chord length from the

leading edge of the aerofoil is ideal to realize the stall delay [84]. The wind tunnel test by Ashill indicates that the low-profile VGs set an angle of about 16° is effective in flow separation control [4]. Therefore, Table 5.1 presents eight MVG models of various geometric parameters and among these MVGs, model A is regarded as the benchmark model.

Table 5.1 Tested MVG Models on the Aerofoil

| Test Case | Configuration | Shape | Position | Angle($\beta$) | e/h |
|---|---|---|---|---|---|
| A | Counter-rotating | Rectangle | 20%c | 16° | 3 |
| B | Counter-rotating | Rectangle | 20%c | 19° | 3 |
| C | Counter-rotating | Rectangle | 20%c | 22° | 3 |
| D | Counter-rotating | Rectangle | 15%c | 16° | 3 |
| E | Counter-rotating | Rectangle | 22%c | 16° | 3 |
| F | Counter-rotating | Rectangle | 25%c | 16° | 3 |
| G | Counter-rotating | Triangle | 20%c | 16° | 3 |
| H | Counter-rotating | Rectangle | 20%c | 16° | 3 |

The chord length of the aerofoil is 0.246 m and the computational domain spanwise length is about 30% of the chord length. The free stream velocity is 10 m/s and the Reynolds number based on the aerofoil chord length is $1.6 \times 10^5$. In all models, the height of the MVGs was about 1% of the aerofoil chord length. The pitch spacing between the adjacent MVGs is three times of its height in order to eliminate the influence between each other.

The common C-H type mesh was adopted as Figure 5.3. The Farfield boundary was located 40 times of chord length away from the aerofoil. Velocity INLET and pressure OUTLET boundary conditions were applied at the inlet and outlet domain, respectively. The aerofoil and MVGs were set as non slip walls. A periodic condition is enforced at the spanwise direction. The structured grid was deployed in the whole domain. There were 300 points along the surface of the aerofoil.

### 5.2.3 VAWT with VGs

After the validation and flow study of the isolated aerofoil, an H-type Darrieus vertical wind turbine will be investigated using the Large Eddy Simulation (LES) method. The LES was found to account better for the cyclic motion of the blades and the associated turbulent structures. Hence LES was used for this section of study. The schematic view of this turbine is given in Figure 5.4. This wind turbine consists of three vertical blades, one vertical support and six horizontal struts.

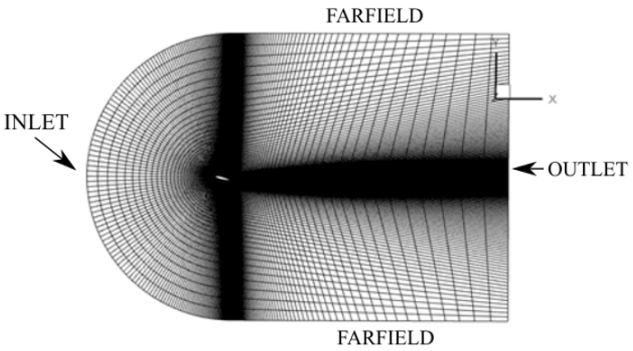


Fig. 5.3 C-H type computational domain.

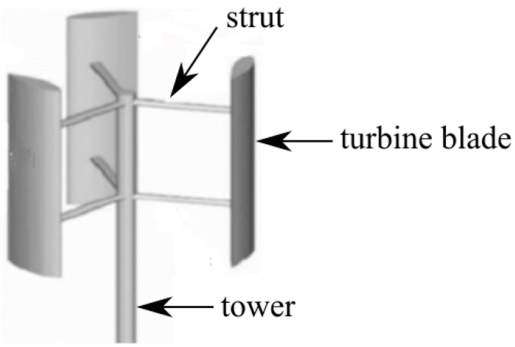


Fig. 5.4 H-type vertical axis wind turbine.

The geometry of the computational domain and the boundary conditions are given in Figure 5.5(a). To have high-quality meshing, supporting arms, central shaft are not included in the current computational domain. As the rotor is a moving surface, the whole computational domain was divided into two sub-domains (ROTOR and STATOR domains) with an interface between them. The ROTOR domain is a circular inner zone that includes the wind turbine. This ROTOR domain rotates at a fixed angular velocity. The STATOR domain is a large stationary rectangular domain outside the inner zone. The mesh cells on both sides of the interface have the same size to achieve a smooth and sliding transition.

This wind turbine blade is the NACA 0018 aerofoil that was discussed in the last section, which can provide high lift-to-drag ratio. The main turbine parameters are given in Table 5.2.

The turbine is assumed to operate in an open field. To avoid wall blockage, the length and width of the STATOR domain are 40R and 10R respectively. The radius of the ROTOR zone is 1.2 times of the turbine radius. Figure 5.5(b) shows a zoom-in view of the mesh around the turbine blades. The inlet boundary was set at a constant wind speed of 8 m/s, while the atmospheric pressure boundary was imposed at the outlet. The symmetry boundary

Table 5.2 Rotor Parameters

| | |
|---|---|
| Number of blades | 3 |
| Blades aerofoil | NACA 0018 |
| Blade chord(c)[m] | 0.246 |
| Radius(R)[m] | 0.85 |
| Wind speed(V)[m/s] | 8 |
| Tip speed ratio | 1-3.5 |
| Height of blades(H)[m] | 0.08 |

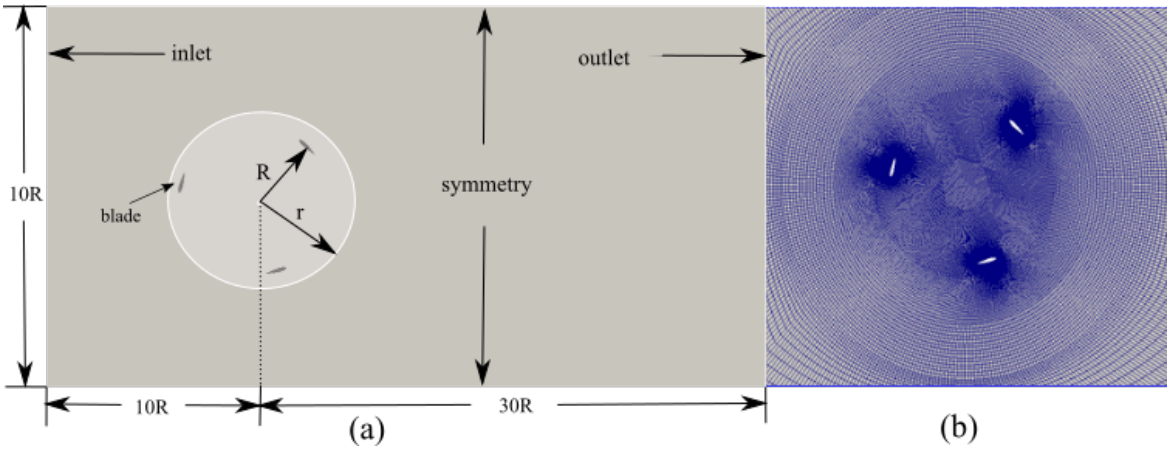


Fig. 5.5 (a) Computational domain (b) Mesh in the local region around turbine blades.

condition was adopted for the top and bottom boundaries in Figure 5.5(a). No-slip wall boundary condition is implemented on the blade and MVG surface.

Because the modeling of the full 3D turbine model of the VAWT is computationally expensive. The present model differs from a full 3D model in that only a certain length of blades is modeled with periodic boundaries at spanwise direction of the domain. As a result, this model essentially represents a VAWT with an infinitely long blade, and the influences of finite span or tip vortices were not taken into account in this model. Many researchers have focused on this method on turbine modeling instead of the full 3D model[**?** ].

The turbine operated with a fixed wind speed (V), whereas the rotational speed of the turbine ($\omega$) changes to achieve different tip speed ratios. The Tip Speed Ratio (TSR) is defined as $\lambda = R\omega/V$ (V stands for the wind velocity).

## 5.3 Numerical Method

Code_Saturne and ANSYS-Fluent were used for the CFD calculations in this study. Code_Saturne of EDF is a general-purpose open source CFD software package based on the finite volume method and a cell-centered approach. The LES simulations were performed by Code_Saturne in the current work, whereas the ANSYS Fluent simulation package was used for the (U)RANS calculations.

For the unsteady RANS Fluent calculation, the well-known two-equations SST (Shear Stress Transport) k-$\omega$ turbulence model proposed by Willcox was chosen [118]. This method attempts to predict turbulence by solving two equations for the extra two variables, turbulent kinetic energy (k) and specific dissipation rate ($\omega$). It blends the k-$\omega$ model and the k-$\varepsilon$ model, which performs better for wall-bounded cases, especially under the adverse pressure gradients [79]. The pressure-based solver with the second order spatial scheme and the SIMPLE time marching method were adopted. No wall function was applied as the mesh resolution near the wall is fine enough.

The LES calculations were performed by Code_Saturne, an unstructured, collocated finite-volume code. The predictor/corrector algorithm is used for pressure-velocity coupling to avoid odd-even oscillations. The fully centered convection scheme is used for the velocity. The Adams-Bashforth time scheme is used for the time integration of the convective term, whereas a Crank-Nicolson scheme is deployed for the time advancement of other terms. The implicit LES (ILES) is adopted for the current study. It uses the numerical dissipation as a subgrid model [6], and thus, no subgrid scale model is applied in the present study. Recently, there has been an increasing interest in the ILES approach and its effectiveness has been demonstrated in a wide range of applications for various fields from fluid engineering to astrophysical fluids computations [35].

For a typical VAWT large eddy simulation testcase in the present study, $3.59 \times 10^7$ cells are deployed to discretize the computational domain as show in Figure 5.5. Usually,the flow becomes fully developed after about ten revolutions, and then, the phase averaging was performed for the following five revolutions. The simulation is regarded to be fully developed if the instantaneous moment coefficient of the turbine was less than 1% different compared to the value of the same azimuth angle of last period. Running such a typical VAWT large eddy simulation testcase would need roughly CPU core hours.

## 5.4 Results and Analysis

### 5.4.1 A single MVG on the plane

The simulation of a single MVG installed on a flat plane has been compared with the experimental results, as shown in Figure 5.6 and Figure 5.7. Six streamwise stations behind the trailing edge of the MVG are given, which are s/h=10, 17, 50 and 109. Here, s is the distance between the station and the trailing edge of MVG. The column (a) in Figure 5.6 and Figure 5.7 present the experimental results from Yao et al.[122]. The experiment were conducted in the Langley 20- by 28-Inch Shear Flow Tunnel. The free-stream velocity is 34 m/s. A 12.7-mm thick splitter plate was used to eliminate any upstream influence. A single VG was located approximately 2.25 m downstream of the boundary layer trip where the boundary-layer thickness ($\theta$) was approximately 35 mm. The column (b) show the CFD results of RANS from Fluent. The present numerical study was conducted in the same conditions with the experiment in the literature by Yao et al [122].

As shown in Figure 5.6, the vortex development downstream of the trailing edge of MVG from the numerical calculations agrees qualitatively well with the measurement data. Figure 7 shows the contour of the streamwise velocity at measurement stations from RANS. As the vortex moves downstream from the generator, the size of vortex increases, but the intensity diminishes and the vortex core moves away from the flat plate. The transparent square in the figure denotes the spanwise location of the vortex generator. It can also be observed that the vortex core moves away from the spanwise location of the MVG when it travels downstream.

Figure 5.7 portrays the contour of the streamwise vorticity at different sections. As s/h increases, the magnitude of the streamwise vorticity decreases and at section s/h=109, the vortex has been fully diffused. This demonstrates the streamwise length in which the MVG can be effective, pointing to the need to carefully choose the location of MVG.

Figure 5.8 shows the comparison of between the numerical result in present work and the experimental data and CFD result from the literature by Yao [122] in terms of the variation of half-life radius of vortex [122]. The unsteady RANS of k-$\omega$ SST model was used in both CFD studies. The half-life radius is defined as the distance between the center of the vortex core and the position where the vorticity was equal to half of the peak vorticity. It was found that the half-life radius increases almost linearly with s and the curves of numerical results have the same trend with experimental data. The URANS result agrees well with each other in both CFD studies. The minor discrepancy between the two RANS results can be related to small difference in the solvers and the small difference in mesh setup. The CFD method overestimates the half-life radius by about 38% at s/h=10. As the vortex is not

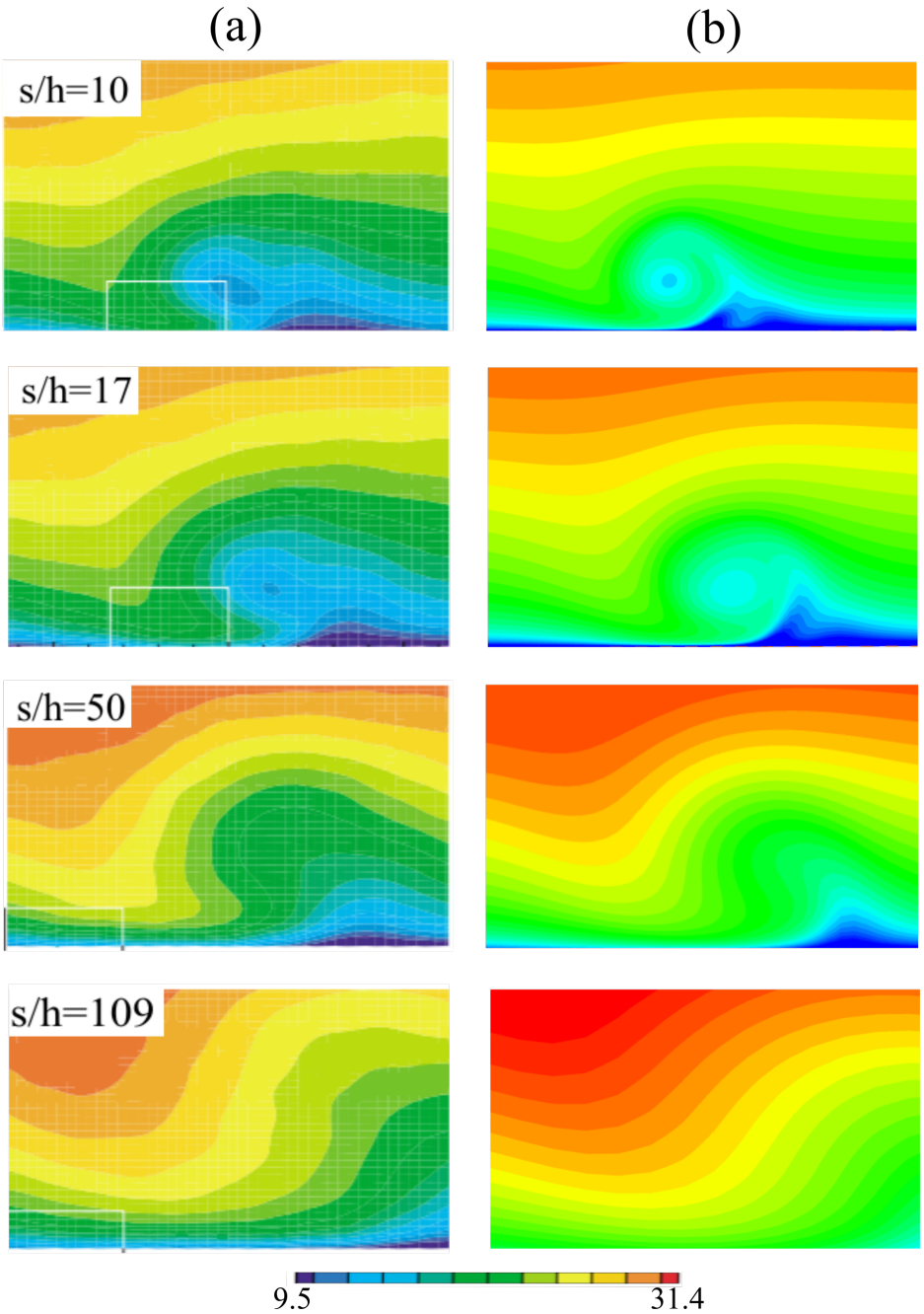


Fig. 5.6 Comparison of streawise velocity at different streamwise stations (a) Experiment [122] (b) RANS.

exactly circular, measurement errors are difficult to avoid. Nevertheless, all show consistent linear increase in the vortex half-life radius nondimensionalized by MVG height.

### 5.4.2 Aerofoil with MVGs

#### Baseline and Mesh Sensitivity

In the clean aerofoil case, the typical feature of its flow field can be seen from a side view of the iso-surfaces of Q colored by velocity magnitude at $Re_c$=1.6 $\times$ $10^5$ as in Figure 5.9. The flow features a laminar separation bubble near the leading edge of the aerofoil, a transition to turbulence immediately after the laminar separation, a flow reattachment of the shear layer and turbulent separation can be seen when the aerofoil is placed at a high angle of attack (AoA).

In order to verify the validity of the study, a baseline of three dimensional NACA 0018 aerofoil was carried out to establish the sensitivity of the simulation to the mesh revolution. Three different meshes with various height of first grid cells near the wall were tested compared to the experimental results of Sheldahl et al. in terms of the time averaged lift and drag coefficient as shown in Table 5.3 [101]. Convergence towards the experimental results is clearly seen as the number of grid cells is increased. The difference in $C_L$ between Mesh 2 and the experimental value is only about 2.0%, while the difference in $C_D$ is 4.1%, Further increase of the mesh size to Mesh 1 yielded a small change and hence Mesh 2 was chosen.

Table 5.3 Comparison of RANS result and experimental data of 3D NACA 0018 aerofoil in terms of lift and drag coefficient, AoA=13°

| | Total Cells | $C_L$ | $C_D$ | $C_L/C_D$ |
|---|---|---|---|---|
| Sheldahl et al.[101] | | 0.950 | 0.0545 | 17.43 |
| Mesh 1 | $8.43 \times 10^6$ | 0.937 | 0.0538 | 17.19 |
| Mesh 2 | $4.79 \times 10^6$ | 0.932 | 0.0524 | 17.78 |
| Mesh 3 | $1.38 \times 10^6$ | 0.911 | 0.0472 | 19.3 |

Figure 5.10 shows the lift and drag coefficients variation with the angle of attack ($\alpha$). As shown in the figure, the lift coefficient of the clean aerofoil from RANS results agrees well with the experiments. For the drag coefficient, the CFD data matches well with the experiment before the stall occurs. After that, the drag coefficient from the numerical result is smaller than the experimental result. This difference is also reported in other studies, which

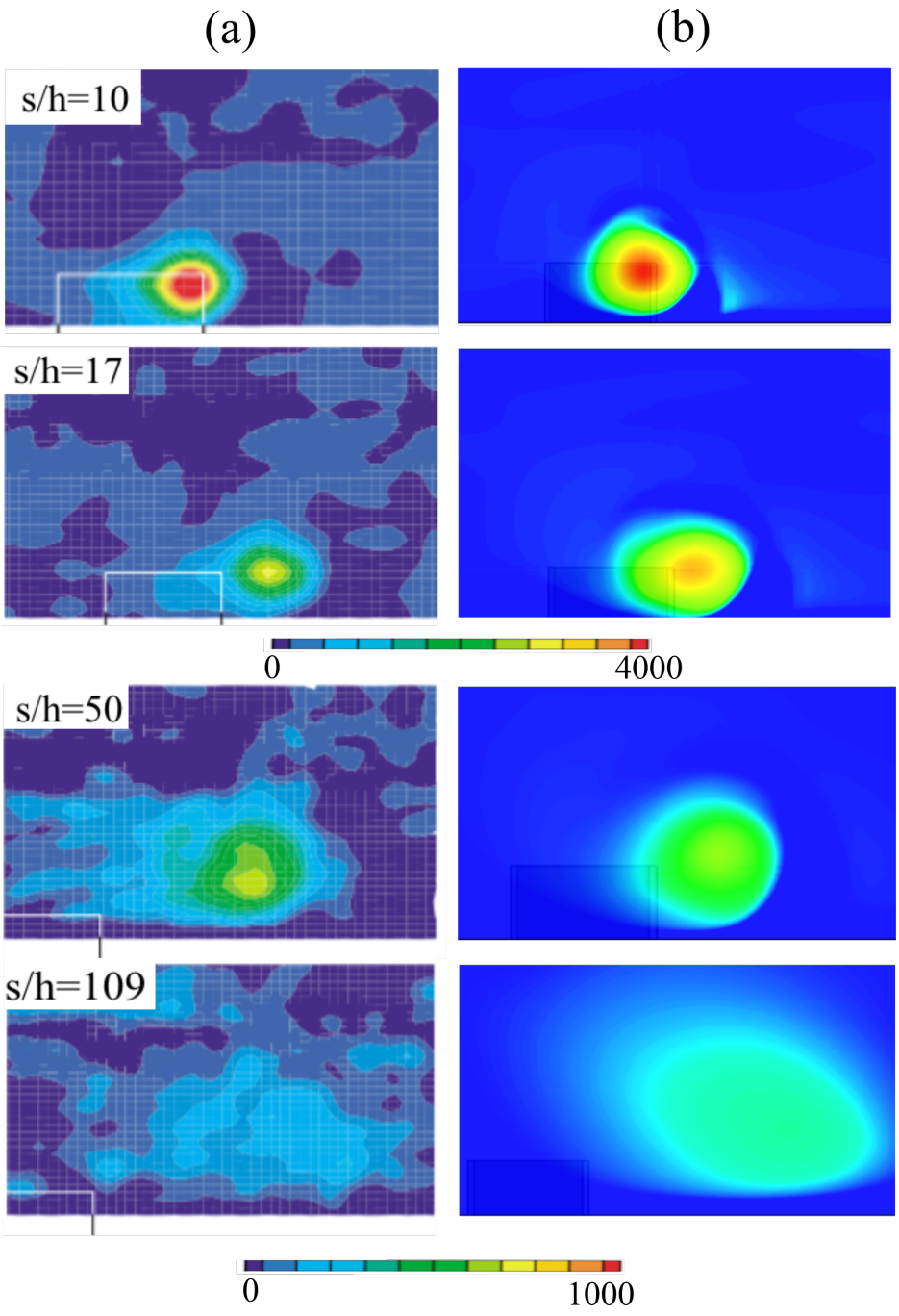


Fig. 5.7 Comparison of streamwise vorticity at different streamwise stations (a) Experiment [122] (b) URANS.

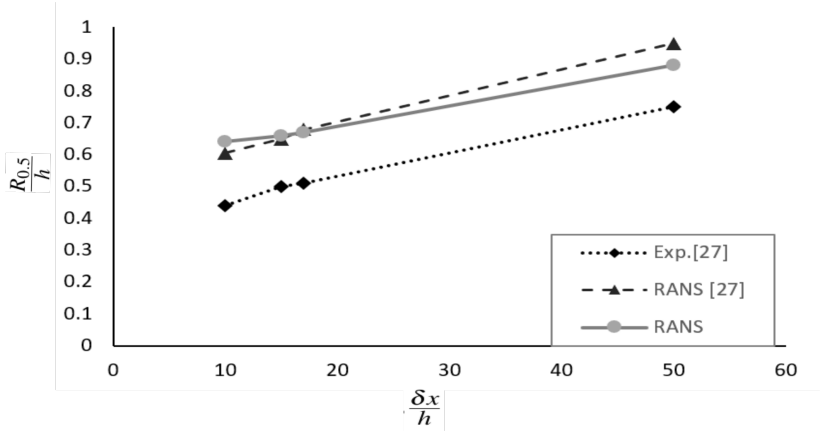


Fig. 5.8 Vortex half-life radius nondimensionalized by device height.

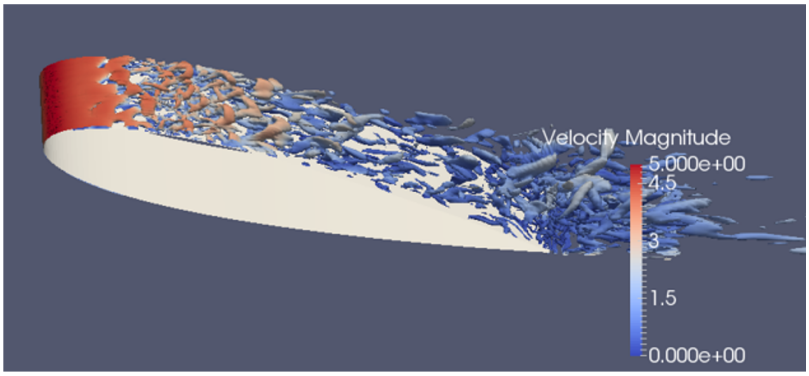


Fig. 5.9 Iso-surfaces of Q colored by velocity magnitude for the case of clean aerofoil NACA 0018, Q=1000, AoA=14°, LES.

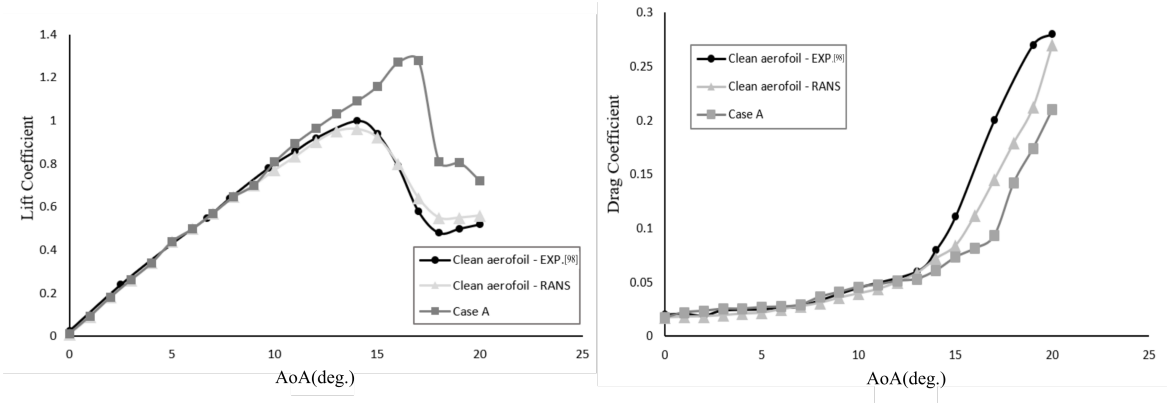


Fig. 5.10 Aerofoil performance at different angles of attack: (a) lift coefficient and (b) drag coefficient, URANS.

is mainly due to the turbulence model limitation for the separated flow. Figure 5.11 indicates a good agreement between numerical result and measured data in terms of lift-to-drag ratio.

In the case with MVGs (case A), it can be seen that the MVGs can improve the aerodynamic performance of the aerofoil significantly. At a very small angle of attack, the lift coefficient of the MVG case is close to that of the clean aerofoil. As the angle of attack increases to around 14°, the stall occurs in the clean aerofoil case with the lift rapidly drops. However, the lift on the aerofoil installed with the MVGs still increases until the angle of attack reached 16.5°. It is evident that the MVGs can increase the stall angle as well as the maximum lift coefficient.

For the drag coefficient, a slightly higher drag is observed in the MVG case as compared to the clean aerofoil before the stall. This is due to the fact that the vortex generator does nothing but to slightly increase the skin drag for the attached boundary layer. As the angle of attack increases beyond the stall angle, it is evident that the drag is significantly less for the aerofoil with MVGs installed. In addition, the positive effects of MVGs can be seen by the lift-to-drag ratio comparison between the cases with and without MVGs in Figure 5.11. At high angles of attack the aerofoil with MVGs has a relatively higher lift-to-drag ratio compared to the clean aerofoil case, but there is a small price to pay at low angles.

Figure 5.12 shows a comparison of the mean value of pressure coefficient ($C_p$) at AoA=15° for the aerofoil with and without MVGs. As can be seen from the figure, $C_p$ on the suction surface of the aerofoil is improved after adding the MVGs. As the result, the pressure difference between the suction and pressure surface of the aerofoil is increased, leading to the higher lift.

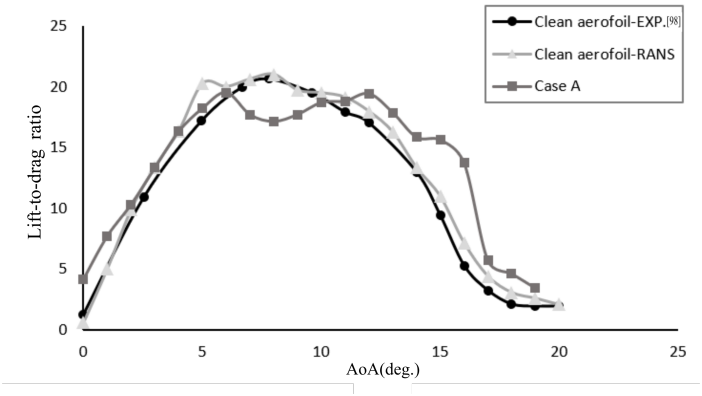


Fig. 5.11 Lift–to-drag ratio comparison between aerofoils with and without MVGs, URANS.

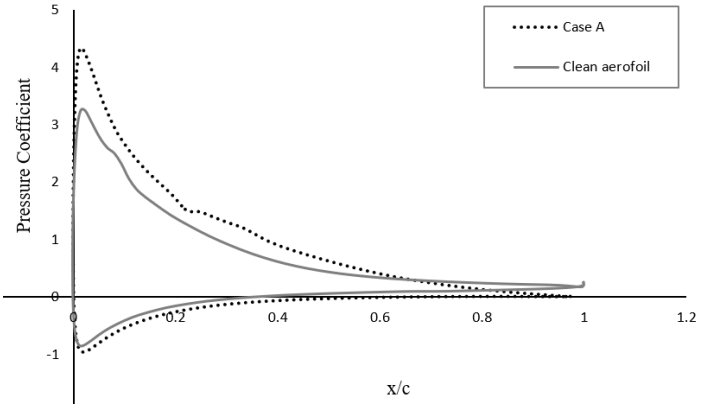


Fig. 5.12 Pressure coefficient comparison between aerofoils with and without MVGs, AoA=15°, URANS.

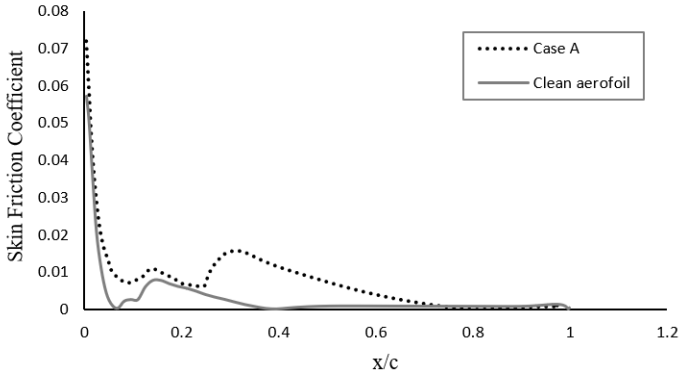


Fig. 5.13 Skin friction coefficient distribution on NACA 0018, AoA=15°, URANS.

Wall shear stress is a useful parameter to assess the effect that the vortices have on the near-wall boundary layer. Figure 5.13 presents a comparison of the skin friction coefficient along the upper surface of aerofoils with and without MVGs at a high angle of attack 15°. The solid line shows the $C_f$ distribution of the clean aerofoil. $C_f$ drops sharply near the leading edge at about 5% chord length caused by the small leading-edge bubble. The value of $C_f$ increases, as the flow reattaches. Further downstream a turning point appears at about 15% chord length of aerofoil where $C_f$ starts decreasing again leading to very low values at $x > 0.4c$ due to massive flow separation.

The dashed line in Figure 5.13 stands for the aerofoil of case A. Near the trailing edge of the aerofoil, the trend of $C_f$ distribution of case A is close to the clean aerofoil. However, there is a sudden rise in $C_f$ at 25% chord length just downstream of the MVGs. Further downstream $C_f$ increases again due to the flow transition from laminar to turbulence and reattachment.

As momentum is introduced into boundary layer by the MVGs, the distribution of the skin friction along the surface changes significantly. Figure 5.14 shows the skin friction at s/h = 3, 5, 10 and 30 behind the MVGs where s stands for the distance to the trailing edge of the MVGs and h is the height of MVGs. With MVGs on the aerofoil, a larger variation of skin friction is observed at s/h=3 compared to a clean aerofoil. The increased level of skin friction is an indication of a healthier boundary layer with no intention to separate. They can improve the skin friction on the wall surface of an aerofoil, which agrees well with other results [122]. This improvement was induced by the vortices behind the MVGs. Along the spanwise direction, the skin friction decreases with the increase of distance from MVGs. Along the chord line direction, skin friction near the MVGs is relatively higher than that farther from MVGs because of the diffusion of vortices.

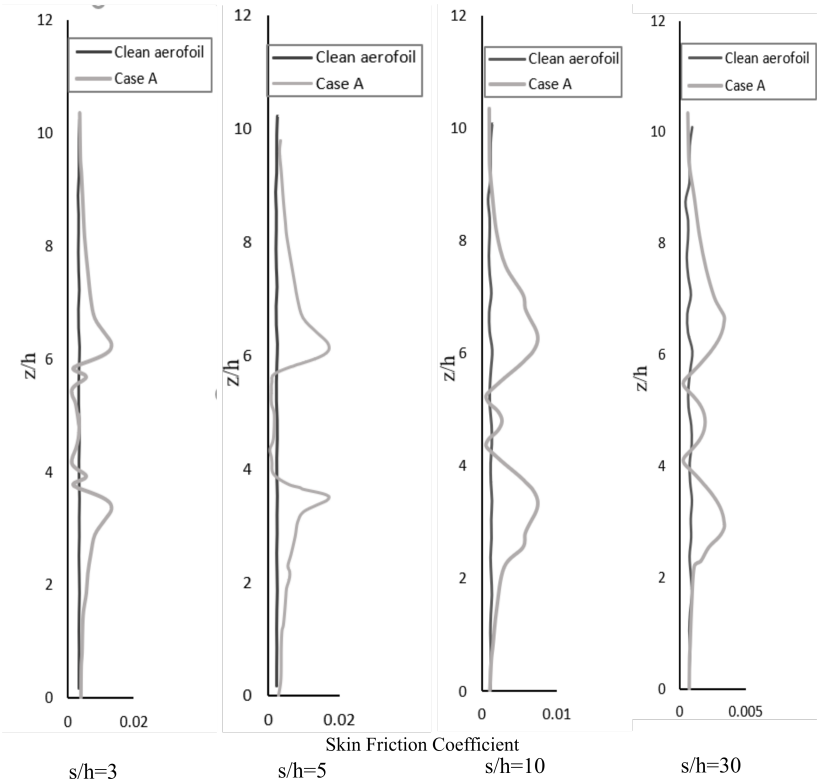


Fig. 5.14 Skin friction coefficient distribution at different points on aerofoil surface, RANS. s stands for the distance to the trailing edge of MVGs. h is the height of MVGs and z is the coordinates in Z direction, URANS.

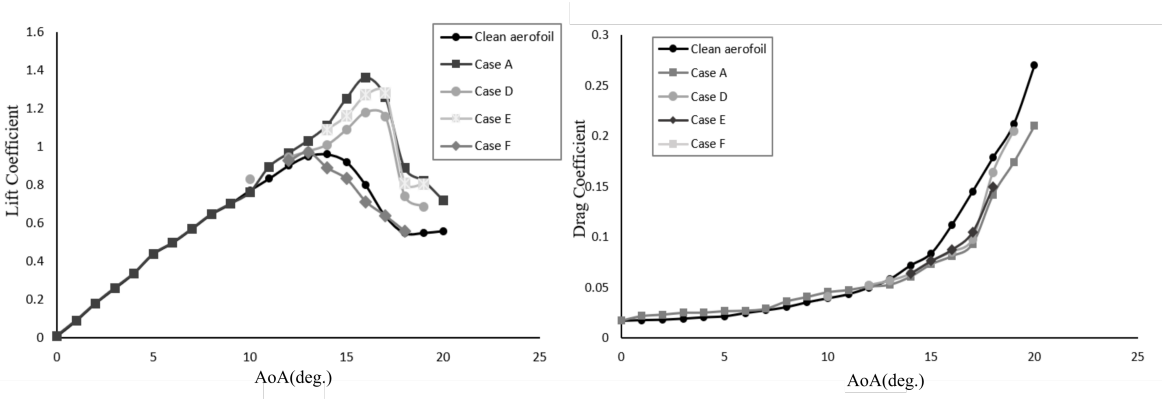


Fig. 5.15 lift and drag coefficient comparison of different cases, URANS.

MVGs with a proper configuration can have a positive effect on the aerodynamic performance of a NACA 0018 aerofoil. In order to optimize the MVG configuration for a better performance, a comprehensive understanding of the influence of several parameters related to MVGs is important, such as the location, mounting angle, length, shape and array configurations.

**Effect of location on the performance of MVGs**

Many researchers have shown that the location of MVGs influences the capability of controlling flow separation. It was found that MVGs located at 15% to 30% of the chord length could improve the aerodynamic performance of the aerofoil. In the present work, besides case A with MVGs located at 20% chord length, three other cases were studied, in which the MVGs were located at 15%, 22% and 25% chord length. The lift and drag coefficients versus the angle of attack for these cases are given in Figure 5.15. The clean aerofoil case is also superimposed. Compared to the clean aerofoil case, cases A, D and E have significantly improved the lift near the stall angles of attack, especially in the case E, where the maximum lift has been improved by 25%. However, the MVGs in case F, which are located at 25% chord length of the aerofoil, have a negative effect on other aspects of aerodynamic performance. The stall angle and the lift after the stall have also been reduced. For the drag, all the cases with MVGs have a similar trend as discussed in the last section. Compared to the clean aerofoil, all four configurations with MVGs have a mildly higher drag at lower angle of attack. However, after the aerofoil stalled, a lower drag is observed in the MVGs cases. Among the cases tested, case A has the best overall performance where the highest lift and the lowest drag are observed.

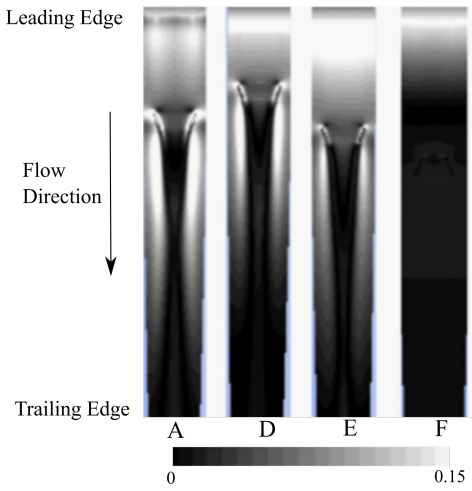


Fig. 5.16 Skin friction coefficient contours on the aerofoil surface on the suction side, AoA=15°.

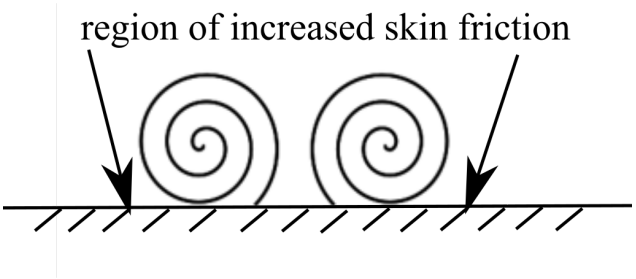


Fig. 5.17 schematic view of one pair of vortices behind MVGs.

The contours of skin friction on the suction side are shown in Figure 5.16, where MVGs are installed in three different streamwise locations. The flow direction and the position of leading edge of the aerofoil are present in the figure. Compared to the clean aerofoil case, the MVGs increase the skin friction which indicates a healthier boundary layer. There is a region of high skin friction in cases A, D and E due to the generation of a pair of counter-rotating vortices behind the trailing edge of MVGs, see Figure 5.17 for illustration. This improvement is most evident in case A, where the MVGs are located at 20% chord length; whereas in case E, where the MVGs are located at 22% chord length, there is no noticeable region of high skin friction behind MVGs.

A strong variation of the skin friction in the spanwise direction can be observed in Figure 5.14. To examine this variation, Figure 5.18 plots the skin coefficient for all the cases with MVGs installed. The data at the station downstream of the MVGs at s/h=5 is extracted. It is evident that the skin coefficient for the case A is highest among all the cases, which indicates that the strongest vortex is generated in case A.

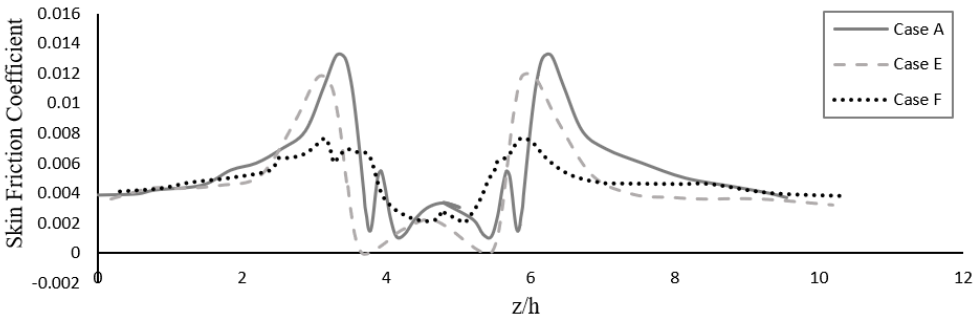


Fig. 5.18 Skin friction selected streamwise section, .x/h =5, AoA=15°, URANS.

Figure 5.19 shows the comparison of streamlines with and without MVGs at different locations at the angles of attack of 15°. From the clean aerofoil, the separation occurs at around half of chord length, pointing to a stall of the trailing edge separation process. In case D, where the MVGs are installed at 15% chord length, there is a small separation bubble near the trailing edge on the suction side of aerofoil. When the MVG moves to the location of 20% chord length in case A, the flow stays attached over the whole suction side of the aerofoil. The MVGs in case E and case F are located 22% and 25% of the chord length respectively. It is clear that in case F the area of the separation region significantly increases in the aft-portion of the chord, with the size of the trailing edge separation bubble being the largest.

**Effect of mounting angle on the performance of MVGs**

Apart from the location, the mounting angle is also of great importance for the performance of MVGs. The MVGs of a larger mounting angle introduce more energy into the boundary layer. However, they may introduce higher drag at smaller angle of attack, which may offset the benefit of the separation control. As a result, finding an optimal mounting angle to balance the lift and drag increases is essential.

The comparison of the lift and drag for the aerofoils with MVGs mounted at three different angles is shown in Figure 5.20. Like other cases discussed above, MVGs have no visible effect on the lift at small angles of attack, while the drag is slightly increased. The lift coefficient continues to increase and peaks at 1.3 in cases A and B, while the clean aerofoil has already stalled. The drag in case A follows the same trend with case B, which is slightly smaller than the clean aerofoil after stall angle.

As discussed before, the suppression of the separation bubble by the MVGs can be shown by the contours of the skin friction on the suction surface of the aerofoil, which are shown

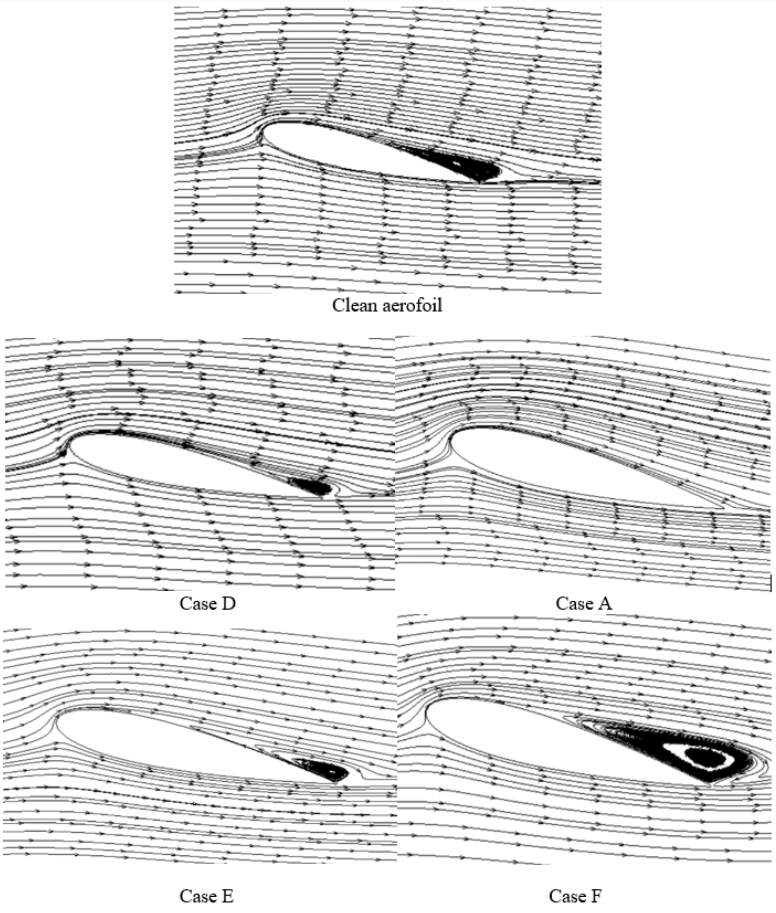


Fig. 5.19 Streamlines around aerofoils with different MVGs at the mid-span, AoA=15°, URANS.

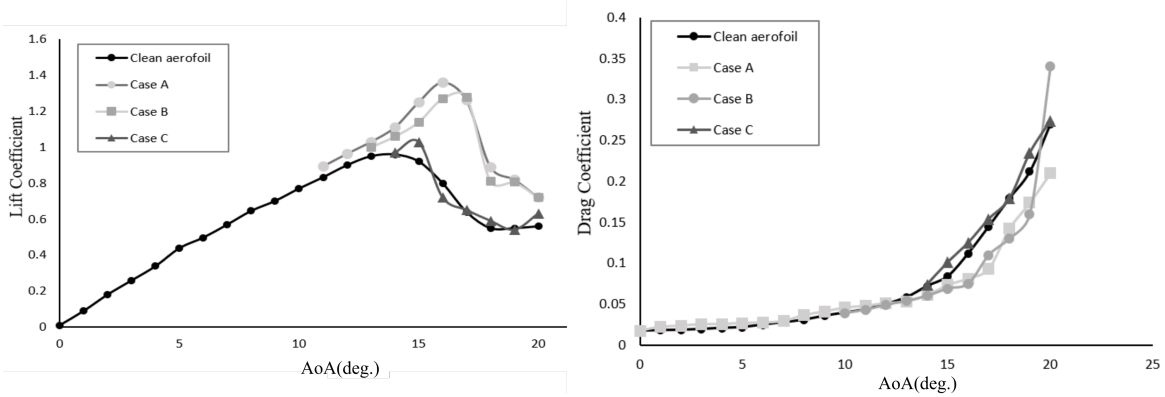


Fig. 5.20 lift (right) and drag (left) coefficient comparison of different cases, URANS.

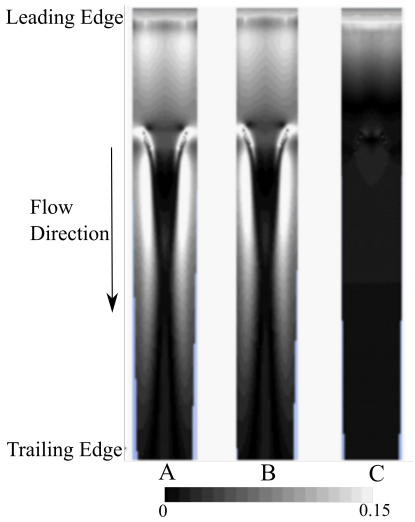


Fig. 5.21 Skin friction coefficient contours on the aerofoil surface on the suction side. AoA=15°, URANS.

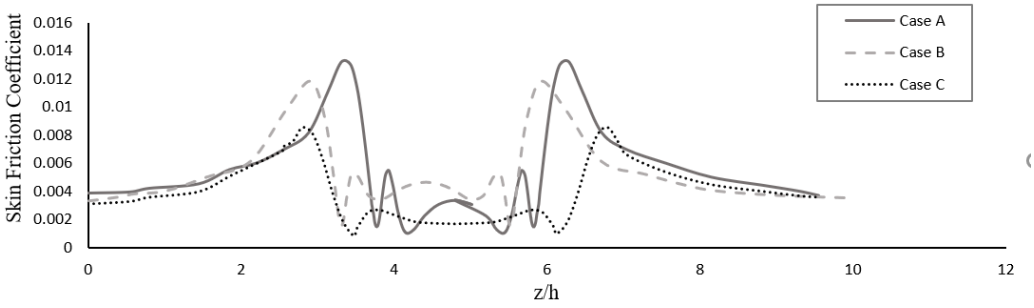


Fig. 5.22 Skin friction selected streamwise section, s/h =4, AoA=15°, URANS.

in Figure 5.21. The spanwise distribution of the skin friction coefficient is shown in Figure 5.22 at s/h =4. The skin friction coefficient is extracted from the location s m downstream the MVGs. The skin friction increase can be observed both in case A and B, but not in case C. Figure 5.21 shows the contour of skin friction coefficient distribution. There is a region of high skin friction downstream of the MVGs in these two cases, which corresponds to the result of the lift enhancement showed in Figure 5.20. However, in case C, as the mounting angle of the MVGs is too high, the counter rotating vortex is not strong enough to suppress the separation bubble, and thus, the skin coefficient is similar to that of the clean aerofoil case.

The effectiveness of MVGs in suppressing the separation bubble is also shown in Figure 5.23, which compares the streamlines around the aerofoils for the cases with MVGs of different mounting angles. The inflow angle of attack is again at 15°. In case B where the MVGs are mounted at an angle of 19° to the free stream, there is a relatively small vortex near

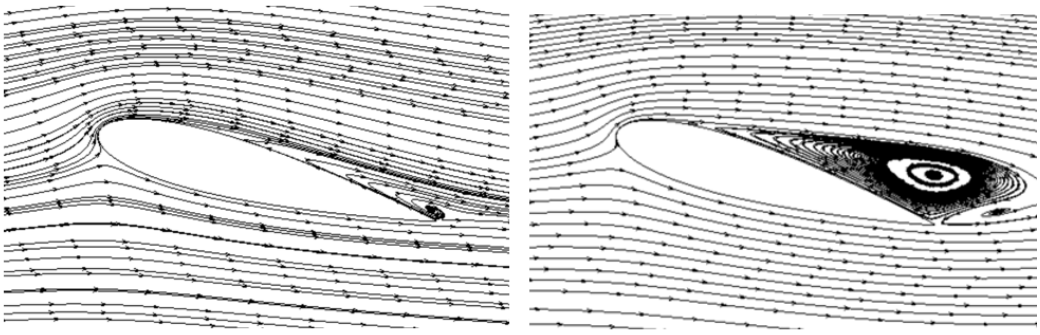


Fig. 5.23 Comparison of streamlines around aerofoils with different MVGs at the mid-span, AoA=15°, URANS.

the trailing edge compared to case B, in which the MVG is installed at 22°. These results can also be compared to case A in Figure 5.19, in which the MVGs are effective in introducing the momentum from the outside to the inside of the boundary layer, and eventually suppress the flow separation. It is shown that with an increase of the mounting angle from 16° to 22°, the effectiveness of MVGs decreases. In addition, when the mounting angle reaches 22°, the MVGs start to degrade the performance of aerofoil. A larger separation bubble is observed compared to the clean aerofoil case.

### MVGs of different shapes

Apart from the location and mounting angle of the MVGs, the vane can also have various shapes, such as rectangle, triangle, trapezoid and so on. Two commonly used shapes are the rectangle and the triangle as studied here. The discussion in this section is centered at the angle of attack of 14°. Table 5.4 shows the effect of the shape of MVGs on the lift and drag of the aerofoil at $\alpha = 15°$. The MVGs in cases A and G have the same height and length. It was found that both MVGs improved the lift and reduced the drag compared to the clean aerofoil. The aerofoil in case A has relatively higher lift compared to case G, while the drag is higher as well for case A. This result in a similar lift-to-drag ratio in these two cases.

Table 5.4 Comparison of drag and lift of aerofoils for different MVGs, AoA=15°

| | $C_L$ | $C_D$ | $C_L/C_D$ |
|---|---|---|---|
| Clean Aerofoil | 0.93 | 0.084 | 11.07 |
| Case A (rectangular MVGs ) | 1.17 | 0.075 | 15.60 |
| Case G (tritangular MVGs ) | 1.09 | 0.071 | 15.35 |

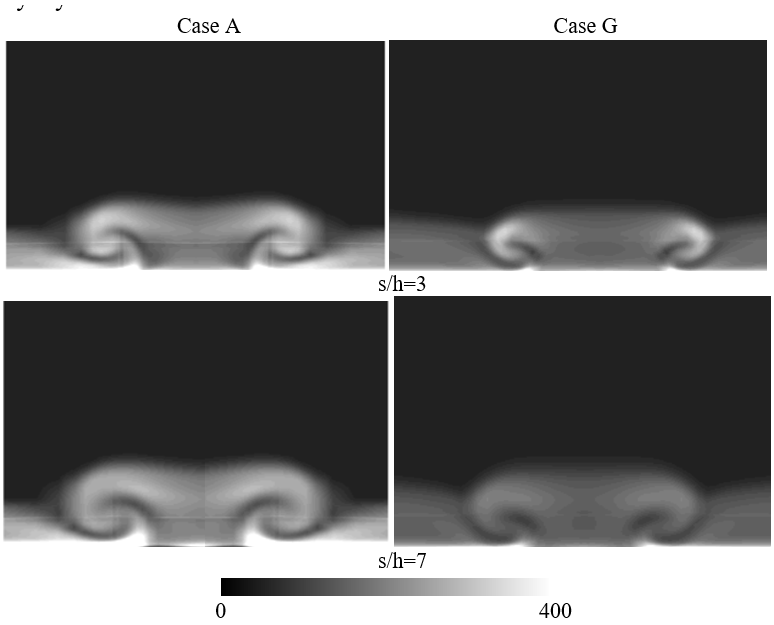


Fig. 5.24 Vortcity magnitude contours at different streamwise stations downstream MVGs, AoA=15º, URANS.

The comparison between Case A and Case G for the vorticity magnitude is shown in Figure 5.24 for the downstream slices at s/h=3 and s/h=7. As indicated by the figure, the size and magnitude of the vortex generated in Case A are larger in both downstream slices, which means rectangular MVGs are more effective in vortex generation compared to the triangular ones that have smaller surface to generate the vorticity. Similar result can be found by Fouatih et al. [30]. In their study, the performance of the rectangular and triangular MVGs of the same height located at 0.3c with the mounting angle of 10° were tested and compared on a NACA 4415 airfoil. It was found that at AoA=18°, the rectangular MVGs improve the lift coefficient of the base line to 1.54, while the value for the triangular MVGs was 1.48. However, the drag coefficient for the aerofoil with rectangular MVGs was slight larger than that of the aerofoil with triangular MVGs. Zhen et al. also found that rectangular VG performed better than triangular VG [128].

As the vortex convects downstream to slice s/h=7, the size of the vortex is still larger in case A. Figure 5.25 shows the contours of the skin friction on the suction surface of the aerofoils in cases A and G. Though the rectangular MVGs in case A and triangular MVG in case G have the same height and mounting angle, the area of high skin friction behind the MVGs in case G is much smaller than that in case A. This indicates a weaker vortex and therefore a weaker momentum transfer between the mainstream and the boundary layer.

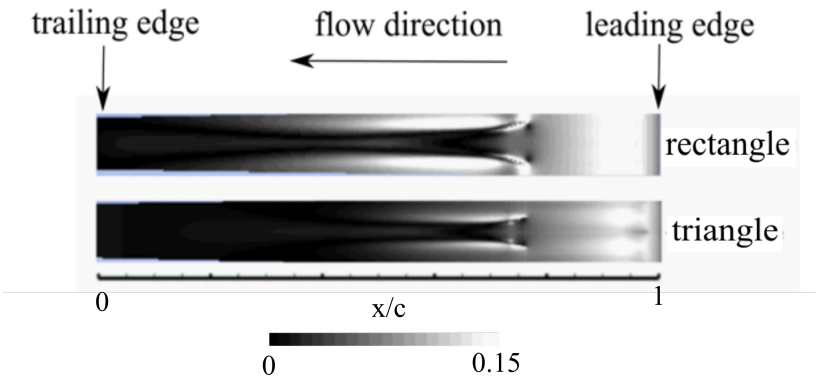


Fig. 5.25 Skin friction coefficient contours on the aerofoil surface on the suction side, AoA=15°, URANS.

The velocity contour around the aerofoils at the angle of attack of 15° is revealed in Figure 5.26. As we can see in this figure, the boundary layer on the suction surface separates near the leading edge without MVGs installed. However, for the cases with MVGs, the separation location moves further downstream. The width of the wake is also reduced by adding MVGs and this reduction is more obvious in case A with the rectangular MVGs as compared to the triangular MVGs in case G. This is because the vortex generated by the triangular MVGs is not as strong and large as that by the rectangular ones.

### The length of MVGs

The length of the MVGs can also change the performance, and this is investigated in this section. In case H, the MVGs' length is e/h=6, where e is the length of MVGs, which is twice as that in case A. Table 5.5 shows a comparison of lift and drag of the aerofoils. As can be seen in the table, at $\alpha = 15°$, the length has limited influence on the effectiveness of MVGs, as the lift and drag stay almost the same when its length is increased. When the angle of attack reaches 16°, although both the lift and drag in case H are larger than that in case A, the increase of the drag is relatively more profound than the increase of the lift. Hence, the lift-to-drag ratio reduces with a longer MVG. This suggests that the increase in drag offsets the benefit of an increased lift for a longer MVGs.

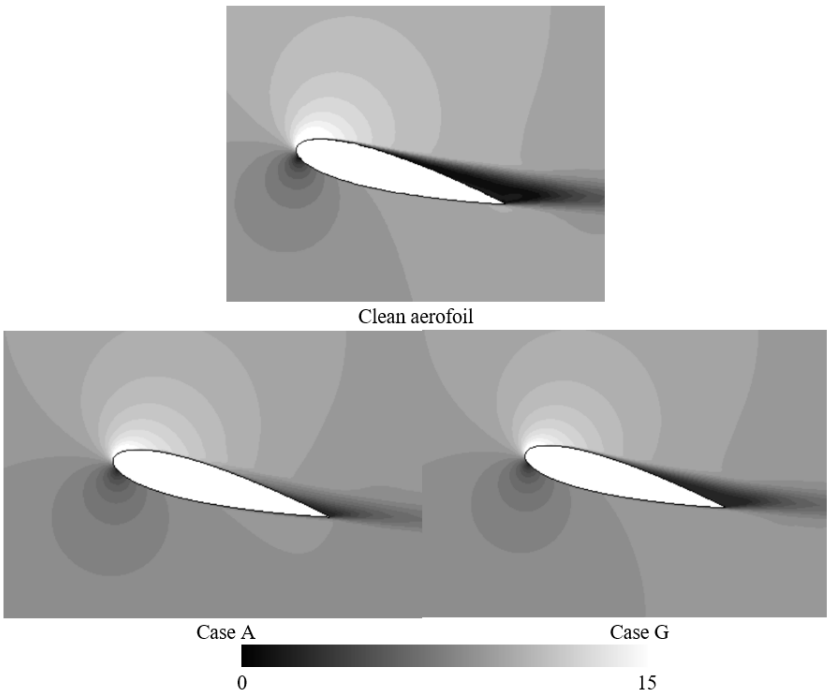


Fig. 5.26 Comparison of velocity contours at spanwise slices midway between clean aerofoil and aerofoils with MVGs, AoA=15°, URANS.

Table 5.5 Comparison drag and lift for aerofoils with different MVGs

| | AoA=15° | | | AoA=16° | | |
|---|---|---|---|---|---|---|
| | $C_L$ | $C_D$ | $C_L/C_D$ | $C_L$ | $C_D$ | $C_L/C_D$ |
| Clean Aerofoil | 0.93 | 0.084 | 11.07 | 0.80 | 0.112 | 7.14 |
| Case A (rectangular MVGs ) | 1.17 | 0.075 | 15.60 | 0.81 | 0.0813 | 9.96 |
| Case G (tritangular MVGs ) | 1.09 | 0.071 | 15.35 | 0.824 | 0.105 | 7.84 |

### 5.4.3 VAWT with MVGs

#### 3D mesh sensitivity analysis

After understanding the aerodynamic performance of micro-vortex generators on an aerofoil, the effectiveness of MVGs installed on a vertical axis wind turbine is assessed in this section. The best performing MVGs studied in the previous section are selected for the wind turbine investigation. Here, large eddy simulations are performed to understand the details of the flow dynamics around the turbine blades as well as the mechanism of MVGs on improving the turbine efficiency. The length of the blade is 50% of chord length of aerofoil. To reduce the computational cost of the large eddy simulation, the tip effect is not considered. A periodic boundary condition is imposed in the spanwise direction.

The mesh sensitivity analysis has been conducted to assess the mesh quality for the LES for the flow field prediction. The 3D mesh independence study was performed only for the unmodified turbine as the base case. The power coefficient of the base case based on three grids (Mesh 4, 5 and 6) is shown in Table 5.6. The wall distance for all the three grids is $3.5 \times 10^{-5}$, resulting in $y^+ < 2$. All the simulated results over estimate the power coefficient of the turbine compared to the experimental result by Balduzzi et al. [8]. Among them Mesh 4 offers the least difference with measured data. However, the discrepancy between Mesh 4 and Mesh 5 is minor, only 2.6%. Therefore, Mesh 5 is adopted considering its reduced computational resources. The moment coefficient of one blade of the turbine is compared in Figure 5.27. There is no obvious difference between Mesh 4 and Mesh 5.

Table 5.6 Comparison drag and lift for aerofoils with different MVGs

| | Total Cells | TSR | Power Coefficient |
|---|---|---|---|
| Balduzzi et al.[8] | | 2.1 | 0.218 |
| Mesh 4 | $4.92 \times 10^7$ | 2.1 | 0.228 |
| Mesh 5 | $3.59 \times 10^7$ | 2.1 | 0.234 |
| Mesh 6 | $1.76 \times 10^7$ | 2.1 | 0.263 |

The LES results of an H-type blade turbine without MVGs are compared to the results available in the literature. Figure 5.28 shows the comparison of the measured data and the CFD results in terms of power coefficient versus tip speed ratio. The rotors in the current study are the same as in the experiment and CFD in [8].

In order to setup the time step for three-dimensional simulation and assess how it affects the results, a time-step sensitivity analysis was performed. Three different values of time

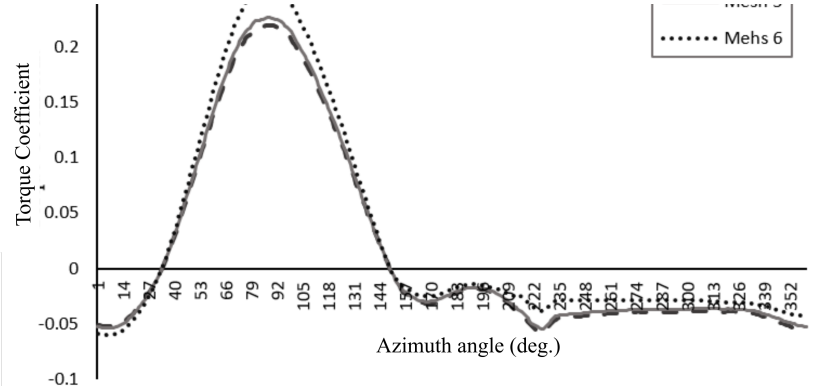


Fig. 5.27 Moment coefficient of one blade in one revolusion of the VAWT for different meshes.

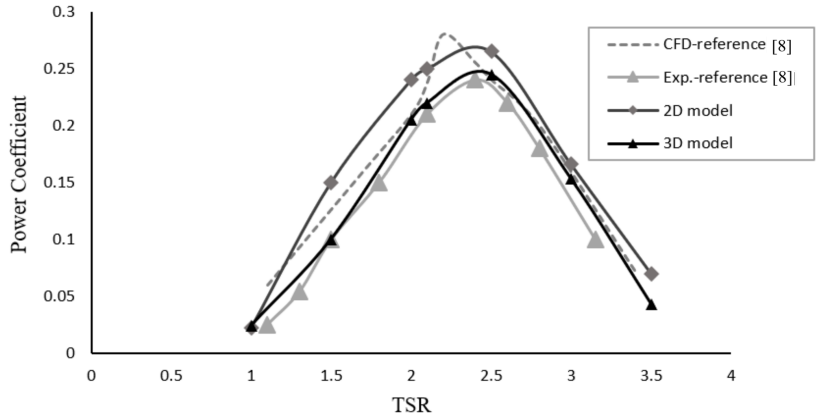


Fig. 5.28 Power coefficient comparison between experiment and CFD results, LES.

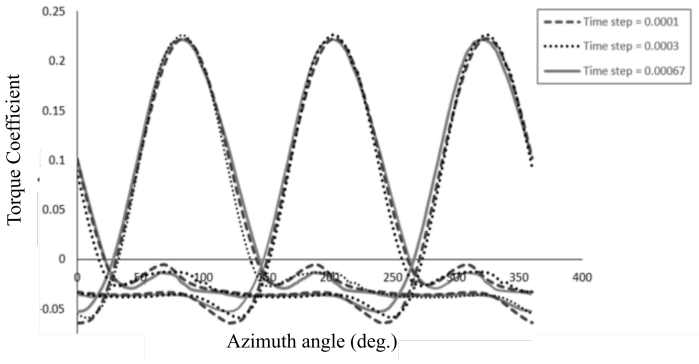


Fig. 5.29 Torque coefficient of the three blades for different time step sizes, TSR=2.5, LES.

step were chosen for testing. They are $\Delta t$ =1e-4s, 3e-4s, 6.7e-4s, where one time period of the turbine rotation is 0.33s at TSR=2. The moment coefficient with different time steps was investigated as in Figure 5.29. It was found that the result of $\Delta t$ =6.7e-4s agrees well with a smaller time step, thus the time step step size of 6.7e-4s is used to keep the computational cost to a feasible level.

For the lift-based turbines, the angle of attack variation for one cycle should be investigated as it has a great influence on the lift generation. Figure 5.30 depicts the variation of angle of attack at different rotor blade azimuth angles and for different tip speed ratios over a full cycle. The maximum angle of attack decreases as the TSR increases. At low TSRs, VAWTs encounter a wide range of angles of attack as shown in Figure 5.29. As the static stall angle of aerofoil NACA 0018 at $Re_c = 1.6 \times 10^5$ is $14^\circ$ . It is clearly found that for the lower TSR, the turbine blades experience a larger part of azimuth angles that exceeds the static stall angle in one revolution. At TSR=1.5, during most of the revolution the blade is in deep stall condition.

Figure 5.31 shows the lift and drag variations for a wide range of angles of attack (AoA) from $0^\circ$ to $40^\circ$. This range covers the AoA that turbine blades encounter in one revolution at $Re = 1.6 \times 10^5$. The effect of MVGs for the aerofoil around the stall angle has been already discussed in detail. The lift drops significantly after the stall angle and then slightly increases with the increasing of AoA. It is clear that at AoA from $28^\circ$ to $40^\circ$ , the lift of a clean aerofoil is slightly higher that the aerofoil with MVGs. On the other hand, the MVGs have no visible influence on the drag of the aerofoil as shown in Figure 5.31(right) for those high AoAs. This can be explained by the fact that the MVGs are inside the massive flow separation region of the stall and cannot function as intended, i.e. inject fresh air from the outer boundary layer to the inner one.

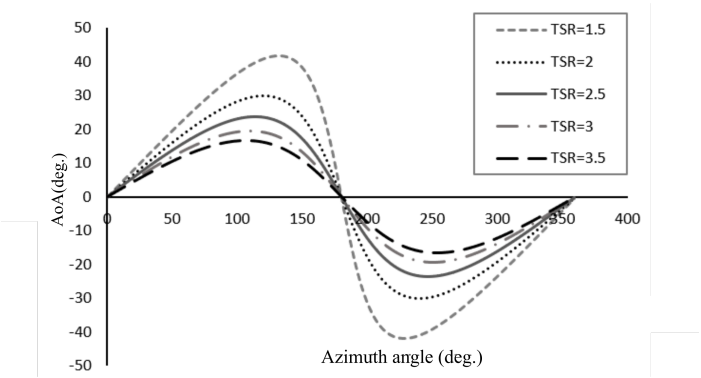


Fig. 5.30 Angle of attack (AoA) variation in one revolution at various TSRs.

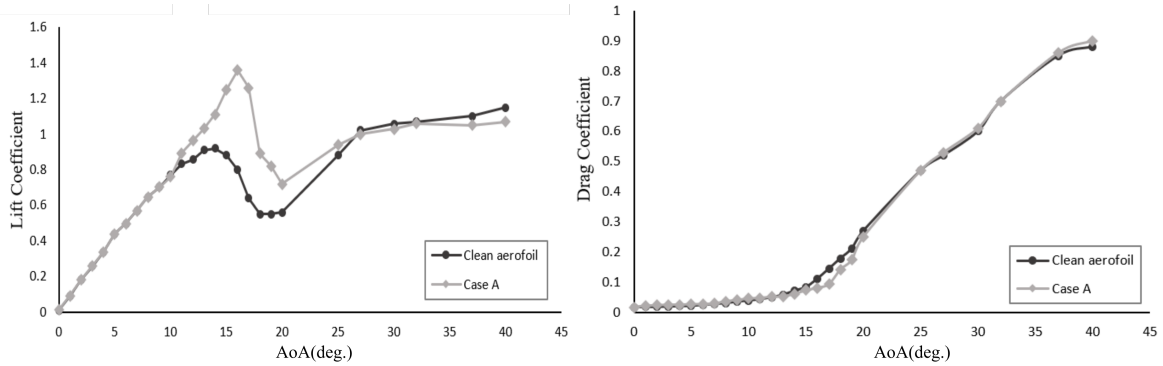


Fig. 5.31 Lift (right) and drag (left) comparison for clean aerofoil and aerofoil with MVGs A, URANS.

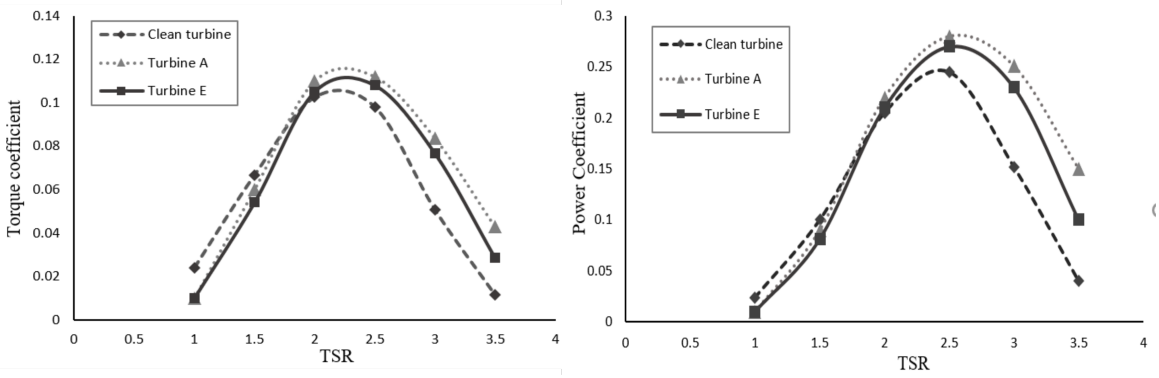


Fig. 5.32 Variations of the moment coefficient and power coefficient as functions of azimuth angle for one blade of various MVGs, LES.

**Effect of location for the performance of MVGs**

The function of MVGs A and E on the turbines is investigated in this section as these two configurations of MVGs were found to be the most effective in improving the aerodynamic performance of a single aerofoil. The torque and the power curves of the clean VAWT and VAWTs with rectangle MVGs of the two locations at the wind speed of 8 m/s are presented in Figure 5.32. All the performance curves start at a lower value and peaking before dropping to a lower value again. The results were computed with LES. As we can see in this figure, the effect of the MVGs on the performance of a VAWT varies with the TSR. At low TSRs, from 1 to 2, the VAWT with and without MVGs have a similar performance. This is because at low TSRs, the turbine blades are considerably at post stall condition during most of the part of the turbine rotation cycle as discussed in the last section. As the MVGs have nearly no effect at angles of attack much higher than the stall angle, their effect was limited on the performance of turbines at low TSRs. When the TSR is larger than 2, adding MVGs with a suitable configuration gives improvement of performance. Compared to other cases, the MVGs located at 20% chord length of the blade's profile give the best performance at TSR=2.5 and 3. This is consistent with the observation made for the single aerofoil.

In order to understand the mechanism of the efficiency improvement due to MVGs, the phase-averaged moment coefficient of one blade for one rotation cycle VAWTs is presented in Figure 5.33. It is evident that most of the wind energy is captured in the first half cycle. For the second half cycle, the torque coefficient $C_m$ of all turbines is low due to the fact that the blade is traveling within the wake of the upstream blade. The main differences of Cm are at the first half cycle where the azimuth angle $\theta$ ranges between 75° and 160° , and hence the

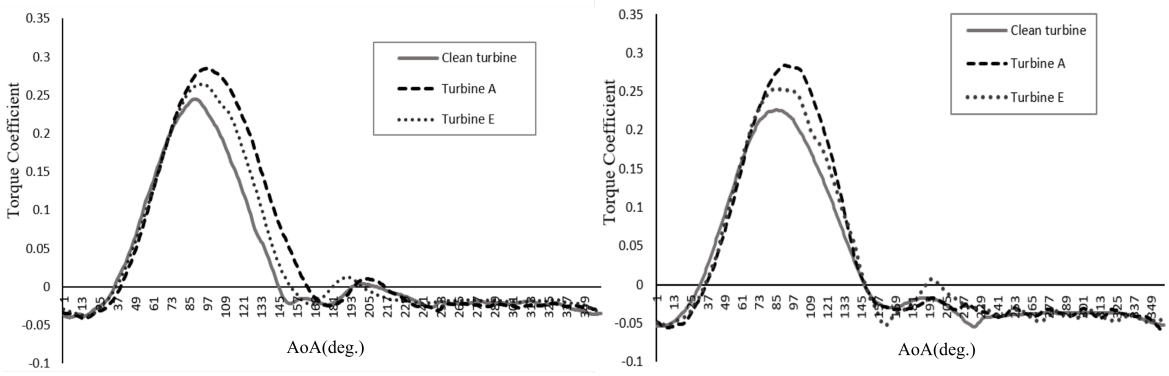


Fig. 5.33 Blade phase-averaged moment coefficient comparison of various turbines TSR=2.5 (left) TSR=3 (right), LES.

flow separation appears because of the relatively large AoA the blades encounter as shown in Figure 5.30.

At low azimuth angles from 0° to 80°, the $C_m$ of all cases follows a similar trend: the moment coefficient increases as the azimuth angle rises. This is because the lift increases with the AoA before stall occurs. When the azimuth angle increases to 80°, where AoA=14°at TSR=2.5, the rotor blades start to stall and the moment coefficient begins to decline from its peak value. The maximum $C_m$ and the azimuth locations of the peak value vary in different cases.

As shown in Figure 5.33 (left), when the azimuth angle increases to around 80°, the moment coefficient of the clean turbine reaches its peak value of 0.237 and starts to decline. However, for other cases, the moment coefficient continues to rise. With the increase of azimuth angle, $C_m$of turbine A is the last one to reach its peak value as compared to other cases, for both TSRs of Figure 5.33. In addition, a maximum value of $C_m$ is observed in turbine A. Compared to the clean turbine, we can conclude that MVGs can improve the performance of VAWTs, and the results are consistent to that of an isolated aerofoil discussed in the last section. A similar result at TSR=3 is shown in Figure 5.33 (right), turbines A and E produce more power output at the first half of the cycle after stall as compared to the clean turbine.

On the second half of the cycle, the angle of attack is negative as shown in Figure 5.30, which leads to the MVGs being the pressure side of the aerofoil instead of the suction side. Hence, the MVGs have no effect on the flow separation and no noticeable difference between the clean turbine and the turbines equipped with MVGs is observed.

The overall moment, which combines all the three blades is another parameter that can be used to evaluate the turbine performance. Figure 5.34 plots the variation of the overall

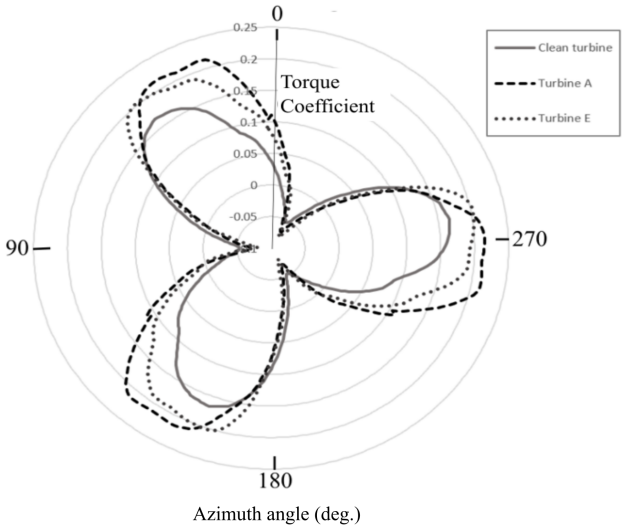


Fig. 5.34 Moment coefficient variation with azimuth angle clean turbine and turbine A and E, TSR=3, LES.

phase-averaged moment coefficient of various turbines over a full operational cycle at TSR=3. All the cases show a similar trend and turbine A offers the maximum value of moment coefficient, which is consistent with the previous analysis.

Figure 5.35 shows the contour of the vorticity magnitude around the blade profile of different turbines at TSR=2.5. The MVGs offer a dramatic change in the pressure distribution on the suction side of the aerofoil. At an azimuth angle of $\theta = 120^{\circ}$, the profile exceeds the stall angle and mild separation starts to occur in the boundary layer of the clean turbine. Two spanwise vorticity rolls can be observed: one originated from the leading-edge separation and the other separation occurs near the trailing edge. The separation point in turbine A is farther away from the leading edge of the aerofoil compared to the clean turbine case and is consistent to a higher lift and torque generation. In turbine E, the flow separation on the suction side of blade is weaker compared to the clean turbine as well.

Figure 5.36 shows a similar result at TSR=3. When the turbine blade rotates to $\theta = 130^{\circ}$, the flow separation of the clean turbine is more profound as compared to the turbines with MVGs A and E again pointing to the benefits of the MVGs on delaying flow separation.

The static pressure field is shown in Figure 5.37 for a blade aerofoil section at $\theta = 90^{\circ}$. As we can see in this figure, this qualitative comparison shows some significant differences in the pressure distribution of the various turbines. The area of the region with a low pressure on the suction side of turbine blade is larger for turbine A and turbine E than the clean turbine. This corresponds to a larger pressure difference, leading to a larger moment generation at

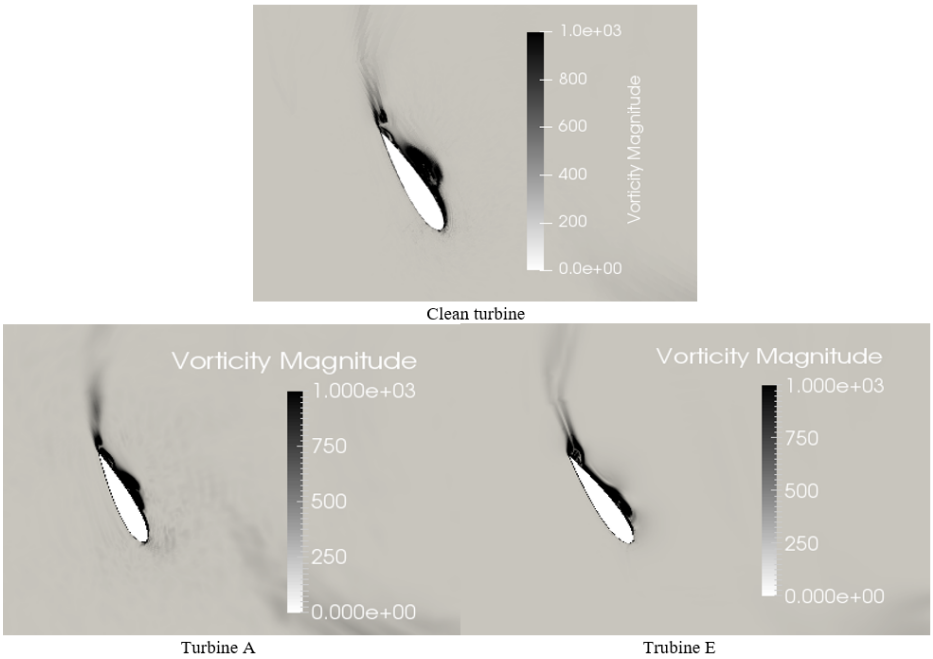


Fig. 5.35 Vorticity magnitude comparison of various turbines at $\theta = 120°$, TSR=2.5, LES.

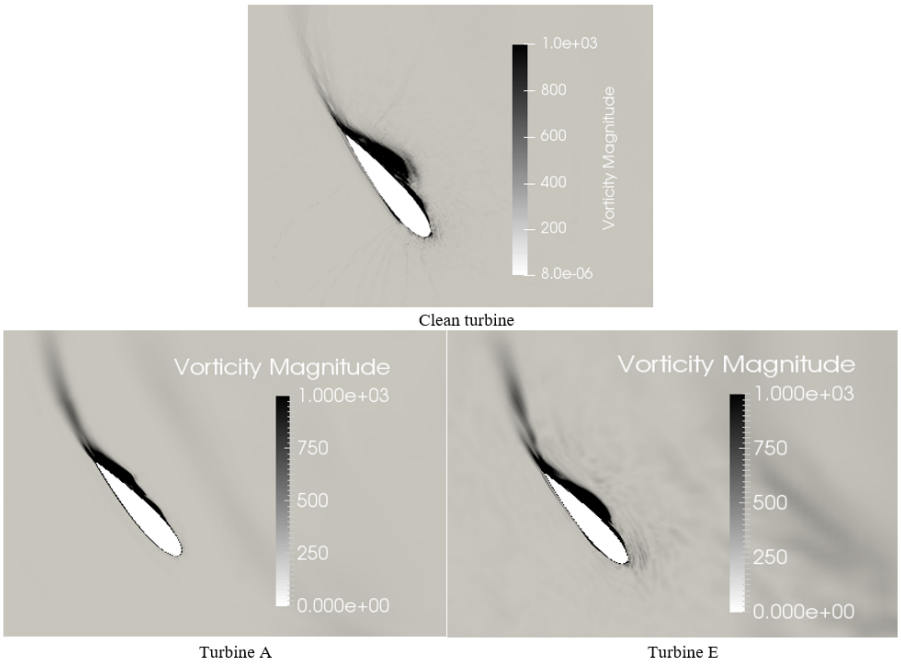


Fig. 5.36 Vorticity magnitude comparison of various turbines at $\theta = 130°$, TSR=3, LES.

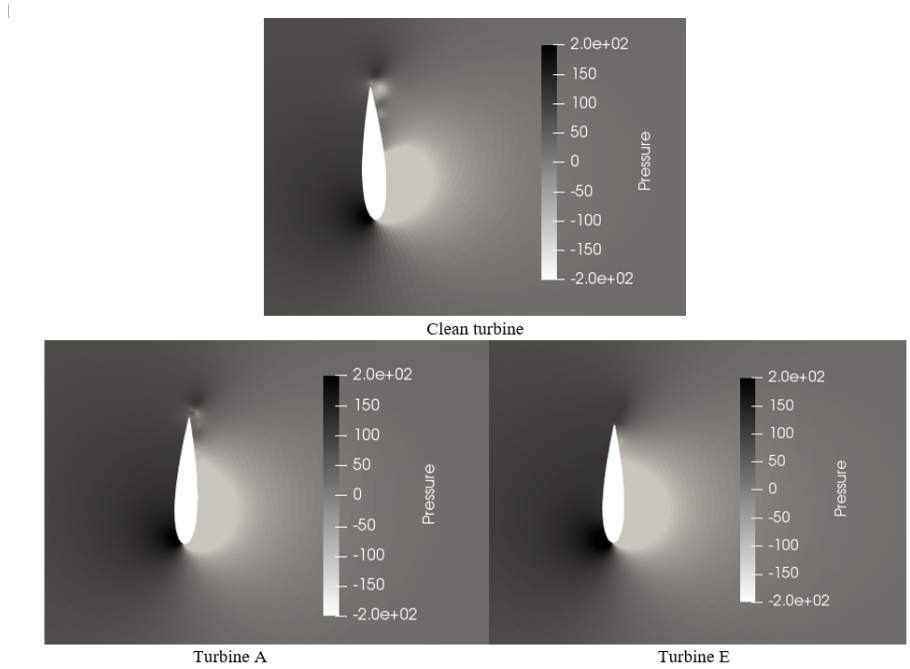


Fig. 5.37 Pressure contour of various turbine blades at $\theta = 90^{\circ}$, TSR=2.5, LES.

this azimuth angle for turbines A and E. The result agrees well with the moment coefficient distribution as Figure 5.33. The power output of turbine D is the lowest at $\theta = 90^{\circ}$ as compared to the other turbines.

### Effect of mounting angle on the performance of MVGs

Figure 5.38 shows a comparison between the clean turbine and the turbine with MVGs of various mounting angles in terms of torque coefficient and power coefficient versus TSR. It is noticeable that the mounting angle can affect the aerodynamic performance of the VAWTs. At low TSR from 1 to 2, the three turbines provide similar performance. When the TSR increases to 2.5, the power coefficients of turbine A and B follow each other very closely and produce more power output compared to the clean turbine. MVG C slightly degrades the power output of the turbine at the medium range of tip speed ratios of 2 to 3.

The comparison between these four models in terms of the instantaneous moment coefficient of a single blade operating at TSR= 2.5 and 3 for one revolution is presented in Figure 5.39. At both TSRs, the torques generated from these four turbines are found to increase with a very similar trend from $\theta = 0^{\circ}$ to $80^{\circ}$, which is similar to the models discussed before. A discrepancy starts to occur in the clean turbine and turbine C, which reach the peak value earlier as compared to the other two models. The moment coefficient for turbine A and

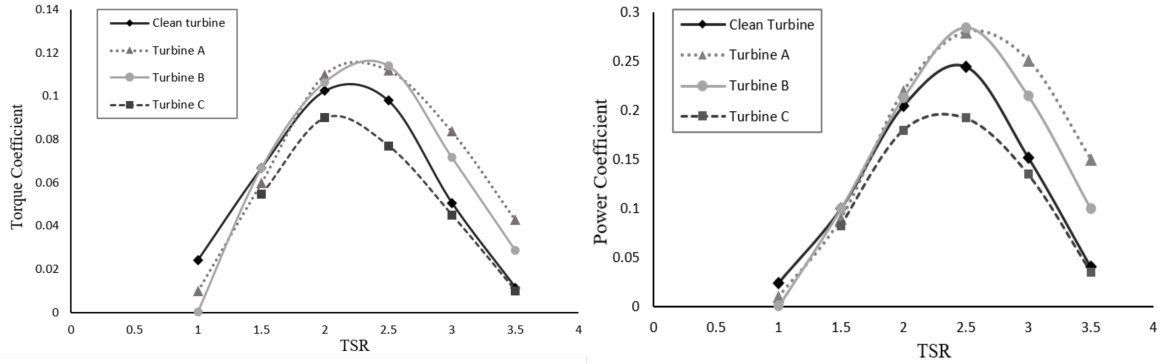


Fig. 5.38 Moment coefficient (right) and power coefficient (left) comparison of different turbines, LES.

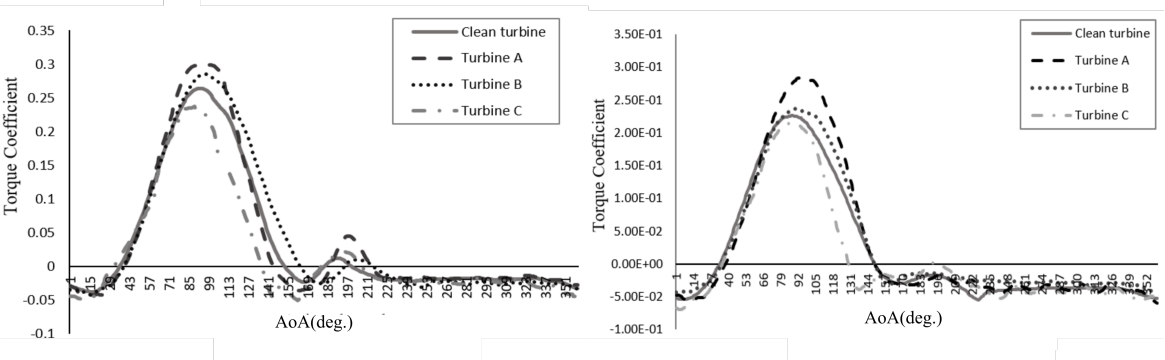


Fig. 5.39 Blade phase-averaged moment coefficient comparison of clean turbine and turbine A, B and C, TSR=2.5(left) TSR=3(right), LES.

turbine B continues to increase before reaching the peak value at around $\theta = 95°$. In the azimuth angle ranging from 80° to 150° , turbines A and B show a significant improvement in power output. At TSR=2.5, turbine B achieves the highest peak value of moment coefficient and at TSR=3, turbine A performs better as compared to the other models. All models generate a mild negative torque in the second half revolution and there is no significant difference between them at TSR=3.

When the blades are at the azimuth angle of 120°, the flow becomes highly separated due to the high angle of attack, showing a dynamic stall at this stage, which is related to a sharp torque decrease shown in Figure 5.39. Figure 5.40 shows the distribution of the vorticity at the azimuth angle 135°. From the visualization of the vortex, the flow separation is stronger in the clean turbine as compared to turbines A and B demonstrating the effectiveness of the MVGs.

The static pressure as relative to the atmosphere pressure contour is shown in Figure 5.41. All blades show similar pattern of the largest pressure difference between the pressure

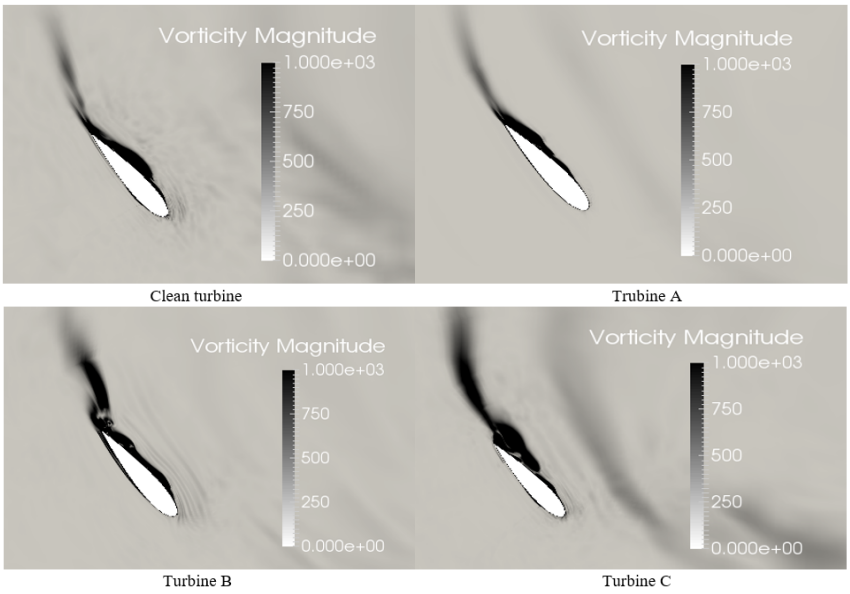


Fig. 5.40 Mid span vorticity magnitude comparison of various turbines at $\theta = 130^\circ$, TSR=3, LES.

(left) and suction (right) side near the tip as expected from aerofoil aerodynamics. The effect of the MVGs is clear on the suction side where it is mounted than on the pressure side. From turbines A and B, we can see that the low pressure region goes further into the trailing edge than in the clean turbine contributing to high pressure difference and thus higher lift. However, turbine C blade shows a reduced pressure near the trailing edge due to the vortex shedding and thus reduced lift as compared to turbines A and B. Its reduced pressure region near the leading edge. All this contributed to the lower $C_m$ by turbine C at $\theta = 90^\circ$ seen in the Figure 5.39 (left).

## 5.5 Conclusions

The purpose of the present study was to determine an effective passive flow control technique to enhance the aerodynamic performance of the NACA 0018 aerofoil commonly used in the wind industry and an associated H-type vertical axis wind turbine (VAWT). Firstly, the dynamics of an MVG vane embedded in the boundary layer of a flat plate was investigated. The time-averaged flow field is found to compare well with the published experimental results.

Several MVGs of various configurations implemented on the suction side of the aerofoil and turbine blades are numerically investigated. The results show that MVGs have a signif-

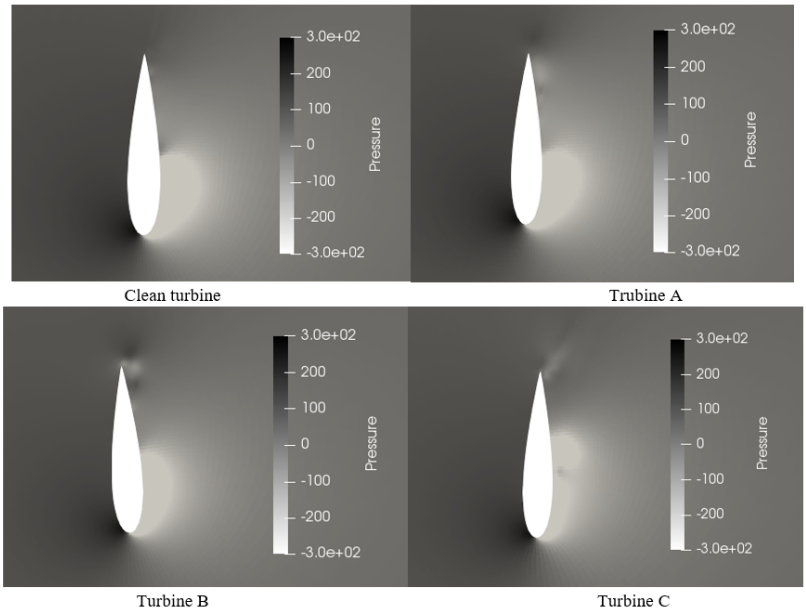


Fig. 5.41 Mid span pressure contour of various turbine blades at $\theta = 90^{\circ}$, TSR=2.5, LES.

icant effect on both the aerofoil and the turbine as a whole. With the MVGs of a suitable design, both the lift coefficient and lift-to-drag ratio can be increased at high angles of attack and the stall angle delayed. The turbine blades with MVGs show a better capability of power generation in comparison to clean blades, having a potential impact on future VAWT design.

The following conclusions can be highlighted:

1. For the isolated aerofoil NACA 0018, the optimum positioning of the MVGs was found to be at 20% chord length along the suction side of the aerofoil with a rectangular shape and mounting angle of 16°. The stall angle delays to 16° from 14° with the installation of MVGs. The maximum lift is improved by 37.5% from 0.96 to 1.32, while the drag decrease from to 0.178 to 0.137 at post stall condition $\alpha = 18^{\circ}$.

2. For the VAWT, a similar conclusion was obtained. The best performance was found for turbine A at high TSRs from $\lambda = 2.5$ to 3.5 in comparison with the other models. Among various TSRs, the MVG A has the most significant effect at TSR=3, where the power coefficient increases by more than 50% to 0.24. This investigation illustrates that MVGs can be an effective technique for delaying flow separation control in operating VAWTs at high TSRs.

# Chapter 6

# Performance Study of Leading-Edge Protuberance for Small-Scale VAWT

## 6.1 Introduction

This chapter presents the application of the leading-edge protuberance as a passive flow control technique on an isolated stationary blade and a Darrieus wind turbine.The three-dimensional CAD model of a single blade is shown in Figure 6.1. The leading-edge protuberance can improve the aerodynamic performance by introducing a pair of counter-rotating over each serration and thus eliminate flow separation at high angles of attack. In this study, sinusoidal wave serrations were implemented on the leading-edge of blade with the NACA 0018 profile. A comparison between the leading-edge protuberances of various parameters including amplitude and wavelength was conducted in terms of detailed flow characteristics and power generation of the VAWTs.

## 6.2 Computational Domain and Grid System

A sketch of the three dimensional computational domain is presented in Figure 6.2 (a). The streamwise and spanwise direction are defined as x and z directions respectively as shown in the figure. The mean chord length of serrated blade is c=0.246m and the span length is s=0.8m. The boundary conditions and the computational domain are similar to the numerical study of the aerofoils with micro vortex generators, which has been discussed in detail in the previous chapter.

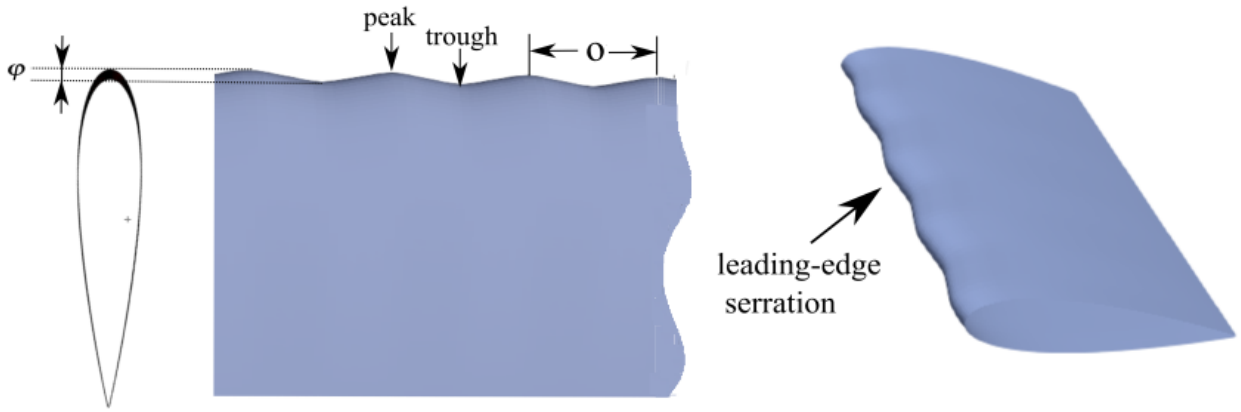


Fig. 6.1 Schematic view of the blade based on the NACA 0018 aerofoil with leading-edge protuberance.

The grid independence study was also conducted in the previous chapter. However, the serrated leading-edge can introduce high skewness and negative cell volumes near the wall. So the thickness of the first layer grid cell and the cells growth ratio need to be carefully selected . The zoom view of the grid resolution on the leading-edge protuberance is presented in Figure 6.2 (b). The length of first cell away from the wall is $0.5 \times 10^{-4}$ m in order to guarantee $y^+ < 1$. In the spanwise direction, there are 300 cells on the blade with equal spacing, resulting in $z^+ < 50y^+$. The mesh resolution is higher as compared to the aerofoil with a straight leading edge, which was comprising around $0.25 \times 10^6$ cells in total.

ANSYS Fluent software was used for the (U)RANS calculations applied to the isolated blade, whereas LES simulations were performed by Code_Saturne on the VAWT. The numerical setup has been discussed in Chapters 3 and 5, so the numerical method will not be discussed in further details here. It should be also noted that the code validation for both Fluent and Code_Saturne was reported in the previous chapter.

In this study, five different types of sinusoidal leading edge serrations with three different wavelengths and amplitudes were investigated. The values of amplitudes ($\varphi$) implemented were 0.01c, 0.02c and 0.03c and the wavelengths (o) were 0.2c, 0.3c and 0.4c.

## 6.3 Aerodynamic Forces on the single stationary blade

The calculated lift and drag forces are presented in this section for the baseline blade and blades with leading-edge protuberances. In the legend, "Unmodified " refers to the base line

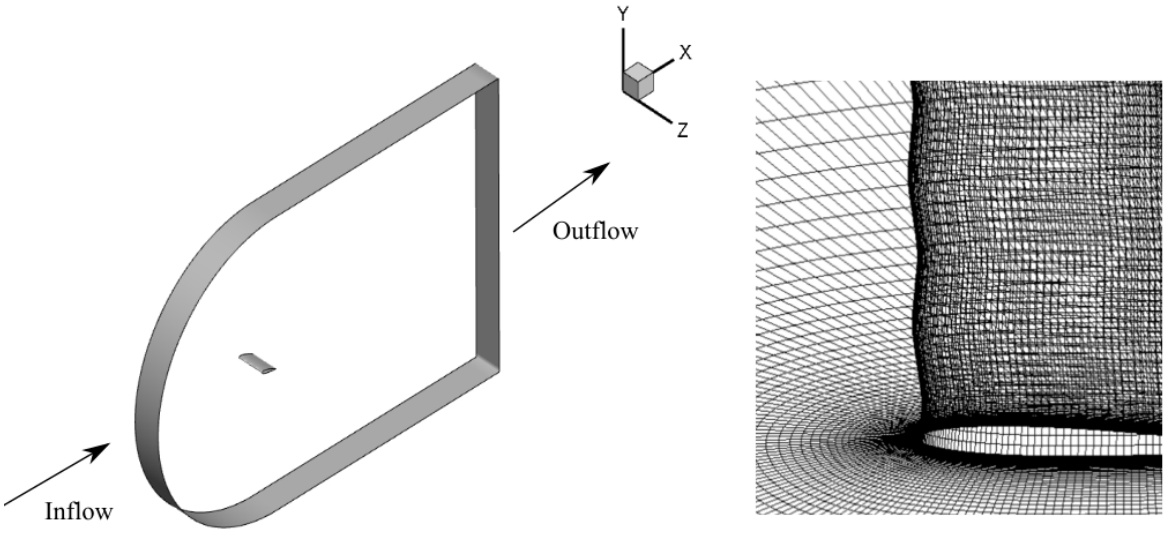


Fig. 6.2 (a) Three-dimensional computational domain.(b) Mesh distribution near the junction between the periodic boundary and leading edge of the blade.

blade. S1 to S5 refer to blades with various leading-edge protuberances. The parameters of leading-edge protuberances for S1 to S5 blades are given in Table 6.1.

Table 6.1 Parameters of leading-edge protuberances

| Aerofoil | Amplitude (g) | Wavelength (w) |
|---|---|---|
| S1 | 0.02c | 0.4c |
| S2 | 0.01c | 0.4c |
| S3 | 0.03c | 0.4c |
| S4 | 0.02c | 0.2c |
| S5 | 0.02c | 0.3c |

### 6.3.1 Effect of the Amplitude

The lift coefficient $C_L$ for the blades with leading-edge protuberances of different amplitudes is plotted in Figure 6.3 (a) as a function of angle of attack (AoA). The protuberanced blades have the same leading-edge protuberance wavelength. The lift coefficient increases linearly with $\alpha$ for all blades up to 9°. After that, the lift coefficient for S3 starts to decline slightly until $\alpha = 12°$, which is different from the other cases. The baseline blade $C_L$ keeps increasing at a mildly reduced rate up to $\alpha = 14°$, reaching the peak value $C_L = 0.94$ before it stalls. Stall occurs at about $\alpha = 14°$ and $C_L$ decreases significantly until $\alpha = 20°$. For $\alpha > 21°$,

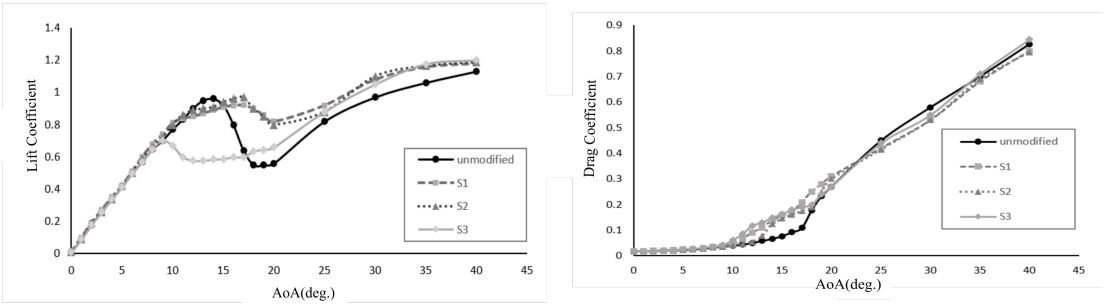


Fig. 6.3 Lift coefficient comparison of blades with LE protuberance of different wave amplitude.

the post stall $C_L$ for the baseline increase continuously. The curves of S1 and S2 follow a similar trend as the baseline, keeping increasing up to $\alpha = 16^\circ$, where the $C_L$ starts to drop to a plateau value, before increasing again at $\alpha = 20^\circ$. At $20^\circ < \alpha < 40^\circ$, the $C_L$ for S1 and S2 keep increasing at a reduced rate as compared to the linear case of small AoA.

As seen in the plots, the blades with leading-edge protuberances have a milder stall characteristic than the baseline aerofoil, especially for S1 and S2, indicating the effect of stall suppression. However, the stall angles and the peak values of $C_l$ at the stall angle for the protuberanced blades are slightly lower. Post stall, the blades with leading-edge protuberances provide higher lift coefficient than the baseline blade at the angle of attack ranging from $17^\circ$ to $40^\circ$. Among the protuberanced blades, S3 with the leading-edge protuberance of the largest amplitude has a relatively small lift coefficient than S1 and S2 at $10^\circ < \alpha < 25^\circ$, while there is no obvious difference between S1 and S2 in this range of angle of attack. It could be conclude that the leading-edge separation type of the blade changed to trailing-edge separation type, in which condition the sudden stall is replaced by the gentle stall from separation based on Hoerner's theory as discussed in Chapter 2 [48].

The drag coefficients $C_d$ for the protuberanced and baseline blades are compared in Figure 6.3 (b). As seen in the figure, an apparent discrepancy exists between the baseline blade and serrated leading-edge blades near the stall at $10^\circ < \alpha < 20^\circ$. The largest $C_d$ values at all the selected angles of attack belong to the blade with the largest amplitude protuberance (S3). For $20^\circ < \alpha < 30^\circ$ the $C_d$ of protuberanced cases are quite close to the baseline blade. In the range of $30^\circ < \alpha < 40^\circ$, the $C_d$ for S1 and S2 are slightly higher than the baseline blade.

The variation of lift-to-drag ratio is shown in Figure 6.4. It can be seen that the maximum lift-to-drag ratio could be obtained at AoA of $8^\circ$ for both unmodified and modified cases.

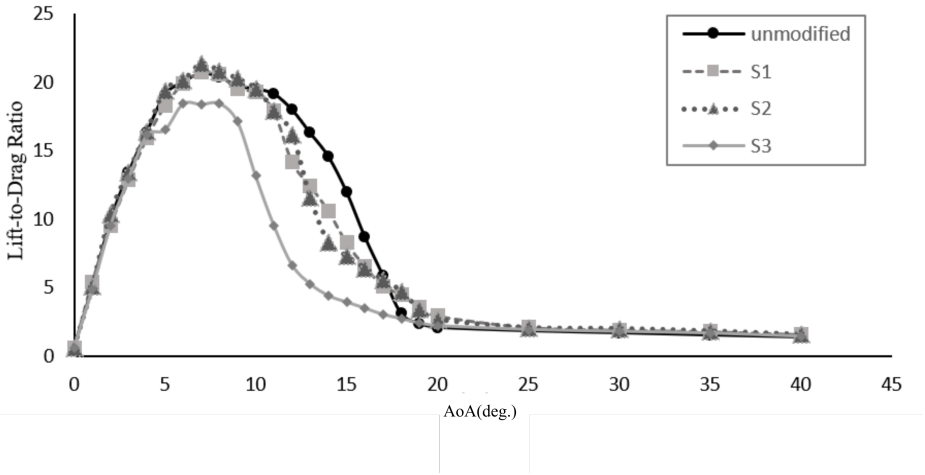


Fig. 6.4 Lift-to-drag ratio comparison of blades with LE protuberance of different wave amplitude.

The maximum lift-to-drag ratio for S1 is 21.6, which is 5.4% larger than the unmodified model .At the angle of attack ranging from 12° to 18°, the baseline blade has the largest lift-to-drag ratio as compared to the serrated leading edge blades. The blade S3 with the largest amplitude protuberance performs the worst within the investigated $\alpha$ range. At higher AoAs from 18° to 40°, the serrated leading-edge blades S1 and S2 have larger lift-to-drag ratios in comparison to the baseline blade, but the difference is small. It could be found that the amplitude of the protuberance can affect its performance seriously. When the amplitude exceeds a critical value, the leading-edge protuberance cannot improve, but degrade the performance of the blade.

### 6.3.2 Effect of wavelength

The lift and drag coefficients for the blade with three leading-edge protuberance wavelengths (S1, S4 and S5) and the baseline blade are compared in Figure 6.5 for the same protuberance amplitude of 0.02c. It appears that the difference in terms of both lift and drag coefficient are small between the three wavelengths. The cases of S5 and S5 have the similar performance with S1 in terms of lift and drag variations. As the result, the difference on the lift-to-drag ratio is marginal(Figure 6.6).

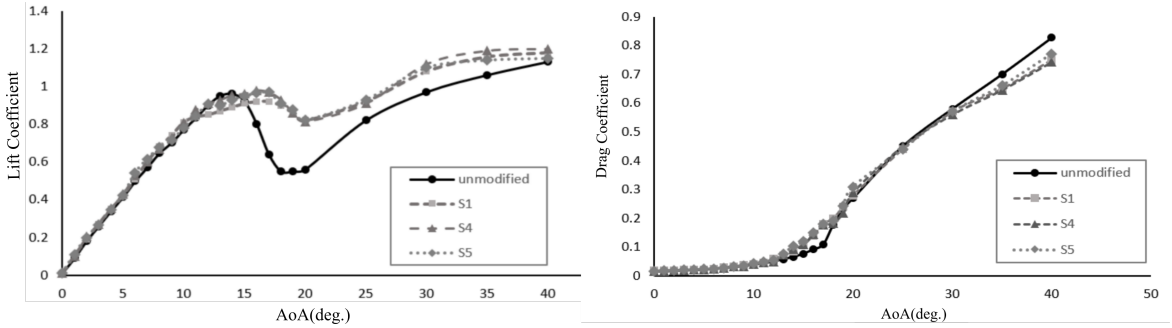


Fig. 6.5 Lift and drag coefficient comparison of blades with LE protuberance of different wavelength.

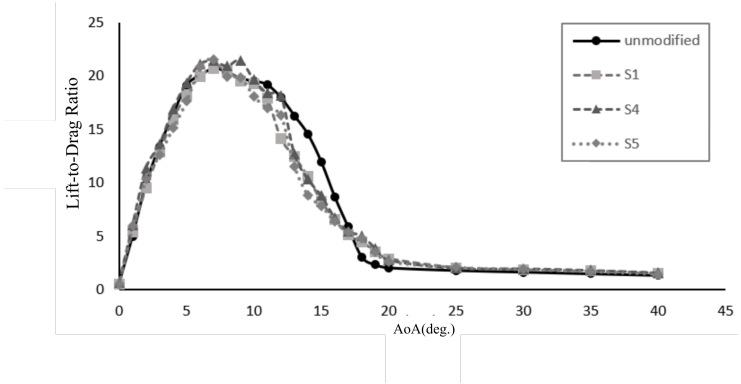


Fig. 6.6 Lift-to-drag ratio comparison of blades with LE protuberance of different wavelength.

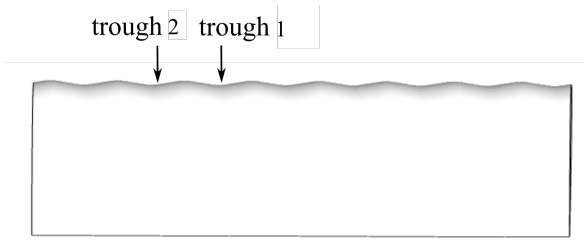


Fig. 6.7 Schematic view of the trough 1 and trough 2 on the leading-edge protuberance of the blade.

## 6.4 Flow Physics of Leading-Edge Protuberances

### 6.4.1 Velocity and vorticity Field

The distribution of the velocity magnitude of the baseline case and the feature slices of serrated leading-edge blades at $\alpha = 18^\circ$ are shown in Figure 6.8. Because the LE protuberance has significant effect on lift enhancement at this AoA. As shown in the figure, the boundary layer on the suction surface of the baseline blade is fully separated. The majority of suction side is covered by a long vortex and a counter-rotating secondary vortex behind it.

For the unmodified blades, the flow on the spanwise slices of two adjacent troughs (denoted as trough 1 and trough 2) of the protuberance are investigated as shown is Figure 6.7. The separation states are different between trough 1 and 2. For the trough 1 of S1 and S2 cases, similar separation vortices can be observed, and it is not far from the baseline case. Around trough 1 of S3 case, a larger separation is observed and the main vortex raises up. However, the flow separation in trough 2 is weaker than the trough 1 of the same blade. For S1 and S2 on trough 2 slices, the attached flow covers 25% and 20% the suction surface respectively, with one small vortex near the trailing edge. The separation on the slice of trough 2 of S3 is larger and the separation point moves upstream nearly reaching the leading edge of the blade.

### 6.4.2 Boundary-Layer and streamlines

In order to reveal the flow mechanism around the leading-edge protuberance, streamwise velocity profiles of the boundary layer flow above the suction side for various spanwise slices are investigated. The y coordinate denotes the distance in the direction normal to the local blade's surface and x coordinate denotes the streamwise velocity normalized by the freestream velocity $U_\infty$ i.e. U/$U_\infty$. For each xy section, eight velocity profiles were chosen

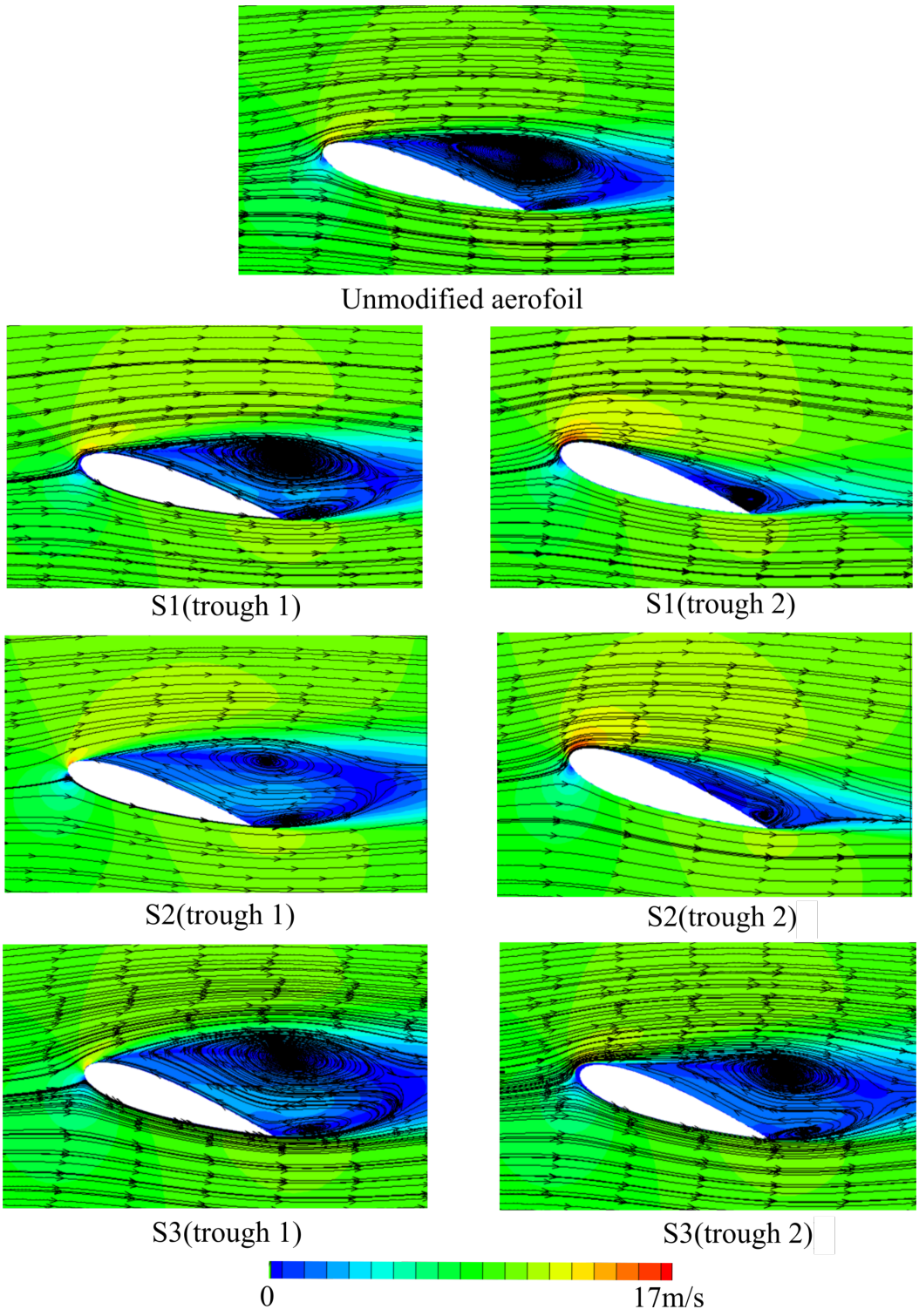


Fig. 6.8 Contours of the time-averaged velocity magnitude at $\alpha = 18^{\circ}$ for the unmodified, S1, S2 and S3 blades.

for the analysis with different streamwise locations. Their normalized distances (x/c), along the suction side surface are labeled above each profile in the figure.

The boundary layer thickness ($\delta$) is defined as the normal distance from the wall to a point where the flow velocity has reached the free stream velocity as shown in equation 6.1.

$$U_0 = 0.99U_\infty \tag{6.1}$$

where $U_\infty$ denotes the free stream velocity and $U_0$ is the flow velocity at the point whose distance to the wall is the regarded as boundary layer thickness.

At $\alpha = 16^\circ$, the separation occurs at somewhere between x/c=0.2 and x/c=0.3 for the baseline blade. After that, the boundary layer thickness gradually increases along the downstream direction reaching about 0.16m at x/c=0.8. In the line of x/c=0.8, when the wall distance is ranging from 0.025 to 0.1, the velocity smaller than 0 can be observed, corresponding to reverse flow in that region, which indicates the occurrence of flow separation. For the trough cases in S1 and S3, the laminar flow tends to separate between x/c=0.2 and x/c=0.3 as well and the separation for S3 is more serious in comparison with S1. However, in trough 1 of modified cases, the growth rate of boundary layer thickness is higher as compared to the baseline blade. At x/c=0.8, the $\delta$ for the cases trough 1 of S1 and S3 reach 0.18 and 0.23m respectively. Separation occurs earlier at around x/c=0.2 for the case of trough 1 in S2.

The flow separation conditions are different in trough 2 cases for the protuberanced models. In S2, the onset of reverse flow moves backward to a location between x/c=0.3 and x/c=0.4 indicating a postponed laminar separation as compared to the baseline. The $\delta$=0.11m at x/c=0.8 is also much lower than the baseline case. The separation point at a similar location can be observed in trough 2 for case 3, although the separation is larger than that on trough 2 in S2. There is no obvious reverse flow in trough 2 of S1, indicating the laminar flow covering the relatively larger part of the section in its suction side before separation occurs as compared to other models, which should be also found in Figure 6.14. As shown in Figure 6.14, the flow separation in trough 1 is heavier as compared to trough 2 slices for both S1 and S2. The flow is more attached in trough 2 of S1 than that of S2. This agrees with the distribution of streamlines as discussed previously.

The potential flow streamlines just above the boundary layer will be slightly displaced away from the wall by the boundary layer. Displacement thickness( $\delta^\star$) is basically defined as the distance across a boundary layer from the walls, by which the boundary should be displaced to compensate for the reduction in flow rate on account of boundary layer formation [100]. In addition, we define the momentum thickness ( $\theta^\star$) as the distance, by which the boundary should be displaced to compensate for the reduction in momentum of the

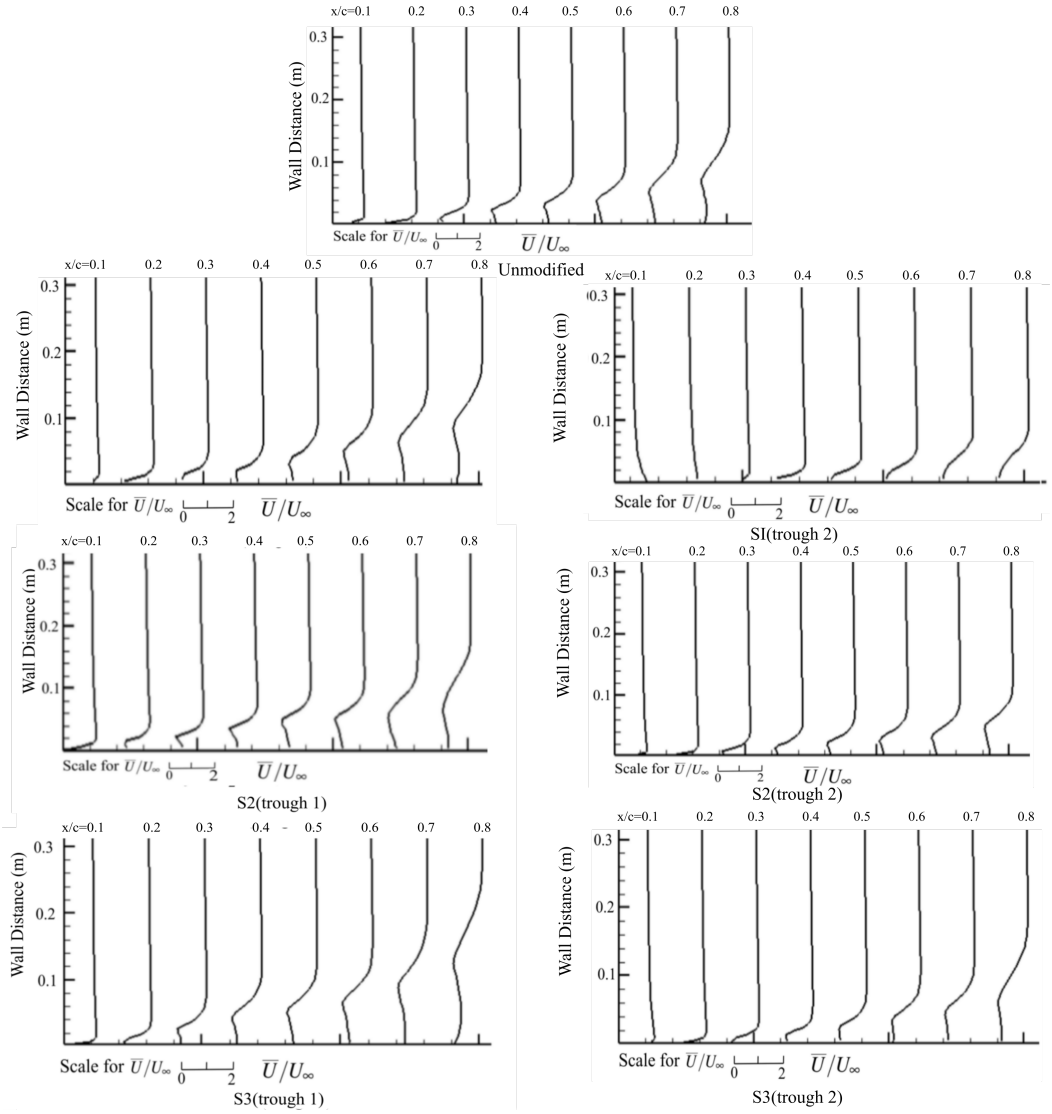


Fig. 6.9 Streamwise velocity profiles of the boundary layer flow at $\alpha = 16^\circ$.

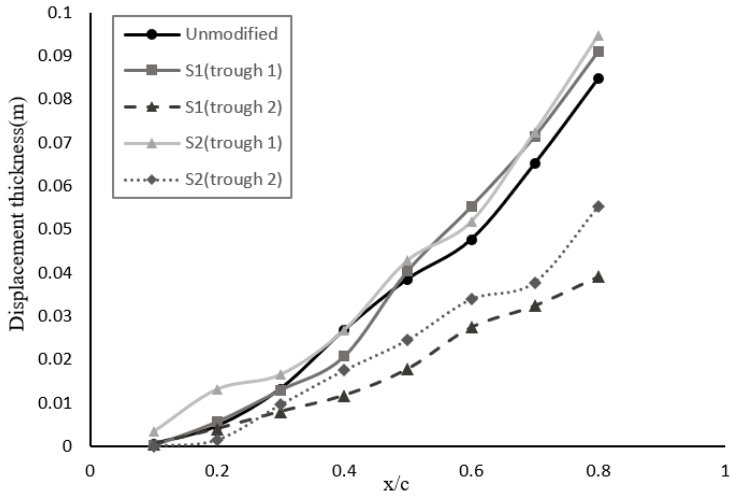


Fig. 6.10 Variations of boundary layer displacement thickness with streamwise distance x/c with and without leading-edge protuberances at $\alpha = 16°$.

flowing fluid on account of boundary layer formation [100]. The displacement thicknesses as functions of streamwise position are shown in Figure **??**. Displacement thickness gradient increases along the streamwise direction for the unmodified model and the trough 1 section of both S1 and S2 model. And the trough 1 of modified model has relatively larger displacement thickness as compared to the unmodified model. The enhancement rate and the value of the displacement thickness of trough 2 section for S1 and S2 is smaller than other three models, especially in the region near the trailing edge of the blade, indicating less flow separation as shown in Figure 6.8.

The shape factors ($H_s$) of the boundary layer, which is defined as a ratio of the displacement thickness to the momentum thickness are used to understand the behaviour of boundary layer.The shape factor in different blades are compared to the shape factor of the unmodified blade at different streamwise slice in Figure 6.11. Shape factor is usually used to locate separation point. In general, a larger shape factor indicates that the boundary layer is more prone to separation [124]. As seen in figure, smaller shape factors compared to that in the uncontrolled cases are observed in trough 2 slice of both S1 and S2 model. The shape factor variation of trough 2 slices in both controlled model shows a similar trend with the unmodified blade. This result shows a reasonable agreement with the flow control effect of the leading edge serration as discussed above.

This variation of flow structure along the spanwise direction may be due to the existence of "bi-periodic" phenomenon. As indicated by Dropkin et al., the "bi-periodic" phenomenon means that on the suction side of the blade, the streamlines and vortex structures converge and

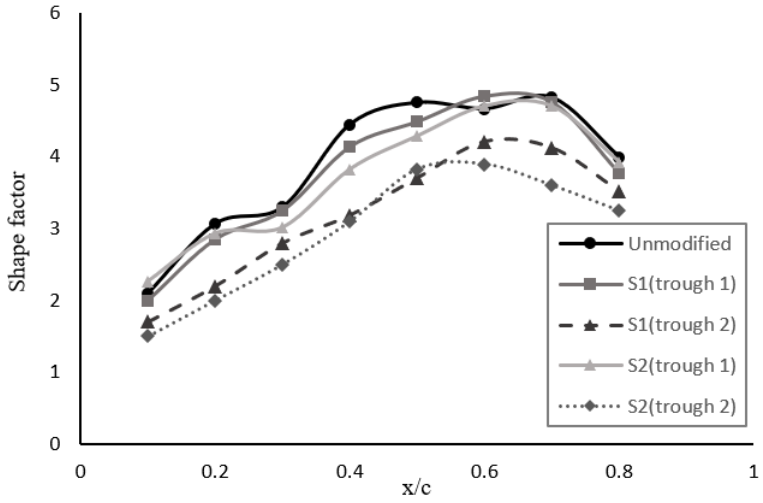


Fig. 6.11 Variations of boundary shape factor with streamwise distance x/c with and without leading-edge protuberances at $\alpha = 16^{\circ}$.

diverge in adjacent trough sections of protuberances with the existence of non-equilibrium of velocity and static pressure, which had been proved to be effective to increase the aerodynamic performance of the blade around stall region [22][127].

Pressure contours on the surface of the protuberanced and baseline blades at $\alpha = 18^{\circ}$ are shown in Figure 6.12. The pressure difference on the suction side of various blades can be observed. On the blades with leading-edge protuberances, the low-pressure region is wave shaped, with a larger area as compared to the baseline case. It was found that the aerodynamic suction (negative $C_p$) on the upper surfaces of the blades (S1 and S2) is higher than on the baseline blade, leading to a higher lift. This agrees with the result in Figure 6.3.

Figure 6.13 compares the distributions of the pressure coefficients along the x-direction of two adjacent trough slices of S1 and the midspan section of the baseline case at $\alpha = 18^{\circ}$. The difference of pressure distribution between two trough sections emerges due to "bi-periodic" phenomenon, which has great influence on stall performance. As shown in the figure, the suction on trough 2 near the leading edge for S1 is higher as compared to other slices, leading to a higher lift generation. The trough 2 slice has a similar pressure distribution as the baseline case. Zhao et al.[127] and Cai [13] obtained a similar result pointing to the advantages of the serrated leading edge was observed at the post stall region, where the lift declined significantly for the baseline blade.

The streamlines on the suction surface of the four blades are illustrated in Figure 6.14 at $\alpha = 16^{\circ}$, at which stall occurs for the baseline case. Different flow patterns have been observed for the serrated blades. There are two pairs of counter-rotating vortices within eight

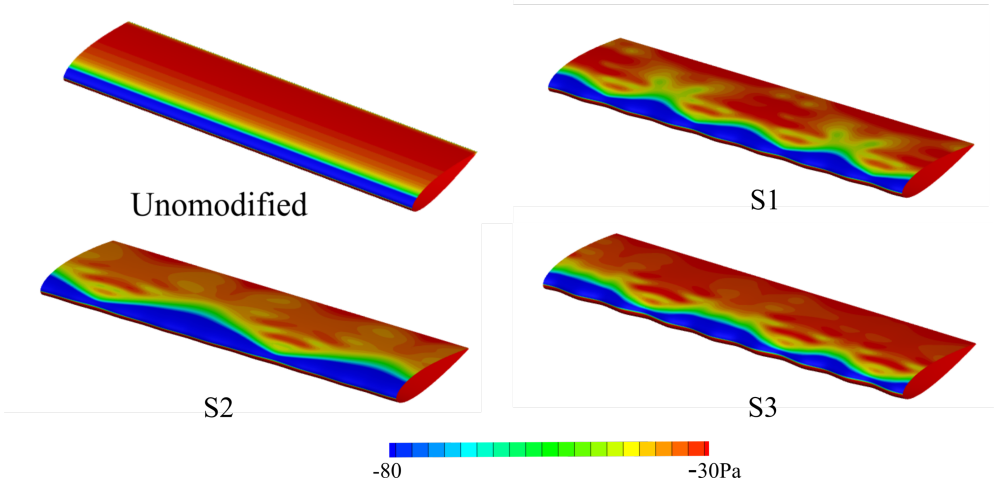


Fig. 6.12 Pressure (as relative to ambient pressure) contours on surfaces of different blade configurations at $\alpha = 16°$.

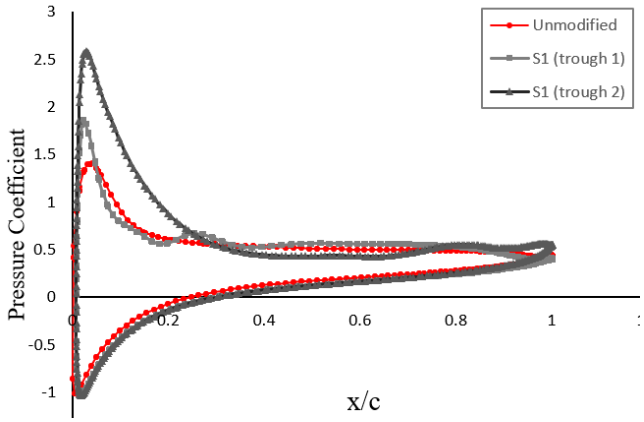


Fig. 6.13 Distributions of pressure coefficient along x-direction at $\alpha = 16°$.

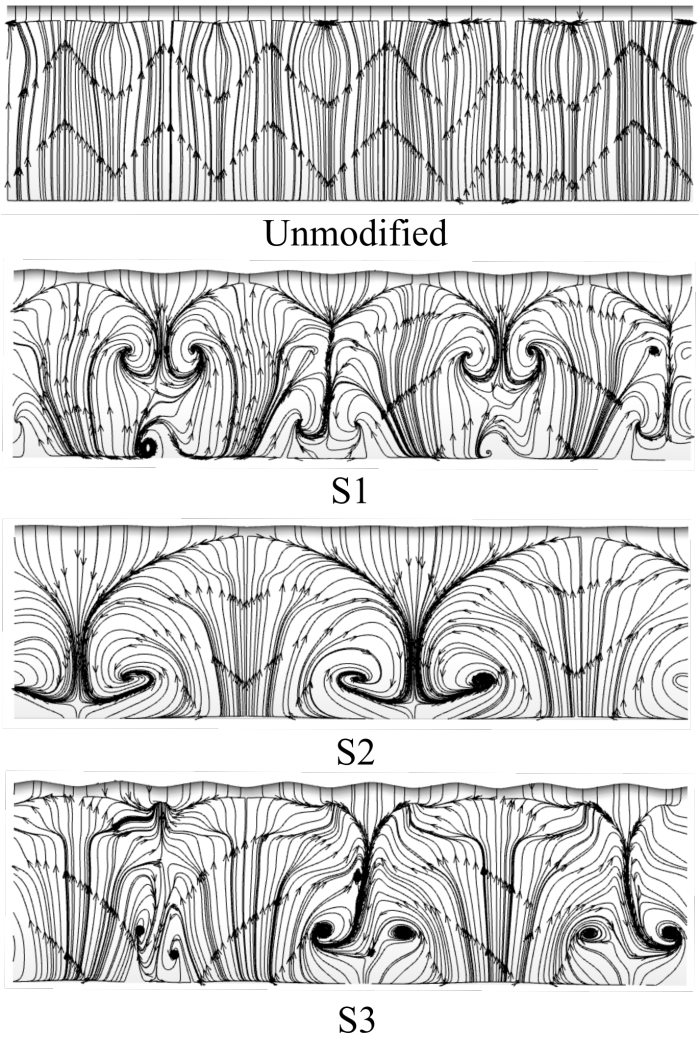


Fig. 6.14 Streamlines over the suction side of the blade with and without leading-edge protuberances at $\alpha = 16^{\circ}$.

protuberances for S1 and S2. The separation point varies along the spanwise direction of the blade. In general, the separation point moves downstream for the two modified models (S1 and S2) as compared to the baseline case indicating a suppression of flow separation, while the vortex for S2 is located relatively downstream in comparison with S1. As a result, the spanwise variation introduced by the leading-edge protuberances increases the suction of the upper surface of the aerofoils, leading to a higher lift after stall. Larger vortex can be observed in S3 and the flow pattern does not strictly change periodically in spanwise direction, indicating a larger flow separation.

In order to investigate the development of the "bi-periodic" phenomenon on the blade's stall performance and the relative vortex dynamics after stall, the streamlines over the suction

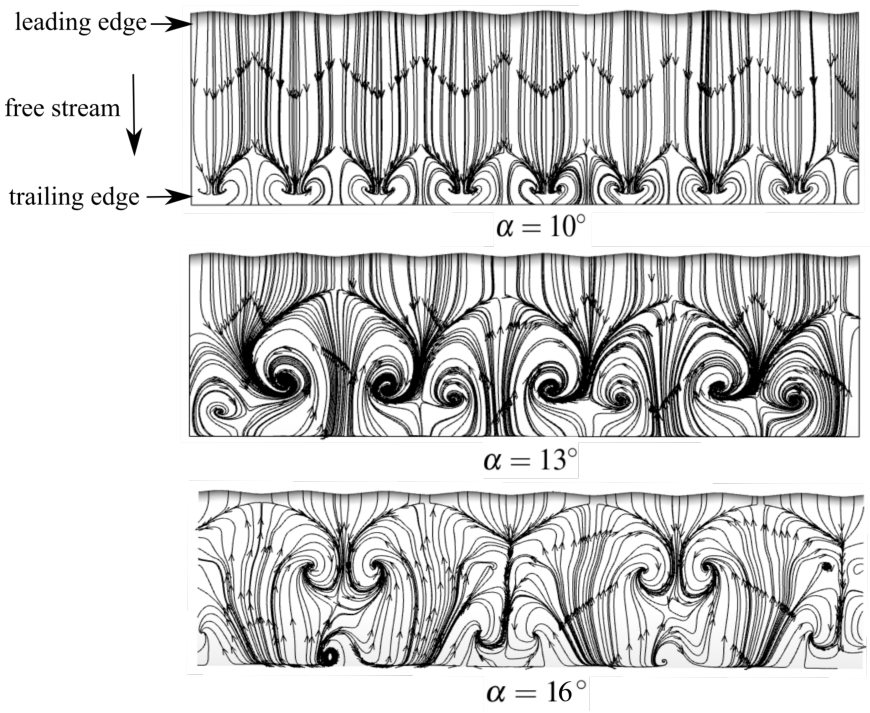


Fig. 6.15 Streamlines over the suction side of the blade S1 at various angle of attack.

surface of S1 blade are present in Figure 6.15 at various angles of attack, representing pre-stall and post stall regions. As shown in Figure 6.15, the near-wall flow is attached along the most of the suction surface with straight streamlines at $\alpha = 10°$. Near the trailing edge of the suction surface, a couple of counter-rotating separation vortices are formed around each protuberance for the protuberanced blades. In S1, the streamline structure is periodic with respect to each protuberance in the spanwise direction. Larger flow separation can be observed in the trough sections as compared to the peak regions. At $\alpha = 13°$, the periodic phenomenon of the flow structure is replaced by a "bi-periodic phenomenon" spanwise for S1 and the number of the vortex pairs reduced to four. The vortice is diffused in one trough and confined in its neighboring trough, indicating the flow interaction between adjacent troughs. In addition, the vortices move upstream with the increase of AoA. This interaction between the vortices becomes stronger at $\alpha = 16°$, where the "bi-periodic phenomenon" become less obvious.

The vortex structure over the blade S1 at various angles of attack can be shown by the iso-surface of Q= 100 colored by the vorticity magnitude in Figure 6.16. At the lower angles of attack $\alpha = 10°$ and $\alpha = 13°$, two distinctive vortex structures can be seen. One is attached to the suction surface of the blade near its trailing edge and the other is the pairs of streamwise counter-rotating vortices in the wake. At $\alpha = 10°$, the vortex pattern is periodic in spanwise

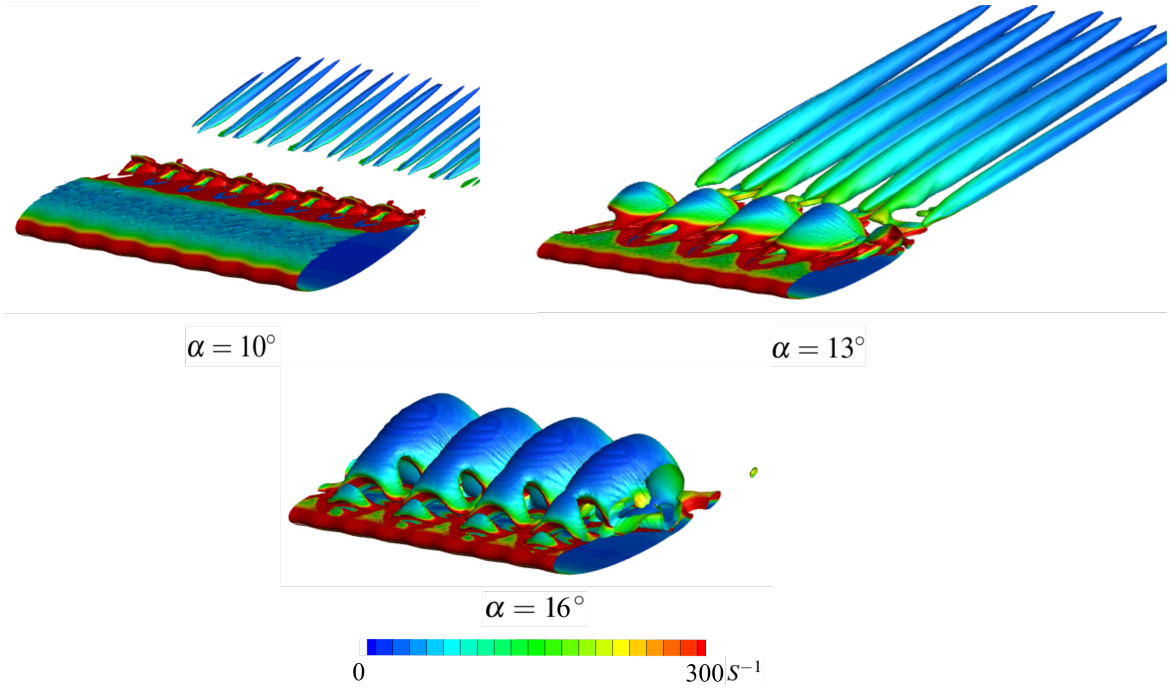


Fig. 6.16 Iso-surface Q= 100 colored by vorticity magnitude at $\alpha = 18°$ for blade S1.

direction. A pair of streamwise vortices can be observed behind each protuberance, which corresponds to the streamline structure as seen in Figure 6.14. When the AoA increases to 13°, the "bi-periodic" phenomenon can be observed, with diverged and converged vortices in neighboring troughs with higher vorticity magnitude as compared to the lower AoA of $\alpha = 10°$. At $\alpha = 16°$, the vortex structure becomes largely attached on the blade with large separation downstream about 0.25c from the leading edge. Similar result regarding to the variation of vortice structure was obtained by Cai et al.[13].

## 6.5 Effect of Leading-Edge Protuberances on the small-scale VAWT

In the previous section, the implementation of the leading-edge protuberance within the NACA 0018 aerofoil is numerically studied. The optimum configuration among the five tested blades is then applied in the vertical axis wind turbine based on the same blade section to assess the ability of leading-edge protuberances to suppress the flow instabilities and eventually improve the aerodynamic performance of the VAWT. As discussed in the previous section, the amplitude of the protuberance shows a greater impact on the performance of

the isolated blade as compared to the wavelength. The effect of the amplitude for the power outputs of the VAWT will be discussed in this chapter.

### 6.5.1 Flow Control Strategy and Numerical Setup

As with the previous section of MVGs, the leading-edge protuberances of S1 and S2 that was proved to have positive effect on the isolated blade were applied to the wind turbine blade. The typical three-bladed H-type Darrieus turbine was used in the present numerical investigation. The parameters of the turbine rotor is similar as the turbine in the previous chapter, except for the blade height. In this chapter, the height of turbine blade is 0.4m, which includes four wavelengths of the sinusoidal protuberances on the leading edge.

The modeling of the full wind turbine with and without leading-edge protuberances implemented was carried out with Code_Saturne. LES modeling was adopted with the same numerical setup and boundary conditions in the last chapter. This numerical framework has been verified in the previous chapter. Therefore the numerical methods and mesh distribution will not be indicated in detail here.

### 6.5.2 Flow Control Effect

#### Power coefficient

The plot of the power coefficient $C_P$ of the turbines as a function of TSR ranging from 1 to 3.5 and with an interval of 0.5 is depicted in Figure 6.17. In the legend, the "unmodified" refers to the baseline case with no protuberances. "S1"and "S2" stand for the VAWT with the leading-edge protuberance profile of S1 and S2 respectively. As seen in the figure, only slight difference in the power outputs can be observed between the unmodified and improved model when the TSR is larger than 3, while obvious improvement can be observed due to the leading edge protuberance at low TSR ranging from 1 to 3. The protuberanced case shows a larger maximum power coefficient than that of the unmodified model. The power output of the S2 case with the protuberance of k=0.01c is slightly larger than S1 case with k=0.02c. The $C_P$ is increased by 14.2% with the leading-edge protuberance operating for S2 at TSR = 2.0, while an improvement of 15.3% can be achieved when operating at TSR = 1.5 as compared to the unmodified model. In general, the leading edge protuberances that enhance the performance of the isolated blade, can also increase the power generation of the VAWT. Among the cases with protuberances, S2 protuberance with the amplitude of 0.01c has better performance on the VAWT in terms of the power output.

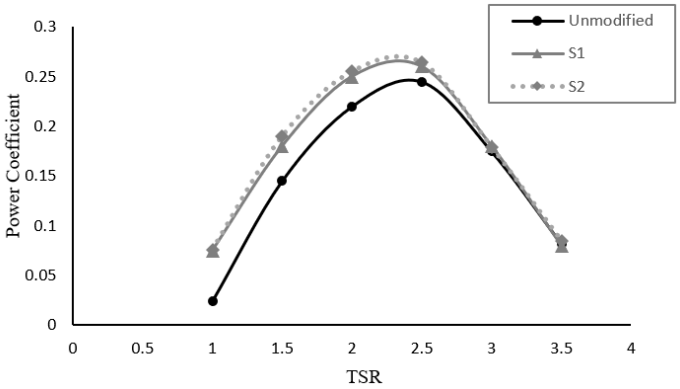


Fig. 6.17 Power coefficient versus TSR for the VAWTs with and without leading-edge protuberances.

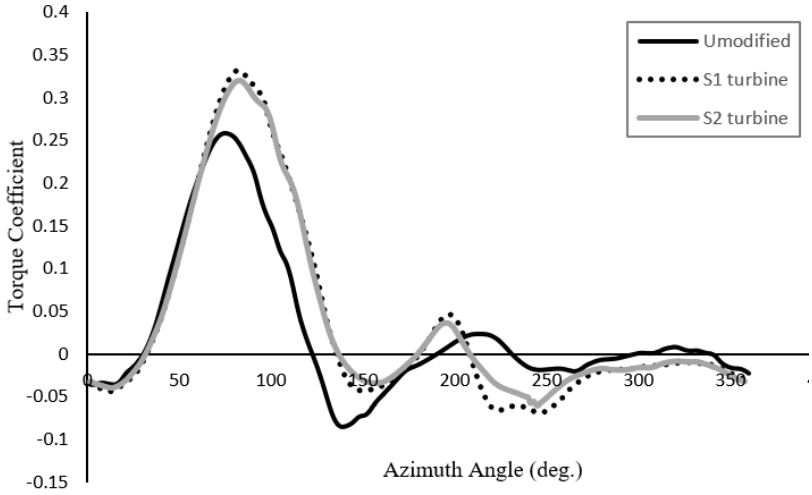


Fig. 6.18 Torque coefficient variation with azimuth angles $\theta$, TSR=2.

The variations of the instantaneous torque coefficient ($C_m$) against the azimuth angle in one cycle operating at TSR = 2.0 are illustrated in Figure 6.18. The definition of azimuth angle ($\theta$) was defined in chapter 5. All tested turbines follow a very similar trend from 0° to 70°. The torque coefficient of the unmodified model reaches its peak value of 0.318 at around $\theta = 72°$ and starts to decline, while for the protuberanced models, the $C_m$ continues to increase till reaching their peak value at $\theta = 84°$. All the cases experienced a sharp decline after reaching their peak values. The unmodified case reduced to the minima earlier as compared to the modified models. Although a slightly higher torque output can be obtained by unmodified case at the azimuth angles ranging from 205° to 360°, the improved models are found to have larger overall power generation as compared to the unmodified model, while there is little discrepancy between the two protuberanced models.

### Effect on Dynamic (Rotating) Stall

The power generation of a VAWT is directly associated with the dynamic stall of the turbine's blades. In order to better understand the flow separation condition of the turbine's blade section, the contour of the vorticity magnitude around the blade profile of different turbines at TSR=2.0 are illustrated in Figure 6.19. As shown in the figure at $\theta = 70^{\circ}$, flows are attached on the blade surface and no flow separation is observed at this azimuth angle for all the three cases. However, a larger area of a positive vorticity magnitude can be observed over the suction side of unmodified model. When the azimuth angle increases to $90^{\circ}$, the area of positive vorticity magnitude on the suction side of blades for improved models is larger as compared to the baseline case, which indicates that the separation is slightly suppressed. This is in agreement with larger power output seen in Figure 6.18. As the turbine blades keep rotating to the next stage with $\theta = 120^{\circ}$, the flow separation becomes more serious. The three models experience deep dynamic stall at this stage, while the stall of the unmodified turbine is more profound as compared to the improved models. The discrepancy of the wake structure of the two improved models can be observed at this stage and the dynamic stall is slightly weaker for S2 model. The dynamic stall is still present at $\theta = 150^{\circ}$ with a relatively larger separation region near the blade of the unmodified model as compared to the improved cases S1 and S2.

The evolution of the boundary layer and downstream vortex can be evaluated by the skin friction coefficient, which is defined as $C_f = \frac{\Gamma_w}{0.5\rho U_{\infty}^2}$, where $\Gamma$ refers to the wall shear stress. The wall shear stress distributions on the suction surfaces of turbine blades are given in Figure 6.20 at three different azimuth angles. Higher wall shear stress indicates a stronger interaction between the vortex and wall, leading to a weaker flow separation. As shown in the figure, improved models have relatively higher wall shear stress, resulting a weaker dynamic stall as compared to the unmodified model, which agrees with the vorticity distribution as in Figure 6.19.

### Lift and drag coefficients

To better understand the flow physics around the turbine blades and to investigate the dynamic stall characteristics of the rotor blades, the dynamic variation of the lift and drag coefficients ($C_L$ and $C_D$) of a single turbine blade operating at TSR = 2.0 are provided in Figure 6.21 and 6.22 respectively. Since models of S1 and S2 has a similar blade torque variation as shown in Figure 6.18, only S1 model will be discussed in this section. The variation of the angle of attack with the azimuth angle is plotted as well for reference, which was calculated in the

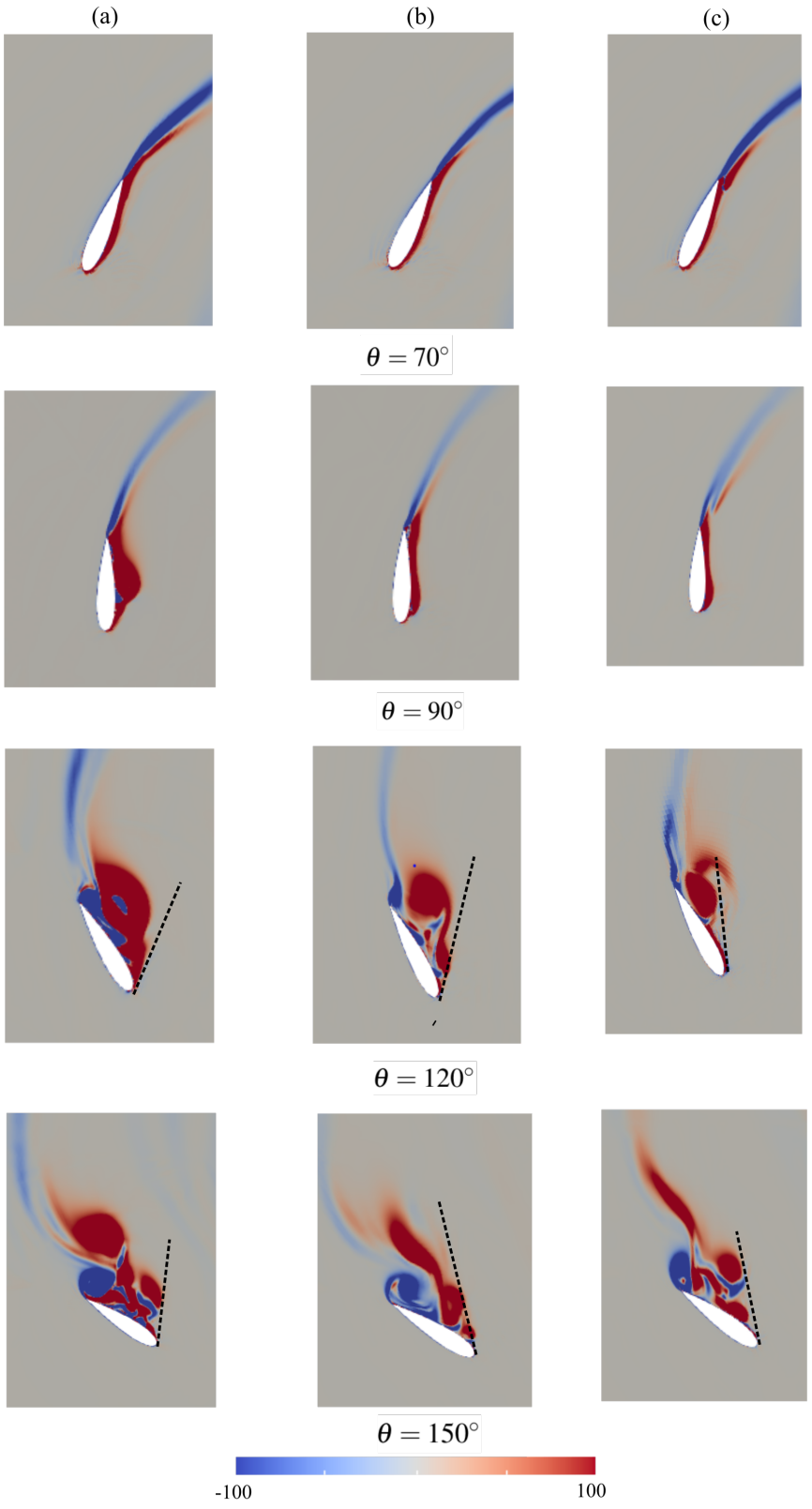


Fig. 6.19 Vorticity distributions of mid-span section for one blade at different azimuth angles. (a)Unmodified (b) S1 (c) S2

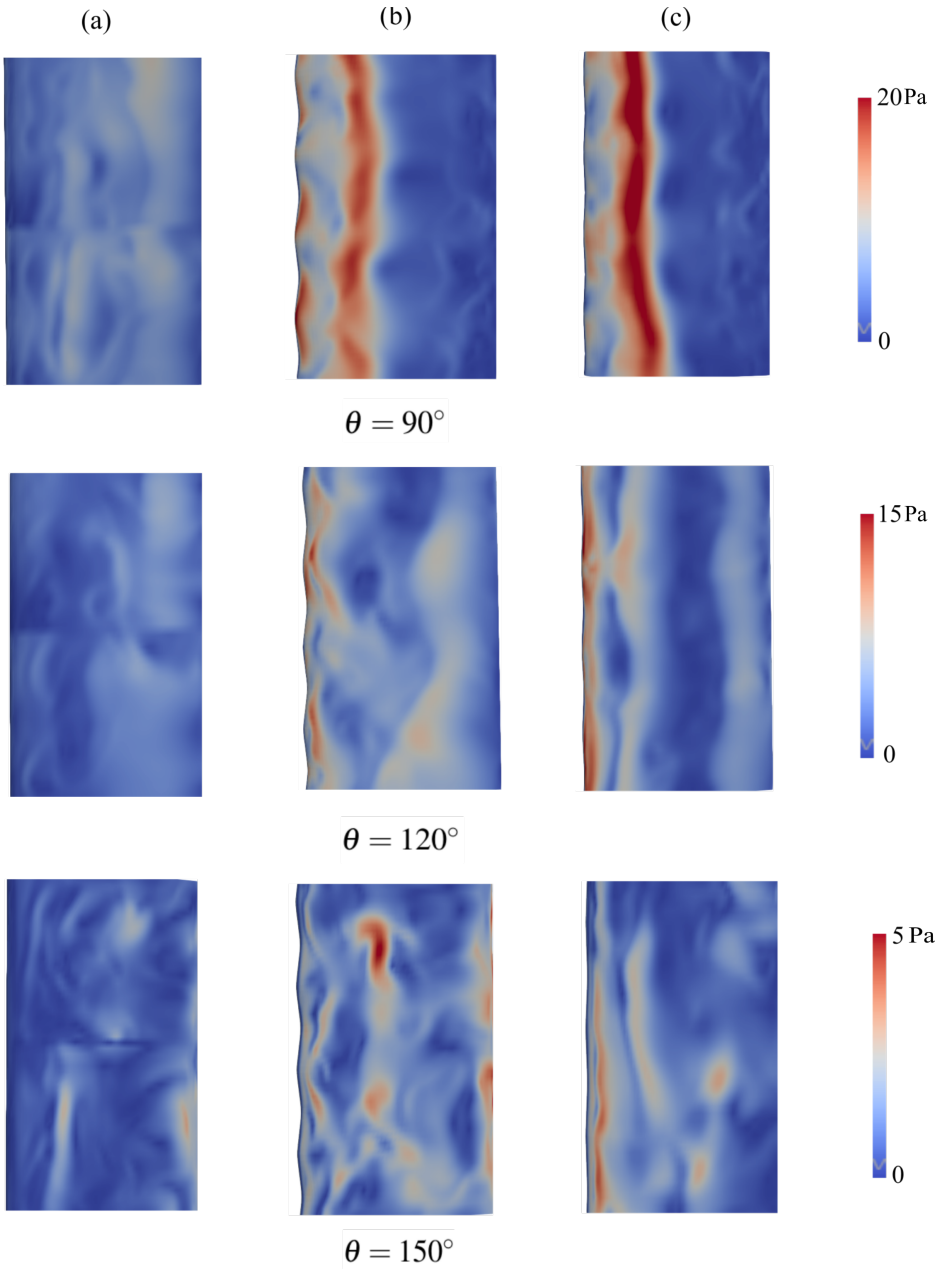


Fig. 6.20 Contour of stress on the suction side of the blades with and without leading-edge protuberances (a)Unmodified (b) S1 (c) S2, TSR=2.

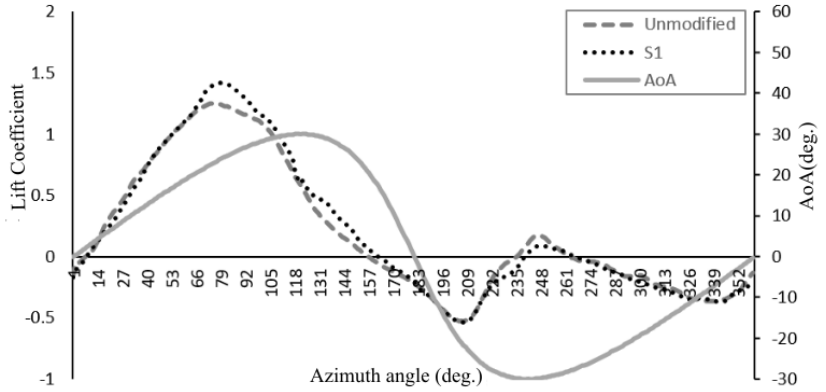


Fig. 6.21 Dynamic lift variation with azimuth angle at TSR=2.0.

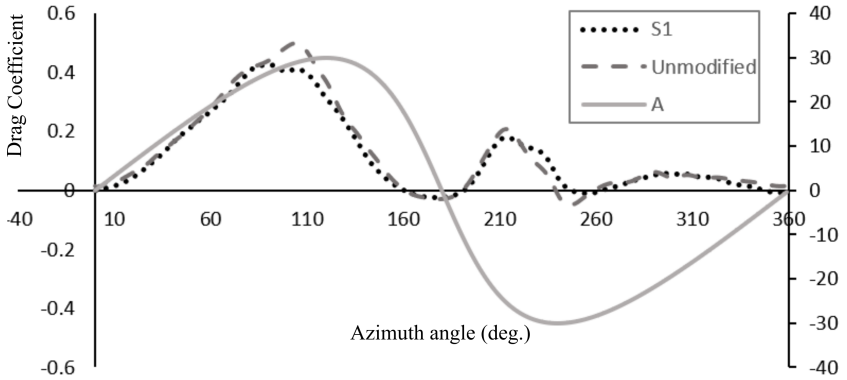


Fig. 6.22 Dynamic drag variation with azimuth angle at TSR=2.0.

Gurney flap investigation. The definitions of $C_L$ and $C_D$ are given in details in Chapter 4. As seen in figure 6.21, the trend of the curve for both cases is similar. With the increase of the azimuth angle, the unmodified case reaches its peak value 1.22 earlier at about $\theta = 75^\circ$ corresponding to the approximate angle of attack of 16°. The maximum $C_L$ of improved model S1 is 16.3% greater than the unmodified case. The $C_L$ declines dramatically after reaching the peak values for both models.

The variation of the $C_D$ for both cases also have a similar trend and obvious discrepancy can be found near the maximum value of $C_D$ corresponding to a high angle of attack. The protuberanced case has a lower value of maximum 0.42 in comparison of 0.51 for the unmodified model. In addition, the improved model has relatively lower $C_D$ at the azimuth angle ranging from 85° to 160°. This is due to the weaker dynamic stall as seen in Figure 6.19, which contributes to a lower drag for the improved case.

## 6.6 Conclusions

The purpose of the present study was to propose and test a practical and effective passive flow control technique called leading-edge protuberance to enhance the aerodynamic performance of a straight blade based on the NACA 0018 aerofoil that is commonly used in the wind industry and an associated H-type vertical axis wind turbine (VAWT) operating at low tip speed ratios. The effect of protuberance with sinusoidal wave patterns of various wavelengths and amplitudes were examined numerically in this study. It was found that the leading-edge protuberance could delay the dynamic stall, especially at low TSRs.

The following conclusions can be highlighted:

1. For a single stationary blade, although the lift coefficient of the protuberanced blade is lower at pre-stall region, the leading-edge protuberances S1 and S2 can effectively delay the aerofoil stall and improve the lift coefficient significantly at post stall angle. The drag coefficient decreases slightly with the modification in the post stall region;

2. It was found that the amplitude of the protuberance had a greater effect on improving the performance as compared to the wavelength. The model with the protuberance wave amplitude of W=0.01c and wave length of k=0.025c produced the best performance for the isolated blade of NACA0018. A "bi-periodic" phenomenon could be observed over the suction surface within a range of angles of attack;

3. For the VAWT, the power output increased greatly by the implementation of the leading-edge protuberance at low TSR that is known to be mostly at post-stall conditions. The vorticity distribution indicated that the dynamic stall was significantly suppressed in the range of the azimuth angle from 90° to 150° at TSR=2. The improved model also showed a higher dynamic lift and lower drag at the azimuth angles ranging from 78° to 110° again as found for TSR=2.

# Chapter 7

# Conclusions and guidelines for future work

## 7.1 Summary

The research presented in this thesis sought to explore effective flow control methods for a small-scale H-type vertical axis wind turbine in order to extend its operating range and to suppress aerodynamic instabilities of the turbine. In order to achieve this goal, three passive flow techniques were tested in the case of isolated static NACA0018 blade that is commonly used in small VAWTs. Afterwards the aerodynamic performance of the improved VAWTs were evaluated in comparison with the unmodified model.

Firstly, the passive flow control device Gurney flap (GF) was investigated. Numerical simulation was performed on the two dimensional aerofoil NACA 0018 and H-type Darrieus wind turbine made of the same aerofoil. Mesh sensitivity study and code validation were conducted to determine the mesh resolution and validate the RANS method. GFs with heights of 1% to 5% of chord length were examined and they were found to have an effect on lift enhancement and stall angle reduction. This effect was even greater when the height of GF increased. The GFs of various mounting angles were tested as well and it was found that the GF perpendicular to the chord line is most effective for lift enhancement. Further work focused on simulating the H-type vertical axis wind turbine. The power coefficient predicted by the numerical method compared well with the published experimental results. The variation of the torque coefficient and the aerodynamic forces within one rotating cycle was illustrated. The evolution of the wake structure and the aerodynamic interaction between the blades and the wake were numerically studied. These results were compared with the

models with GF mounted on the external side of the blade. Such configuration was found to performed better that when mounting the GF on the internal side of the blade.

It was found that the GFs can improve the aerodynamic performance of the VAWT in the upstream region, resulting in an overall improvement for low TSR ranging from 1 to 2, while reducing the overall performance at high TSRs. Among the improved models, the optimum height of GF is 2%c with the largest power coefficient at lower tip speed ratio of TSR =1, 1,5 and 2. Also, the vorticity magnitude distribution near the rotor blade surface indicated that the GFs can suppress flow separation and dynamic stall, pointing to the potential of GF flow control in vertical axis wind turbine design. The MVG has much less parasitic drag than the VG but requires more careful design to achieve aerodynamic improvement.

Another flow control device investigated in this study was the micro vortex generator (MVG), which is a widely-used flow control device for various aerodynamic applications, especially in the wind turbine industry. The main function of the VGs is to transfer momentum from the main stream to the inner boundary layer, in order to suppress flow separation.

Initial study for the flow dynamics of a MVG attached on a flat plate in a turbulent boundary layer was presented first. Numerical simulation using URANS method was conducted for comparison with published experimental results, which included flow field and vortex half-life radius. To further understand the effects of MVGs, several MVGs implemented on the suction side of the aerofoil that was suffering flow separation was numerically investigated. Eight MVGs with various parameters, including shape, position, mounting angle, length and configurations, were examined. It was found that the MVGs increased the skin friction behind the MVG vane via a counter-rotating vortex pair, pointing to a weaker flow separation. Among the modified cases, the optimum MVG vane was found to be located at 20% chord length on the suction side of the aerofoil with a rectangular shape and installed at angle of 16°. With the MVGs, the aerofoil stall angle was delayed from 14° to 16°, while the maximum lift was improved by 37.5% from 0.96 to 1.32, while the drag decrease from to 0.178 to 0.137 at post stall condition $\alpha = 18°$.

Further more, LES study of a small-scale vertical axis wind turbine with MVGs on the outer surface of the three turbine blades was presented. The power coefficient curves were compared to the published experimental and CFD results. Code_Saturne was again used for the turbine calculations and it slightly overestimated power coefficient obtained within the selected TSRs ranging from 1 to 3. The simulation of the improved VAWTs showed a significant enhancement in power generation at high TSR ranging from 2 to 3.5. The phase-averaged torque coefficient indicated that the main improvement obtained at the azimuth angle ranging from 80° to 160°. Similar result can be obtained by analyzing the rotating stall

of the turbine, where the flow separation of turbine blade was suppressed significantly with MVG modification. Among various improved models, the optimum choice for the MVG modification increased the power output by 50% at TSR=3. The MVGs were proven an effective flow control technique for VAWTs, which showed a potential impact on future VAWT design.

The third modification design named as leading-edge protuberance was studied. Numerical simulations were conducted on an isolated stationary NACA 0018 blade to investigate the effects of leading-edge protuberances. Including the baseline, five sinusoidal wave protuberance patterns of various wavelengths and amplitude were considered, with wavelengths ranging from 20 to 40% of chord length and amplitudes ranging from 1 to 3% of chord length. The simulations were carried out using RANS method using the k-$\omega$ turbulence model in the ANSYS software. It was found that the amplitude of the protuberance has a greater effect as compared to its wavelength. At an angle of attack ranging from 11° to 14°, all blades with leading-edge protuberance generated less lift as compared to unmodified model, while at higher AoAs in post stall region, the modified blades produced higher lift. Blades with protuberances generated higher drag in the post stall region with the angle of attack ranging from 14° to 20°. Within the deep stall region, $20^\circ < \alpha < 40^\circ$, S3 model with the largest protuberance amplitude was nearly identical to the unmodified aerofoil, while other two modified models, S1 and S2 produced lower drag.

Furthermore, the flow field showed great differences over the blades with and without modifications. Different flow conditions could be observed in various sections along the spanwise direction of the improved models. The velocity profiles and the vorticity distributions were investigated between two adjacent trough slices for the improved models and the unmodified aerfoil. The development of the "bi-periodic" phenomenon was visualized by streamline patterns on the suction surface of the modified aerofoils. Overall, the best performance was achieved with the improved models of S1 and S2.

For the VAWT, LES study was conducted using Code_Saturne. Three protuberance patterns of various wave amplitudes that were adopted from the isolated blade simulation were applied to the same small-scale VAWT that has been introduced before for the GF and MVG studies. It was found that protuberances increased the $C_P$ at low TSRs that experience significant post-stall conditions during the cycle. For TSR=2 the power coefficient enhancement was mainly obtained at the azimuth angles from 90° to 150°. Separation control and post-stall performance enhancement could be demonstrated by the vorticity distribution and the shear stress on the suction surface. The improved models S1 and S2 showed a greater power generation at the TSR ranging from 1 to 2.5.

In this work the aerodynamic performance of the three passive flow control methods are deeply investigated. They have different effect and optimum operation conditions. For the stationary isolated aerofoil, the GF can increase the lift and drag before stall, but make the stall earlier. The MVG has good behaviour around stall, but mildly worse in post-stall region. The LE protuberance can weaken the stall and improve post stall condition. For the VAWT based on the same aerofoil, the MVG can increase the power generation at high TSRs but mildly reduces power at low TSRs. On the contrary, the GF and LE protuberance increase the power coefficient at low TSRS for the VAWT.

## 7.2 Guidelines for future work

The numerical study in this thesis has made an initial contribution to the study of flow control of the small-scale vertical axis wind turbine. There are number of areas that need further consideration.

In the present study, the attention was firstly paid to the performance of low Reynolds number aerofoils with and without flow control modification. The same inlet conditions are adopted in the original and redesigned aerofoils and wind turbines. The inlet flow used here was steady with constant direction and magnitude. However, it will be of interest to investigate the effect of an unsteady inlet flow condition,e.g., varying velocity magnitude, on the performance of modified aerofoil and the VAWT. The effect of high turbulence intensity at the inlet should also be considered, which might be more realistic.

The computational results based on the numerical methods documented in this study agreed generally well with the published experimental data. However there were some shortcomings for the RANS simulations especially for the drag prediction. In section 5.2, RANS noticeably underestimated the drag of the unmodified aerofoil in the post-stall region. LES study should be recommended to explore if there is interest is to predict the drag more accurately using RANS.

The three flow control methods, Gurney flap, micro vortex generator and leading-edge protuberance were tested separately on the aerofoil and the VAWT. However, each method has its optimum working condition and shortcomings. Drag penalty was caused greatly by GF and leading-edge protuberance in a wide range of angle of attack. It will be of interest to explore the effect of a combination of the various flow control techniques applied on an isolated aerofoil and the wind turbine blade in order to investigate if the performance could be improved and the optimal operating condition of the VAWT can be extended.

# References


[1] Ackermann, T. and Söder, L. (2000). Wind energy technology and current status: a review. *Renewable and sustainable energy reviews*, 4(4):315–374.

[2] Akbari, M. and Price, S. (2003). Simulation of dynamic stall for a naca 0012 airfoil using a vortex method. *Journal of fluids and structures*, 17(6):855–874.

[3] Almohammadi, K. M., Ingham, D. B., Ma, L., and Pourkashanian, M. (2014). 2-d-cfd analysis of the effect of trailing edge shape on the performance of a straight-blade vertical axis wind turbine. *IEEE Transactions on Sustainable Energy*, 6(1):228–235.

[4] Ashill, P., Riddle, G., and Stanley, M. (1994). Control of three-dimensional separation on highly-swept wings. In *ICAS PROCEEDINGS*, volume 19, pages 2012–2012. AMERICAN INST OF AERONAUTICS AND ASTRONAUTICS.

[5] Ashill, P. R., Riddle, G. L., and Stanley, M. (1995). Separation control on highly-swept wings with fixed or variable camber. *The Aeronautical Journal*, 99(988):317–327.

[6] Aspden, A., Nikiforakis, N., Dalziel, S., and Bell, J. (2009). Analysis of implicit les methods. *Communications in Applied Mathematics and Computational Science*, 3(1):103–126.

[7] Association, A. W. E. et al. (2009). American wind energy association annual wind industry report.

[8] Balduzzi, F., Bianchini, A., Maleci, R., Ferrara, G., and Ferrari, L. (2016). Critical issues in the cfd simulation of darrieus wind turbines. *Renewable Energy*, 85:419–435.

[9] Bianchini, A., Balduzzi, F., Di Rosa, D., and Ferrara, G. (2019). On the use of gurney flaps for the aerodynamic performance augmentation of darrieus wind turbines. *Energy conversion and management*, 184:402–415.

[10] Bianchini, A., Balduzzi, F., Ferrara, G., and Ferrari, L. (2016). A computational procedure to define the incidence angle on airfoils rotating around an axis orthogonal to flow direction. *Energy conversion and management*, 126:790–798.

[11] Boris, J. P. (1990). On large eddy simulation using subgrid turbulence models comment 1. In *Whither turbulence? Turbulence at the crossroads*, pages 344–353. Springer.

[12] Bravo, R., Tullis, S., and Ziada, S. (2007). Performance testing of a small vertical-axis wind turbine. In *Proceedings of the 21st Canadian Congress of Applied Mechanics (CANCAM07), Toronto, Canada, June*, pages 3–7.

[13] Cai, C., Zuo, Z., Liu, S., and Wu, Y. (2015). Numerical investigations of hydrodynamic performance of hydrofoils with leading-edge protuberances. *Advances in Mechanical Engineering*, 7(7):1687814015592088.

[14] Calarese, W., Crisler, W., and GUSTAFSON, G. (1985). Afterbody drag reduction by vortex generators. In *23rd Aerospace Sciences Meeting*, page 354.

[15] Castelli, M. R., Englaro, A., and Benini, E. (2011). The darrieus wind turbine: Proposal for a new performance prediction model based on cfd. *Energy*, 36(8):4919–4934.

[16] Chen, J., Yang, H., Yang, M., Xu, H., and Hu, Z. (2015). A comprehensive review of the theoretical approaches for the airfoil design of lift-type vertical axis wind turbine. *Renewable and sustainable energy reviews*, 51:1709–1720.

[17] Collins, F. G. (1981). Boundary-layer control on wings using sound and leading-edge serrations. *AIAA Journal*, 19(2):129–130.

[18] Consul, C., Willden, R., Ferrer, E., and McCulloch, M. (2009). Influence of solidity on the performance of a cross-flow turbine. In *Proceedings of the 8th European wave and tidal energy conference, Uppsala, Sweden*.

[19] Date, J. C. and Turnock, S. R. (2002). Computational evaluation of the periodic performance of a naca 0012 fitted with a gurney flap. *Journal of fluids engineering*, 124(1):227–234.

[20] Debiasi, M., Khoo, H. H., Bouremel, Y., Luo, S., and Zhiwei, E. (2011). Shape change of the upper surface of an airfoil by macro fiber composite actuators. In *29th AIAA Applied Aerodynamics Conference*, page 3809.

[21] Debnath, B. K., Biswas, A., and Gupta, R. (2009). Computational fluid dynamics analysis of a combined three-bucket savonius and three-bladed darrieus rotor at various overlap conditions. *Journal of Renewable and Sustainable energy*, 1(3):033110.

[22] Dropkin, A., Custodio, D., Henoch, C., and Johari, H. (2012). Computation of flow field around an airfoil with leading-edge protuberances. *Journal of Aircraft*, 49(5):1345–1355.

[23] Ekaterinaris, J. A. and Platzer, M. F. (1998). Computational prediction of airfoil dynamic stall. *Progress in aerospace sciences*, 33(11-12):759–846.

[24] El Rafei, M., Könözsy, L., and Rana, Z. (2017). Investigation of numerical dissipation in classical and implicit large eddy simulations. *Aerospace*, 4(4):59.

[25] Eriksson, S., Bernhoff, H., and Leijon, M. (2008). Evaluation of different turbine concepts for wind power. *renewable and sustainable energy reviews*, 12(5):1419–1434.

[26] Ferreira, C. S., Van Kuik, G., Van Bussel, G., and Scarano, F. (2009). Visualization by piv of dynamic stall on a vertical axis wind turbine. *Experiments in Fluids*, 46(1):97–108.

[27] Fiedler, B. and Bukovsky, M. (2011). The effect of a giant wind farm on precipitation in a regional climate model. *Environmental Research Letters*, 6(4):045101.

[28] Fish, F. E. (1999). Performance constraints on the maneuverability of flexible and rigid biological systems. In *International Symposium on Unmanned Untethered Submersible Technology*, pages 394–406. University of New Hampshire-Marine Systems.

[29] Fish, F. E. and Battle, J. M. (1995). Hydrodynamic design of the humpback whale flipper. *Journal of Morphology*, 225(1):51–60.

[30] Fouatih, O. M., Medale, M., Imine, O., and Imine, B. (2016). Design optimization of the aerodynamic passive flow control on naca 4415 airfoil using vortex generators. *European Journal of Mechanics-B/Fluids*, 56:82–96.

[31] Fournier, Y., Bonelle, J., Moulinec, C., Shang, Z., Sunderland, A., and Uribe, J. (2011). Optimizing code_saturne computations on petascale systems. *Computers & Fluids*, 45(1):103–108.

[32] Gao, L., Zhang, H., Liu, Y., and Han, S. (2015). Effects of vortex generators on a blunt trailing-edge airfoil for wind turbines. *Renewable Energy*, 76:303–311.

[33] Giguere, P., Lemay, J., and Dumas, G. (1995). Gurney flap effects and scaling for low-speed airfoils. In *13th Applied Aerodynamics Conference*, page 1881.

[34] Greenblatt, D., Ben-Harav, A., and Mueller-Vahl, H. (2014). Dynamic stall control on a vertical-axis wind turbine using plasma actuators. *AIAA journal*, 52(2):456–462.

[35] Grinstein, F. F., Margolin, L. G., and Rider, W. J. (2007). *A rationale for implicit LES*. Cambridge University Press, Cambridge.

[36] Guide, A. F. U. (2016). Release 17.0. *Ansys Inc*.

[37] Gupta, R. and Biswas, A. (2010). Computational fluid dynamics analysis of a twisted three-bladed h-darrieus rotor. *Journal of Renewable and Sustainable Energy*, 2(4):043111.

[38] Gupta, S. and Leishman, J. G. (2006). Dynamic stall modelling of the s809 aerofoil and comparison with experiments. *Wind Energy: An International Journal for Progress and Applications in Wind Power Conversion Technology*, 9(6):521–547.

[39] GWEC, G. W. E. C. (2017). Global wind report. 2015. *Brussels: GWEC*.

[40] Hamada, K., Smith, T., Durrani, N., Qin, N., and Howell, R. (2008). Unsteady flow simulation and dynamic stall around vertical axis wind turbine blades. In *46th AIAA Aerospace Sciences Meeting and Exhibit*, page 1319.

[41] Hansen, A. and Butterfield, C. (1993). Aerodynamics of horizontal-axis wind turbines. *Annual Review of Fluid Mechanics*, 25(1):115–149.

[42] Hansen, K. L., Kelso, R. M., and Dally, B. B. (2011). Performance variations of leading-edge tubercles for distinct airfoil profiles. *AIAA journal*, 49(1):185–194.

[43] Hau, E. (2013). *Wind turbines: fundamentals, technologies, application, economics*. Springer Science & Business Media.

[44] Heffron, A., Williams, J. J., and Avital, E. J. (2016). Flow seperation and passive flow control on e387 airfoil. In *54th AIAA Aerospace Sciences Meeting*, page 0324.

[45] Heffron, A. P. (2017). *Rotating Stall and Passive Flow Control on Blade Profiles and in Centrifugal Compressors*. PhD thesis, Queen Mary University of London.

[46] Heffron, A. P., Williams, J. J., and Avital, E. (2018). Numerical and experimental study of microvortex generators. *Journal of Aircraft*, 55(6):2256–2266.

[47] Hersh, A. S., Sodermant, P. T., and Hayden, R. E. (1974). Investigation of acoustic effects of leading-edge serrations on airfoils. *Journal of Aircraft*, 11(4):197–202.

[48] Hoerner, S. F. and Borst, H. V. (1975). Fluid-dynamic lift, practical information on aerodynamic and hydrodynamic lift. Technical report, BORST (HENRY V) AND ASSOCIATES WAYNE PA.

[49] Horton, H. P. (1968). *Laminar separation bubbles in two and three dimensional incompressible flow.* PhD thesis.

[50] Howe, M. S. (1991). Aerodynamic noise of a serrated trailing edge. *Journal of Fluids and Structures*, 5(1):33–45.

[51] Howell, R., Qin, N., Edwards, J., and Durrani, N. (2010). Wind tunnel and numerical study of a small vertical axis wind turbine. *Renewable energy*, 35(2):412–422.

[52] Huang, J., Corke, T. C., and Thomas, F. O. (2006). Plasma actuators for separation control of low-pressure turbine blades. *AIAA journal*, 44(1):51–57.

[53] Islam, M., Mekhilef, S., and Saidur, R. (2013). Progress and recent trends of wind energy technology. *Renewable and Sustainable Energy Reviews*, 21:456–468.

[54] Islam, M., Ting, D. S., and Fartaj, A. (2007). Desirable airfoil features for smaller-capacity straight-bladed vawt. *Wind Engineering*, 31(3):165–196.

[55] Jang, C. S., Ross, J. C., and Cummings, R. M. (1998). Numerical investigation of an airfoil with a gurney flap. *Aircraft Design*, 1(2):75–88.

[56] Jeffrey, D. and Hurst, D. (1996). Aerodynamics of the gurney flap. In *14th Applied Aerodynamics Conference*, page 2418.

[57] Jin, X., Zhao, G., Gao, K., and Ju, W. (2015). Darrieus vertical axis wind turbine: Basic research methods. *Renewable and Sustainable Energy Reviews*, 42:212–225.

[58] Johari, H., Henoch, C. W., Custodio, D., and Levshin, A. (2007). Effects of leading-edge protuberances on airfoil performance. *AIAA journal*, 45(11):2634–2642.

[59] Johnston Jr, S. F. (1980). Proceedings of the vertical axis wind turbine (vawt) design technology seminar for industry. Technical report, Sandia Labs., Albuquerque, NM (USA).

[60] Keith, D. W., DeCarolis, J. F., Denkenberger, D. C., Lenschow, D. H., Malyshev, S. L., Pacala, S., and Rasch, P. J. (2004). The influence of large-scale wind power on global climate. *Proceedings of the National Academy of Sciences*, 101(46):16115–16120.

[61] Khan, M., Bhuyan, G., Iqbal, M., and Quaicoe, J. (2009). Hydrokinetic energy conversion systems and assessment of horizontal and vertical axis turbines for river and tidal applications: A technology status review. *Applied energy*, 86(10):1823–1835.

[62] Kim, D. and Gharib, M. (2013). Efficiency improvement of straight-bladed vertical-axis wind turbines with an upstream deflector. *Journal of Wind Engineering and Industrial Aerodynamics*, 115:48–52.

[63] Kirk-Davidoff, D. B. and Keith, D. W. (2008). On the climate impact of surface roughness anomalies. *Journal of the Atmospheric Sciences*, 65(7):2215–2234.

[64] Kishore, R. A., Coudron, T., and Priya, S. (2013). Small-scale wind energy portable turbine (swept). *Journal of wind engineering and industrial aerodynamics*, 116:21–31.

[65] Kuvlesky Jr, W. P., Brennan, L. A., Morrison, M. L., Boydston, K. K., Ballard, B. M., and Bryant, F. C. (2007). Wind energy development and wildlife conservation: challenges and opportunities. *The Journal of Wildlife Management*, 71(8):2487–2498.

[66] Langtry, R., Gola, J., and Menter, F. (2006). Predicting 2d airfoil and 3d wind turbine rotor performance using a transition model for general cfd codes. In *44th AIAA aerospace sciences meeting and exhibit*, page 395.

[67] Leddy, K. L., Higgins, K. F., and Naugle, D. E. (1999). Effects of wind turbines on upland nesting birds in conservation reserve program grasslands. *The Wilson Bulletin*, pages 100–104.

[68] Li, Q., Maeda, T., Kamada, Y., Murata, J., Shimizu, K., Ogasawara, T., Nakai, A., and Kasuya, T. (2016). Effect of solidity on aerodynamic forces around straight-bladed vertical axis wind turbine by wind tunnel experiments (depending on number of blades). *Renewable energy*, 96:928–939.

[69] Li, Y., Wang, J., and Hua, J. (2007). Experimental investigations on the effects of divergent trailing edge and gurney flaps on a supercritical airfoil. *Aerospace Science and Technology*, 11(2-3):91–99.

[70] Li, Y., Wang, J., and Zhang, P. (2002). Effects of gurney flaps on a naca0012 airfoil. *Flow, Turbulence and Combustion*, 68(1):27.

[71] Li, Y., Wang, J., and Zhang, P. (2003). Influences of mounting angles and locations on the effects of gurney flaps. *Journal of Aircraft*, 40(3):494–498.

[72] Liebeck, R. H. (1978). Design of subsonic airfoils for high lift. *Journal of aircraft*, 15(9):547–561.

[73] Lin, J. C. (2002). Review of research on low-profile vortex generators to control boundary-layer separation. *Progress in Aerospace Sciences*, 38(4-5):389–420.

[74] Lin, J. C., Robinson, S. K., McGhee, R. J., and Valarezo, W. O. (1994). Separation control on high-lift airfoils via micro-vortex generators. *Journal of aircraft*, 31(6):1317–1323.

[75] Liu, Y., Li, K., Zhang, J., Wang, H., and Liu, L. (2012). Numerical bifurcation analysis of static stall of airfoil and dynamic stall under unsteady perturbation. *Communications in Nonlinear Science and Numerical Simulation*, 17(8):3427–3434.

[76] McCroskey, W. J., Carr, L. W., and McAlister, K. W. (1976). Dynamic stall experiments on oscillating airfoils. *Aiaa Journal*, 14(1):57–63.

[77] McGhee, R. J., Walker, B. S., and Millard, B. F. (1988). Experimental results for the eppler 387 airfoil at low reynolds numbers in the langley low-turbulence pressure tunnel.

[78] McGranahan, B. and Selig, M. (2003). Surface oil flow measurements on several airfoils at low reynolds numbers. In *21st AIAA Applied Aerodynamics Conference*, page 4067.

[79] Menter, F. (1992). Improved two-equation k–$\omega$ turbulence models for aerodynamic flows. nasa sti. Technical report, Recon Technical Report 93, 22809.

[80] Menter, F. (1993). Zonal two equation kw turbulence models for aerodynamic flows. In *23rd fluid dynamics, plasmadynamics, and lasers conference*, page 2906.

[81] Mohamed, M. (2012). Performance investigation of h-rotor darrieus turbine with new airfoil shapes. *Energy*, 47(1):522–530.

[82] Mohamed, M., Ali, A., and Hafiz, A. (2015). Cfd analysis for h-rotor darrieus turbine as a low speed wind energy converter. *Engineering Science and Technology, an International Journal*, 18(1):1–13.

[83] Moreau, E. (2007). Airflow control by non-thermal plasma actuators. *Journal of physics D: applied physics*, 40(3):605.

[84] Mueller-Vahl, H., Pechlivanoglou, G., Nayeri, C., and Paschereit, C. (2012). Vortex generators for wind turbine blades: A combined wind tunnel and wind turbine parametric study. In *ASME Turbo Expo 2012: Turbine Technical Conference and Exposition*, pages 899–914. American Society of Mechanical Engineers.

[85] Müller, G., Jentsch, M. F., and Stoddart, E. (2009). Vertical axis resistance type wind turbines for use in buildings. *Renewable Energy*, 34(5):1407–1412.

[86] Óskarsdóttir, M. Ó. et al. (2014). *A General Description and Comparison of Horizontal Axis Wind Turbines and Vertical Axis Wind Turbines*. PhD thesis.

[87] Paraschivoiu, I., Trifu, O., and Saeed, F. (2009). H-darrieus wind turbine with blade pitch control. *International Journal of Rotating Machinery*, 2009.

[88] Pope, K., Rodrigues, V., Doyle, R., Tsopelas, A., Gravelsins, R., Naterer, G., and Tsang, E. (2010). Effects of stator vanes on power coefficients of a zephyr vertical axis wind turbine. *Renewable Energy*, 35(5):1043–1051.

[89] Post, M. L. and Corke, T. C. (2006). Separation control using plasma actuators: dynamic stall vortex control on oscillating airfoil. *AIAA journal*, 44(12):3125–3135.

[90] Price, T. J. (2006). Uk large-scale wind power programme from 1970 to 1990: the carmarthen bay experiments and the musgrove vertical-axis turbines. *Wind Engineering*, 30(3):225–242.

[91] Rezaeiha, A., Kalkman, I., Montazeri, H., and Blocken, B. (2017). Effect of the shaft on the aerodynamic performance of urban vertical axis wind turbines. *Energy conversion and management*, 149:616–630.

[92] Roger, M., Schram, C., and De Santana, L. (2013). Reduction of airfoil turbulence-impingement noise by means of leading-edge serrations and/or porous material. In *19th AIAA/CEAS aeroacoustics conference*, page 2108.

[93] Roh, J.-H., Kim, K.-S., and Lee, I. (2009). Shape adaptive airfoil actuated by a shape memory alloy and its aerodynamic characteristics. *Mechanics of Advanced Materials and Structures*, 16(3):260–274.

[94] Roshan, S. Z., Alimirzazadeh, S., and Rad, M. (2015). Rans simulations of the stepped duct effect on the performance of ducted wind turbine. *Journal of Wind Engineering and Industrial Aerodynamics*, 145:270–279.

[95] Roy, S. and Saha, U. K. (2013). Numerical investigation to assess an optimal blade profile for the drag based vertical axis wind turbine. In *ASME 2013 International Mechanical Engineering Congress and Exposition*, pages V06AT07A084–V06AT07A084. American Society of Mechanical Engineers.

[96] Saeed, F., Paraschivoiu, I., Trifu, O., Hess, M., and Gabrys, C. (2011). Inverse airfoil design method for low-speed straight-bladed darrieus-type vawt applications. *Wind Engineering*, 35(3):357–367.

[97] Sasson, B. and Greenblatt, D. (2011). Effect of leading-edge slot blowing on a vertical axis wind turbine. *AIAA journal*, 49(9):1932–1942.

[98] Saturne, C. (2015). 4.0. 0 theory guide. *Fluid Dynamics, Power Generation and Environment Department, Single Phase Thermal-Hydraulics Group, EDF Lab Chatou, France*.

[99] Sawin, J. L., Martinot, E., Sonntag-O'Brien, V., McCrone, A., Roussell, J., Barnes, D., Flavin, C., Mastny, L., Kraft, D., Wang, S., et al. (2010). Renewables 2010-global status report.

[100] Schlichting, H. (1979). Boundary layer theory, 7t h mcgraw-hill. *New York*.

[101] Sheldahl, R. E. and Klimas, P. C. (1981). Aerodynamic characteristics of seven symmetrical airfoil sections through 180-degree angle of attack for use in aerodynamic analysis of vertical axis wind turbines. Technical report, Sandia National Labs., Albuquerque, NM (USA).

[102] Shen, X., Avital, E., Paul, G., Rezaienia, M. A., Wen, P., and Korakianitis, T. (2016). Experimental study of surface curvature effects on aerodynamic performance of a low reynolds number airfoil for use in small wind turbines. *Journal of Renewable and Sustainable Energy*, 8(5):053303.

[103] Shen, X., Avital, E., Rezaienia, M. A., Paul, G., and Korakianitis, T. (2017). Computational methods for investigation of surface curvature effects on airfoil boundary layer behavior. *Journal of Algorithms & amp; Computational Technology*, 11(1):68–82.

[104] Sinha, S. (1999). System for efficient control of flow separation using a driven flexible wall. *US Patents*, 5(961):080.

[105] Sinha, S. (2007). Optimizing wing lift to drag ratio enhancement with flexible-wall turbulence control. In *25th AIAA Applied Aerodynamics Conference*, page 4425.

[106] Skillen, A., Revell, A., Pinelli, A., Piomelli, U., and Favier, J. (2014). Flow over a wing with leading-edge undulations. *Aiaa Journal*, 53(2):464–472.

[107] Stephen, B. P. et al. (2000). Turbulent flows. *Cambridge University*, pages 387–457.

[108] Storms, B. L. and Jang, C. S. (1994). Lift enhancement of an airfoil using a gurney flap and vortex generators. *Journal of Aircraft*, 31(3):542–547.

[109] Stough III, H. P. and DiCarlo, D. J. (2000). Spin resistance development for small airplanes–a retrospective. *SAE transactions*, pages 145–171.

[110] Taylor, H. (1947). The elimination of diffuser separation by vortex generators. united aircraft corporation research department report no. Technical report, R-4012-3.

[111] Tjiu, W., Marnoto, T., Mat, S., Ruslan, M. H., and Sopian, K. (2015). Darrieus vertical axis wind turbine for power generation ii: Challenges in hawt and the opportunity of multi-megawatt darrieus vawt development. *Renewable Energy*, 75:560–571.

[112] Van Dam, C., Berg, D. E., and Johnson, S. J. (2008). Active load control techniques for wind turbines. Technical report, Sandia National Laboratories.

[113] Velasco, D., Mejia, O. L., and Laín, S. (2017). Numerical simulations of active flow control with synthetic jets in a darrieus turbine. *Renewable Energy*, 113:129–140.

[114] Wang, J., Li, Y., and Choi, K.-S. (2008). Gurney flap—lift enhancement, mechanisms and applications. *Progress in Aerospace sciences*, 44(1):22–47.

[115] Wang, T. (1999). *Unsteady aerodynamic modelling of horizontal axis wind turbine performance*. PhD thesis, University of Glasgow.

[116] Wang, Z. and Zhuang, M. (2017). Leading-edge serrations for performance improvement on a vertical-axis wind turbine at low tip-speed-ratios. *Applied Energy*, 208:1184–1197.

[117] WILCOX, D. (1988). Multiscale model for turbulent flows. *AIAA*, 26(1):1311–1320.

[118] Wilcox, D. C. (1988). Multiscale model for turbulent flows. *AIAA journal*, 26(11):1311–1320.

[119] Wu, J. and Tao, W. (2012). Effect of longitudinal vortex generator on heat transfer in rectangular channels. *Applied Thermal Engineering*, 37:67–72.

[120] Wu, J.-C., Sankar, L., and HUFF, D. (1988). Evaluation of three turbulence models for the prediction of steady and unsteady airloads. In *27th Aerospace Sciences Meeting*, page 609.

[121] Yang, Y., Li, C., Zhang, W., Guo, X., and Yuan, Q. (2017). Investigation on aerodynamics and active flow control of a vertical axis wind turbine with flapped airfoil. *Journal of Mechanical Science and Technology*, 31(4):1645–1655.

[122] Yao, C., Lin, J., and Allen, B. (2002). Flowfield measurement of device-induced embedded streamwise vortex on a flat plate. In *1st Flow Control Conference*, page 3162.

[123] Yashodhar, V., Humrutha, G., Kaushik, M., and Khan, S. (2017). Cfd studies on triangular micro-vortex generators in flow control. In *IOP Conference Series: Materials Science and Engineering*, volume 184, page 012007. IOP Publishing.

[124] You, D. and Moin, P. (2008). Active control of flow separation over an airfoil using synthetic jets. *Journal of Fluids and structures*, 24(8):1349–1357.

[125] Yousefi, K., Saleh, R., and Zahedi, P. (2014). Numerical study of blowing and suction slot geometry optimization on naca 0012 airfoil. *Journal of Mechanical Science and Technology*, 28(4):1297–1310.

[126] Yu, T., Wang, J., and Zhang, P. (2011). Numerical simulation of gurney flap on rae-2822 supercritical airfoil. *Journal of Aircraft*, 48(5):1565–1575.

[127] Zhao, M., Zhang, M., and Xu, J. (2017). Numerical simulation of flow characteristics behind the aerodynamic performances on an airfoil with leading edge protuberances. *Engineering Applications of Computational Fluid Mechanics*, 11(1):193–209.

[128] Zhen, T. K., Zubair, M., and Ahmad, K. A. (2011). Experimental and numerical investigation of the effects of passive vortex generators on aludra uav performance. *Chinese Journal of Aeronautics*, 24(5):577–583.

[129] Zhu, H., Hao, W., Li, C., and Ding, Q. (2018). Simulation on flow control strategy of synthetic jet in an vertical axis wind turbine. *Aerospace Science and Technology*, 77:439–448.